# MELBOURNE GRADUATE

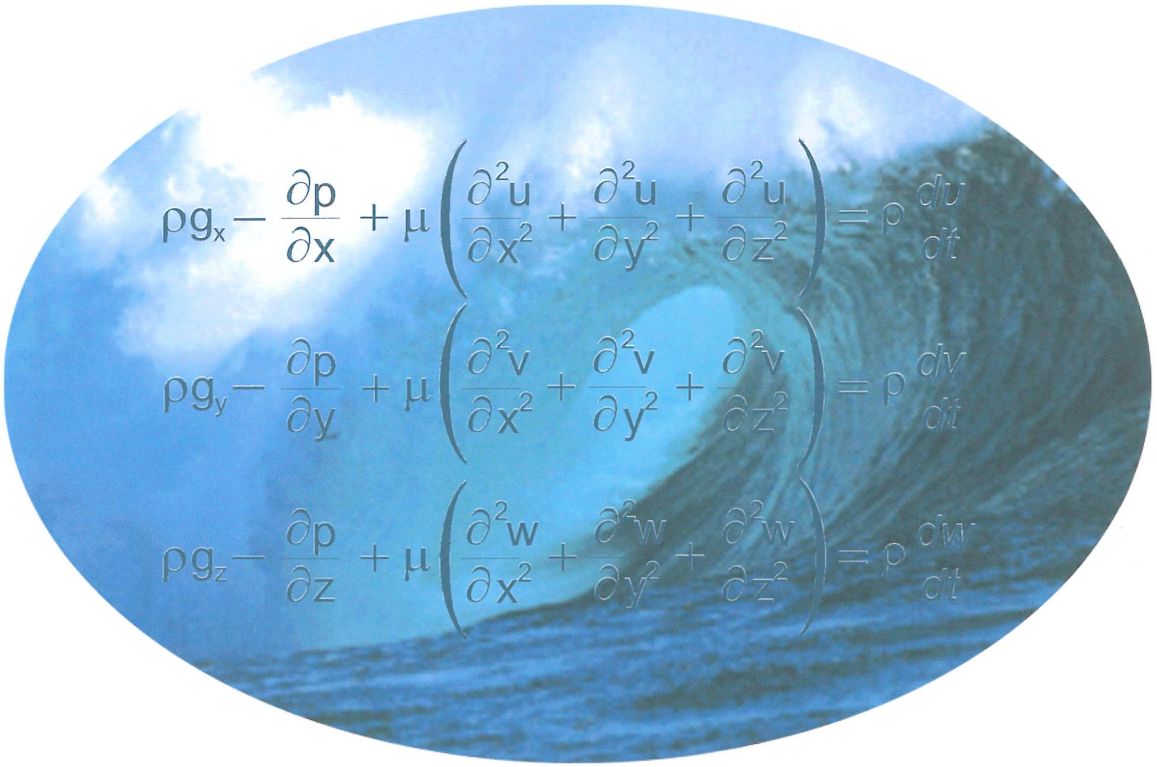


# FLUIDS CONFERENCE

MONASH UNIVERSITY
JULY 2001

MONASH
UNIVERSITY

# TIMETABLE & INDEX

## Session 1



## Session 2



## Session 3



## Session 4

*Melbourne Graduate Fluids Conference*
*Monash University, Melbourne, Australia*

# Turbulent Pipe Flow: Characteristics of the Mean Velocity Profile

**Jason P. MONTY, Salah HAFEZ, Malcolm B. JONES and Min S. CHONG**

Department of Mechanical and Manufacturing Engineering
University of Melbourne, VIC. 3010, Australia

## ABSTRACT

An analysis of recent data recorded in a pipe flow facility at Melbourne is presented. The data consists of 5 mean velocity profiles in the Reynolds number range: $43\times10^3$ - $142\times10^3$ all taken using a Pitot tube. These profiles are compared with those of Zagarola & Smits[1] and Österlund[2].

The velocity profiles are shown to collapse onto the logarithmic law of the wall when scaled appropriately and the universal constants, $\kappa$ and $A$, are determined.

## 1. INTRODUCTION

Research into the mean velocity distribution in turbulent pipe and boundary layer flows has received added attention recently due to the results of the Princeton University "superpipe" experiment. The "superpipe" was able to achieve very high Reynolds number flows (up to $35\times10^6$) using compressed air as the working fluid. In analysing their "superpipe" data, Zagarola & Smits[1] developed a number of controversial conclusions, including the existence of a power law region as well as a log law region of the velocity profile and large values of $\kappa$ and $A$.

Opposing these views is Österlund[2] who gives a detailed analysis of results taken in a boundary layer with a hot-wire anemometer. Perry *et al.*[3] reinterpreted the "superpipe" data and found support for Österlund[2], but made the observation: "What is urgently needed is an extensive set of mean velocity profiles in a pipe measured with a hot-wire". This comment is the motivation for the current investigation. However, at this point only Pitot tube results have been recorded and these are presented in this paper.

## 2. EXPERIMENTAL METHOD

Perhaps the most significant feature of the experimental apparatus is the length of the pipe. It is close to 400 diameters ($\frac{L}{D} = 397.8$) from the entrance to the test location which should ensure full flow development. Most of the pipe lengths used were originally assembled by Henbest[4], however, a new test section and calibration section were constructed and a new fan controller installed. Also, the pipe has been disassembled, carefully polished, checked, reassembled and realigned.

Immediately downstream of the contraction I (see Figure 1), a sand paper trip (60 grit and 15cm long) has been glued to the pipe surface. There are a total of six static pressure taps along the length of the pipe, at roughly 6 metre intervals, used to calculate the static pressure gradient.

Figure 1(a) shows the setup used to take mean velocity measurements. Measurements are taken with a Pitot-static tube mounted on a manual traverse capable of 25.4 $\mu$m increments. A *Halstrup type PU* pressure transducer interfacing with a *GWI MACADIOS II* data acquisition board (3 bursts of 30sec samples at 1kHz) is used to measure the velocity at 30 positions through the pipe cross section. Profiles were recorded for $\mathrm{Re} = \frac{\overline{U}D}{\nu} = 43\times10^3$, $58\times10^3$, $76\times10^3$, $95\times10^3$ and $142\times10^3$ ($\overline{U}$ is the bulk velocity, D is the pipe internal diameter).

Figure 1(b) is the hot-wire static calibration setup. During calibration, the test section is detached from the main pipe and attached to contraction II. The downstream end of the test section is connected straight onto the fan. This setup ensures the uniform flow required to perform the calibration accurately. Pitot tube measurements do not require this calibration, hence only the apparatus shown in Figure 1(a) is currently in use.

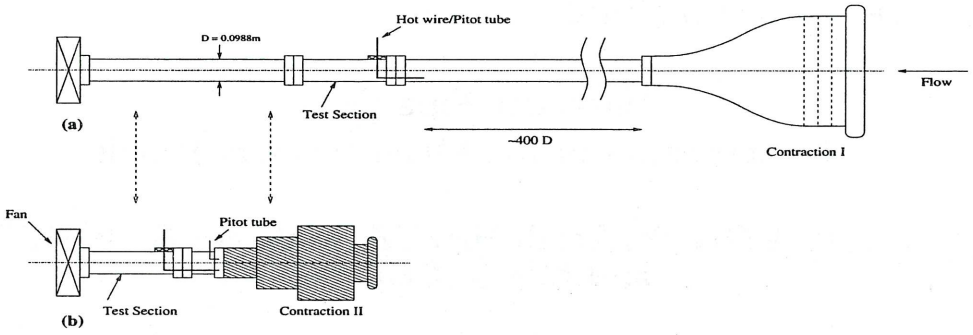


**Figure 1:** Schematic diagram of pipe flow facility

# 3. RESULTS AND DISCUSSION

## 3.1 Mean Velocity Profiles

A classical result of turbulence theory is that turbulent pipe flow can be split into two basic regions, an inner flow region and an outer flow region. Dimensional analysis gives functional relationships between the suitably scaled mean velocity, $U$ and distance from the wall, $y$. Suitable scales for the inner flow region are a viscous length scale, $\frac{\nu}{U_\tau}$ and the friction velocity, $U_\tau = \sqrt{\tau_w/\rho}$ where $\tau_w$ is the wall shear stress (calculated from the static pressure gradient), $\rho$ is the density, and $\nu$ the kinematic viscosity. In the outer flow region, the pipe internal radius, $a$, and friction velocity are the appropriate length and velocity scales respectively. The functional relationship in the inner flow region is given by:

$$\frac{U}{U_\tau} = f(\frac{yU_\tau}{\nu}) \tag{1}$$

and in the outer flow region:

$$\frac{U_{CL} - U}{U_\tau} = g(\frac{y}{a}), \tag{2}$$

where $U_{CL}$ is the velocity at the pipe centreline. It is assumed that there is a region of the pipe flow where both functional relationships apply, that is, an overlap of inner flow and outer flow regions. Finding mean velocity gradients and integrating, noting that the functions $f$ and $g$ must be independent of the viscous length scale and pipe radius in the overlap region gives,

$$U^+ = \frac{U}{U_\tau} = \frac{1}{\kappa}\ln(y^+) + A; \qquad y^+ = \frac{yU_\tau}{\nu} \tag{3}$$

$$\frac{U_{CL} - U}{U_\tau} = -\frac{1}{\kappa}\ln(\eta) + B; \qquad \eta = \frac{y}{a} \tag{4}$$

Equation 3 is known as the logarithmic law of the wall, and equation 4, the velocity defect law. $\kappa$ and $A$ are universal constants in the overlap region and so all data in this region of the inner scaled velocity profiles should collapse onto equation 3. The mean velocity profiles with inner flow scaling are plotted in Figure 2 with the abscissa plotted logarithmically and the ordinate naturally. The extent of collapse in the wall region is clearly excellent for all Reynolds numbers tested.

To determine $\kappa$ and $A$, the overlap region must be quantitatively defined. At this stage, a lower limit of $y^+ = 100$ and upper limit of $\eta = 0.15$ are chosen. (Note: These limits will be revised when full Pitot tube and hot-wire data sets are available). Extracting data between these limits and performing a least squares error fit for each Reynolds number profile gives values of $\kappa$ and $A$. Averaging each set of constants over all Reynolds numbers gives $\kappa = 0.386$ and $A = 4.21$. These values are very similar to those of Österlund[2] ($\kappa = 0.384$, $A = 4.1$) and Perry *et al.*[3] (0.39, 4.42), although markedly different to Zagarola & Smits[1] (0.436, 6.13). The log law given below is also plotted in Figure 2 (solid line).

$$U^+ = \frac{1}{0.386}\ln(y^+) + 4.21, \tag{5}$$

## 3.2 Corrections

The velocity profiles plotted in Figure 2 have been corrected for errors in Pitot tube measurements. Firstly, MacMillan[5] found that an addition of $0.15d_p$ ($d_p = 1.4$mm is the Pitot tube outer diameter) to the wall distance measurement corrects for mean shear. Secondly, a velocity fluctuation correction is given by:

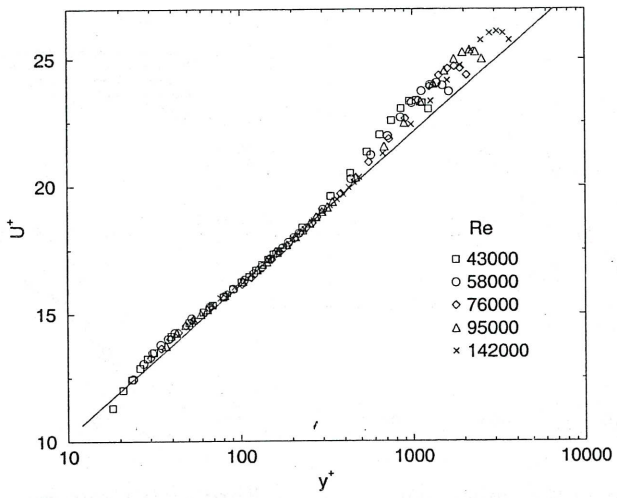


**Figure 2:** Corrected Velocity profiles scaled with inner flow variables.

$$\frac{U}{U_\tau} = \sqrt{\left(\frac{U_m}{U_\tau}\right)^2 - \frac{\overline{u_1^2}}{U_\tau^2}}, \tag{6}$$

where $U$ is the corrected mean velocity, $U_m$ is the measured mean velocity and $\overline{u_1^2}$ is the mean square of velocity fluctuations in the streamwise direction. However, no turbulence measurements have been recorded so the following laws were utilised,
For $y^+ > 50$ (Perry *et al.*[6]):

$$\frac{\overline{u_1^2}}{U_\tau^2} = 2.67 - 0.9\ln\eta - 6.06(y^+)^{-0.5} \tag{7}$$

For $15 < y^+ < 50$ (Abell[7]):

$$\frac{\overline{u_1^2}}{U_\tau^2} = 3 - 1.5\log\left(\frac{y^+}{15}\right). \tag{8}$$

### 3.3 Comparison of Results

Figure 3 contains profiles of Österlund's[2] hot-wire data plotted over the corrected results of this investigation at the highest and lowest Reynolds numbers measured. Figure 4 compares the raw data taken here with the raw data of the "superpipe" (raw data used so that comparisons made are independent of the correction applied).

All data sets in Figures 3 and 4 clearly collapse very well in the wall region and the same collapse is seen at all other Reynolds numbers tested. It should be noted that only "superpipe" data in the range of Re = $40 \times 10^3$ - $146 \times 10^3$ has been used for comparison, corresponding to the range of measurements taken at Melbourne.

### 3.4 The Log Law Constants

In response to claims of a velocity profile power law, Österlund[2] plots the function $\Theta$ given by:

$$\Theta = \left(y^+\frac{dU^+}{dy^+}\right)^{-1}. \tag{9}$$

If the logarithmic law does exist, $\Theta = \kappa$ in the overlap region. A major problem with plotting this function is that it requires the derivative of data points to be taken and this is not usually an accurate or reliable procedure. The best method found was to use a second order finite difference scheme. The scheme fits a parabola to three data points $y^+_{i+1}$, $y^+_i$ and $y^+_{i-1}$ and the first derivative of that parabola at $y^+_i$ gives the algorithm for the derivative:

$$\left(\frac{dU^+}{dy^+}\right)_i = \frac{U^+_{i+1}(\Delta y^+_i)^2 - U^+_{i-1}(\Delta y^+_{i+1})^2 + U^+_i[(\Delta y^+_{i+1})^2 - (\Delta y^+_i)^2]}{\Delta y^+_i \Delta y^+_{i+1}(\Delta y^+_i + \Delta y^+_{i+1})} \tag{10}$$

This algorithm was applied to data sets of ($\ln y^+$,$U^+$) which is evenly spaced in $\ln y^+$, rather than ($y^+$,$U^+$) in which $y^+$ is spaced almost logarithmically. Figure 5 is a plot of $\Theta$ against $y^+$ for all Reynolds numbers where only data for which $\eta < 0.15$ is included. A constant value of $\Theta = 0.384 \approx \kappa$ appears for $y^+ > 125$ (approx.),

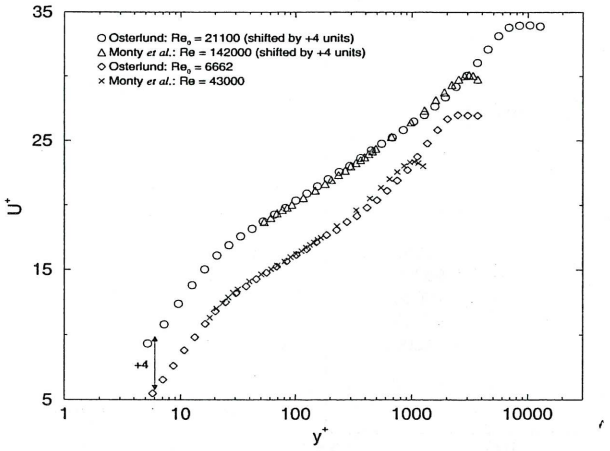


**Figure 3:** Comparison of the authors data (corrected) with Osterlund's data

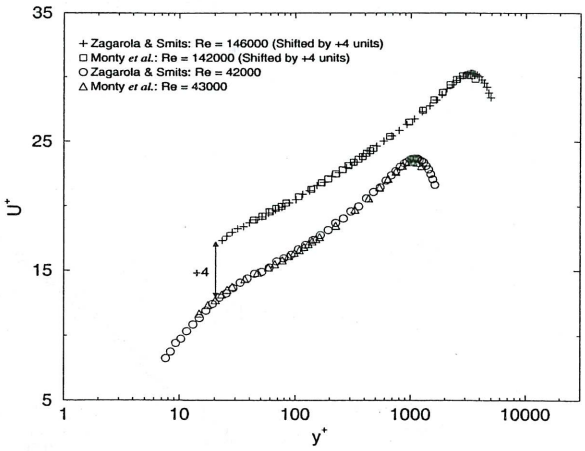


**Figure 4:** Comparison of the author's data with Superpipe data (all uncorrected)

confirming a log law. A slight drop in $\Theta$ for high $y^+$ is evident, indicating more appropriate overlap region limits maybe $y^+ > 100$ and $\eta < 0.1$ as found in Henbest[4] and Perry *et al*[3].

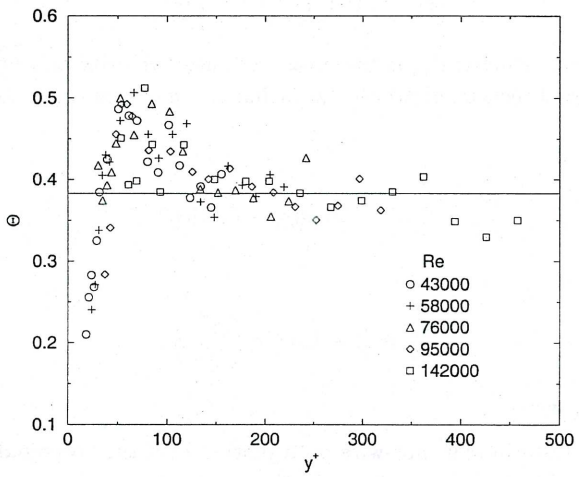


**Figure 5:** A plot of the function $\Theta$ with inner flow scaling

## 4. CONCLUSION

The mean velocity profiles with near wall scaling collapse well onto the logarithmic law of the wall for the whole Reynolds number range studied. Constants in this log law are determined as $\kappa = 0.386$ and $A = 4.21$.

The consistency of these results as compared with Österlund[2] and Perry *et al*.[3] is encouraging. However, it is the results of hot-wire measurements which will be critical in this investigation and it is the intent of this author to complete these measurements thoroughly and promptly.

## 5. REFERENCES

[1]ZAGAROLA, M.V. & SMITS, A.J., "Mean-flow scaling of turbulent pipe flow",*J. Fluid Mech.*, **373**, 33, 1998.
[2]ÖSTERLUND, J.M., "Experimental Studies of Zero Pressure-Gradient Turbulent Boundary-Layer Flow", *Ph.D. thesis,* Department of Mechanics, Royal Institute of Technology, Stockholm, Sweden, 1999.
[3]PERRY, A.E., HAFEZ, S. & CHONG, M.S., "A Possible Reinterpretation of the Princeton Superpipe Data", *J. Fluid Mech.*, Under review, 2001.
[4]HENBEST, S.M., "The Structure of Turbulent Pipe Flow", *Ph.D. thesis,* Department of Mechanical and Manufacturing Engineering, University of Melbourne, Australia, 1983.
[5]MACMILLAN, F.A., "Experiments on Pitot-Tubes in Shear Flow", *Aero. Res. Counc.*,R. & M. 3028, 1957.
[6]PERRY, A.E., HENBEST, S.M. & CHONG, M.S., "A theoretical and experimental study of wall turbulence", *J. Fluid Mech.*, **165**, 163, 1986.
[7]ABELL, C.J., "Scaling Laws for Pipe Flow Turbulence", *Ph.D. thesis,* University of Melbourne, Australia, 1974.

*Melbourne Graduate Fluids Conference, 2001*
*Monash University, Melbourne, Australia*

# Simplified Modelling of Pressure Driven Flow in Pressure Swing Adsorption Processes

**R.S. Todd, C.C.K. Beh, S.J. Wilson and P.A. Webley**

Department of Chemical Engineering
Monash University, Clayton, Victoria, AUSTRALIA

## ABSTRACT

Many Pressure Swing Adsorption (PSA) processes involve the flow of gas through packed beds of zeolite or activated carbon adsorbent particles. Given the inherent non-linear form of the governing partial differential equations that describe the system, a tractable solution cannot be obtained analytically. Hence, a numerical scheme is required to model the complex interactions between the mass, energy and momentum balances. To avoid the complexity of a full Navier-Stokes 3-Dimensional analysis for unsteady-state flow through a packed bed, a convenient approximation for bed pressure drop can be formulated in one spatial dimension using the Ergun equation, which assumes additivity of both the laminar and turbulent flow components. This paper investigates the performance of the Ergun equation against experimental data obtained from a suitably instrumented pilot plant operated under two different flow regimes.

1. Steady state flow of air through a pre-saturated (inert) bed of 5A molecular sieve zeolite.
2. Single step adsorption (breakthrough) study of nitrogen from an air carrier stream over a pre-cleaned bed of 5A molecular sieve zeolite.

## 1. INTRODUCTION

Adsorption involves the migration and subsequent uptake of a species from the bulk fluid phase (either gas or liquid) to a solid surface. Generally most commercial adsorption separation processes utilise synthetic molecular sieve zeolites, which is composed of a crystalline aluminosilicate structure pelletised through the addition of a suitable binding agent [1]. The subsequent adsorbent particle exhibits excellent adsorptive, selectivity and regenerative properties. One process that harnesses the selectivity of these adsorbents is Pressure Swing Adsorption (PSA), with one of the first patents for a commercial PSA cycle awarded to Skarstrom in 1960 [2].
There are two principal steps involved in a typical PSA application.

1. Pressurising the feed stream to pressures above atmospheric (adsorption). This causes the preferentially adsorbed species to be selectively adsorbed from the bulk gas to solid phase.
2. Reducing the total pressure of the bed to atmospheric or sub-atmospheric pressure (desorption). This allows the adsorbent to be regenerated for use during the next adsorption step.

However, most patented PSA processes utilise a series of intermediary steps around those listed above such as low pressure purge and bed-to-bed pressure equalisation to increase process efficiency, improve product recovery and reduce power consumption. Given a typical PSA process can take several thousand cycles to reach Cyclic Steady State [3], the use of a conservative numerical scheme (such as the finite volume method adopted here) is critical to obtain mass and energy balance closure [4]. To adequately capture the sharp wavefront characteristic of convective flow through a packed bed, the QUICK scheme [5] with SMART smoothing [6] is adopted. This approach has been shown in previous studies to correctly model bed dynamics over a range of process conditions [7, 8, 9 10]. This work will demonstrate the validity of the Ergun equation in describing pressure driven flow across a packed bed of 5A molecular sieve zeolite with a comparison to experimental data obtained from a suitably instrumented pilot plant.

## 2. NUMERICAL MODEL

Under pressure swing conditions, an overall mass balance for the system is conveniently written with pressure as the dependent variable, assuming ideal gas behaviour. Under non-isothermal conditions, the overall mass balance for an assumed binary system becomes

$$\frac{\partial p}{\partial t}-\frac{p}{T}\left(\frac{\partial T}{\partial t}\right)=-\frac{T}{\varepsilon_b}\frac{\partial}{\partial z}\left(\frac{up}{T}\right)-\frac{\rho_b RT}{\varepsilon_b}\left(\frac{\partial n_1}{\partial t}+\frac{\partial n_2}{\partial t}\right) \tag{1}$$

where $n_i$ is the moles of species $i$ adsorbed per unit mass of adsorbent, $\varepsilon_b$ the bed voidage and $u$ the superficial velocity. A Linear Driving Force Approximation is applied to the mass transfer term, $\partial n_i/\partial t$ [11]. A species mass balance for component 1 reveals

$$p\frac{\partial y}{\partial t}-\frac{py}{T}\left(\frac{\partial T}{\partial t}\right)+y\left(\frac{\partial p}{\partial t}\right)=-\frac{T}{\varepsilon_b}\frac{\partial}{\partial z}\left(\frac{upy}{T}\right)-\frac{\rho_b RT}{\varepsilon_b}\frac{\partial n_1}{\partial t} \tag{2}$$

The energy balance is formulated on the assumption thermal equilibrium is attained locally between the gas, adsorbed and solid phases. Conditions over which this holds have been investigated [12, 13] and cover the region of interest through this work. The following energy balance is therefore applied.

$$\frac{\partial}{\partial t}\left[\rho_b U_{solid}+\varepsilon_b\rho_{gas}U_{gas}+\rho_b U_{ads}\right]=-\frac{\partial}{\partial z}\left(u\rho_{gas}H_{gas}\right)-\frac{4h_w}{D}\left(T-T_{amb}\right) \tag{3}$$

For convective flow through a packed bed, pressure drop becomes the dominant mechanism for momentum transfer. This can either be modelled empirically or rigorously through the Navier-Stokes equation for each finite volume within the bed. The empirical correlation of Ergun [14] for bed pressure drop has been used in the past with much success, and provides a simplified approach to modelling one-dimensional, steady state flow through a packed bed.

$$-\frac{\partial p}{\partial z}=\left[\frac{1.75(1-\varepsilon_b)\rho_{gas}M_{gas}}{\phi_s\varepsilon_b^3 d_p}\right]u^2+\left[\frac{150\mu_{gas}(1-\varepsilon_b)^2}{\phi_s^2\varepsilon_b^3 d_p^2}\right]u \tag{4}$$

Here, $d_p$ and $\phi_s$ are the diameter and shape factor respectively for the particles, $\mu_{gas}$ the fluid dynamic viscosity and $M_{gas}$ the molecular weight of the gas. The right hand side of equation (4) has two components, with the $u^2$ term relevant over the turbulent flow regime and the $u$ term relevant over the laminar flow regime. The set of coupled PDEs, equations (1) through (3) above are discretised in the axial domain and solved in the temporal domain using LSODA, a stiff/non-stiff, variable time step ODE solver [15].

## 3. RESULTS AND DISCUSSION

### 3.1 EXPERIMENTAL PILOT PLANT

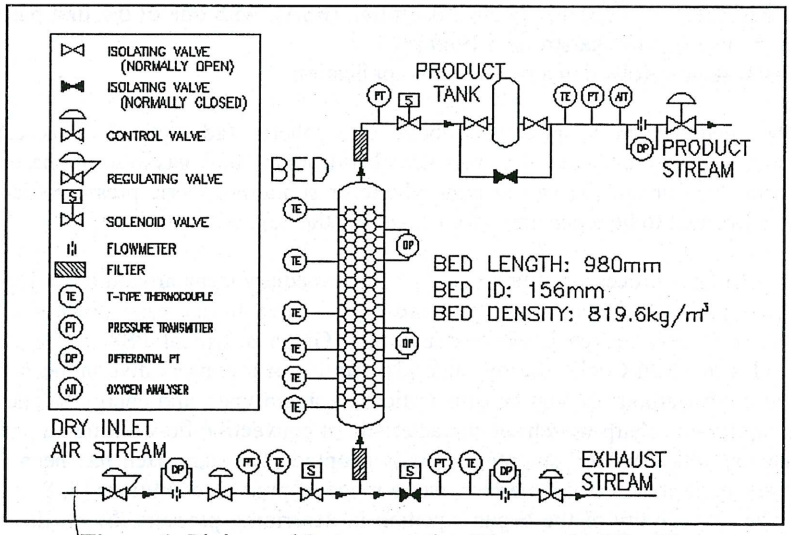


**Figure 1:** Piping and Instrumentation Diagram for Pilot Plant.

The adsorbent bed is composed of a homogenous, single layer of 16×40 mesh 5A (calcium exchanged) molecular sieve zeolite that selectively adsorbs nitrogen from a nitrogen-oxygen gas mixture. The use of small bead 5A particles ensures a significant pressure profile exists over the axial domain of the adsorbent bed, providing a good test of the Ergun equation. There are two differential pressure transducers located across the adsorbent bed. The first lies between axial points z=20mm and z=400mm and the second between points z=475mm and z=850mm. Pressure transducers and flow

meters are located on the inlet and outlet lines to and from the process. To monitor temperature variations in the system, 10 thermocouples within the adsorbent bed and thermocouples on each of the inlet and outlet lines are logged every 0.5 seconds.

### 3.2 STEADY STATE FLOW THROUGH AN INERT BED

Once the adsorbent bed of Figure 1 is saturated with feed air, adsorption/desorption of material to or from each zeolite particle no longer occurs. Hence, the zeolite behaves as an inert packed bed and the adsorption derivatives, $\partial n_i/\partial t$ of equations (1) and (2) are subsequently zero. Once saturation of the bed had occurred, bed profiles and flow rates at steady state were logged. To simulate this numerically, the use of a valve CV equation [7] at the inlet and experimental molar flow rate at the outlet were set as boundary conditions and the resulting pressure profile for the bed obtained.

| System | Mole Flow Out | Outlet Pressure | DP1 (Lower) | DP2 (Upper) |
|---|---|---|---|---|
| Experimental | 0.2786 gmole/s | 190.5 kPa.abs | 6.75 kPa | 7.99 kPa |
| Simulated | 0.2786 gmole/s$^{\#}$ | 190.4 kPa.abs | 7.05 kPa | 7.26 kPa |

**Table 1:** Experimental and Simulated results.($^{\#}$ Set as a Boundary Condition to the Simulator)

Slight deviations in the order of half a kilopascal are seen for the two regions of the bed, within experimental error for the measured values. Particle diameter for this material was taken to be 0.64 mm, with a shape factor of 0.80.

### 3.3 ONE STEP BREAKTHROUGH STUDY

A single step breakthrough study analyses the response of an initially clean bed of adsorbent particles to a step change in sorbate concentration at the inlet [16, 17]. For our case, the bed was pre-saturated with a certified 90 % oxygen/10 % nitrogen mixture. From these initial conditions, the bed was then exposed to a step change in nitrogen composition (air) and the resulting pressure profiles logged with time. To compare this with the numerical model (Figure 2 below), initial conditions for the bed were set to that of the pre-satuarated composition and the boundary conditions allowed for inlet and outlet pressure to change with time. Nitrogen breakthrough was complete after 45 seconds. Given the initial conditions are different to the feed conditions, the numerical model must now allow for adsorption phenomena within the bed, which acts to remove gas from the bulk phase and alter the pressure profile from steady state conditions.

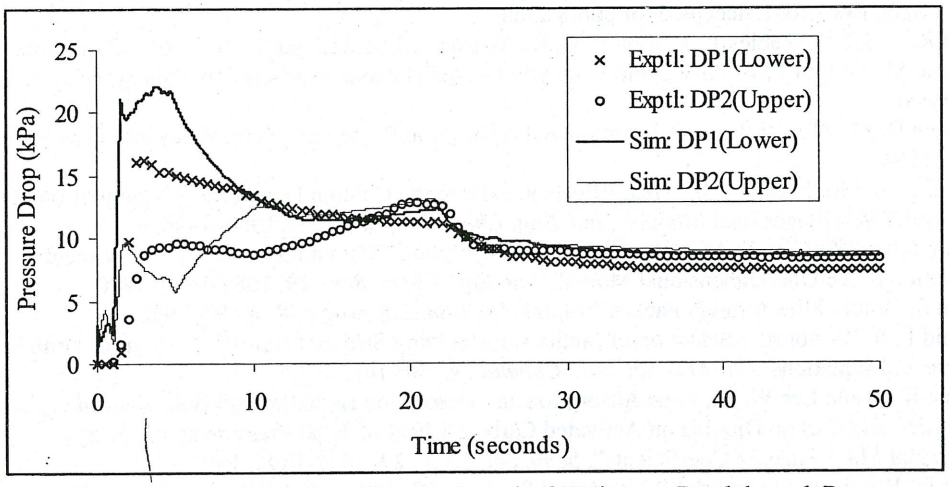


**Figure 2:** Experimental and Simulated results for Nitrogen Breakthrough Run.

Qualitative trends in pressure, such as the initial spike which asymptotes towards the steady state profile at the onset of breakthrough (45 seconds) is captured within the model. Given the Ergun equation considers steady state flow only and is a function of particle size, distribution and shape,

relatively good agreement is seen for bed profiles. A maximum error of approximately 6 kPa (across the lower region of the bed) is seen when the bed is initially pressurised.

## 4. CONCLUSION

The ability of a simplified flow model, the Ergun Equation, in capturing pressure and flow profiles has been demonstrated for two different flow regimes within an adsorption system for (a) Flow through an inert bed of zeolite and (b) the Breakthrough of nitrogen over a pre-cleaned bed of 5A zeolite. Numerical results obtained with the Ergun Equation for these cases provides a good representation of experimental data and eliminates the requirement of a 3-Dimensional Navier-Stokes model for pressure driven flow within a PSA system. However, better characterisation of non-spherical material with significant deviations in size distribution, such as 5A zeolite, is important to improve process model mismatch in cyclic adsorption simulation.

## 5. REFERENCES

1. Yang R., "Gas Separation by Adsorption Processes", Butterworths, MA, 1987
2. Skarstrom C. W., "Method and Apparatus for Fractionating Gaseous Mixtures by Adsorption" US Patent 2,944,627 (July 1960)
3. He J. and Webley P. A., "Criteria for Establishing Cyclic Steady State for Non-Isothermal Cyclic Adsorption Systems", 2001, *Submitted*
4. Botte G. G., Ritter J. A. and White R. E., "Comparison of Finite Difference and Control Volume Methods for Solving Differential Equations", *Compt. Chem. Eng.*, **24**, 2633-2654, 2000
5. Leonard B. P., "A Stable and Accurate Convective Modelling Procedure based on Quadratic Upstream Interpolation", *Comp. Meth. Appl. Mech. & Eng.*, **19**, 59-98, 1979
6. Gaskell P. H. and Lau A. K. C., "Curvature-Compensated Convective Transport: SMART, A new Boundedness-Preserving Transport Algorithm", *Int. J. Num. Meth. Fluids*, **8**, 617-641, 1988
7. Webley P. A. and He J., "Fast Solution-Adaptive Finite Volume Method for PSA/VSA Cycle Simulation; 1 Single Step Simulation", *Compt. Chem. Eng.*, **23**, 1701-1712, 2000
8. Webley, P. A., Beh C., He J., Wilson S. and Todd R. S., "Numerical Simulation and Experimental Validation of Multiple-Layer, Non-Isothermal, Bulk gas Pressure Swing Adsorption", *Proc. 2nd. Pacific Basin Conf. Adsorption Sci. & Tech.*, Ed. D. Do, 14-18 May 2000 (World Scientific, Sing.)
9. Wilson S. J., Beh C. C. K., Webley P. A. and Todd R. S., "The Effects of a Readily Adsorbed Trace Component (Water) in a Bulk Separation PSA Process: The Case of Oxygen VSA", *Ind. Eng. Chem. Res.*, 2001, accepted for publication
10. Todd R. S., He J., Webley P. A., Beh C. C. K., Wilson S. J. and Lloyd M. A., 2001, "Fast Finite Volume Method for PSA/VSA Cycle Simulation – Analytic and Experimental Validation", 2001, *submitted*
11. Ruthven D. M., "Principles of Adsorption and Adsorption Processes", John Wiley and Sons, New York, 1984
12. Farooq S. and Ruthven D. M., "Heat Effects in Adsorption Column Dynamics. 1. Comparison of One- and Two-Dimensional Models", *Ind. Eng. Chem. Res.*, **29**, 1076-1084, 1990
13. Farooq S. and Ruthven D. M., "Heat Effects in Adsorption Column Dynamics. 2. Experimental Validation of the One-Dimensional Model", *Ind. Eng. Chem. Res.*, **29**, 1084-1090, 1990
14. Ergun S., "Fluid Flow through Packed Columns", *Chem.Eng.Prog.*, **48**, 89-92, 1952
15. Petzold L. R, "Automatic Selection of Methods for Solving Stiff and Nonstiff Systems of Ordinary Differential Equations", *SIAM J. Sci. Stat. Comput.*, **4**, 136-148, 1983
16. Hwang K. S. and Lee W. K., "The Adsorption and Desorption Breakthrough Behaviour of Carbon Monoxide and Carbon Dioxide on Activated Carbon. Effect of Total Pressure and Pressure-Dependent Mass Transfer Coefficients", *Sepn. Sci. Tech.*, **29**, 1857-1891, 1994
17. Foeth F., Bosch H., Sjöstrand A., Aly G. and Reith T., "Equilibrium Adsorption Data from Breakthrough Curves with Variable Velocity and Pressure", *Sepn. Sci. Tech.*, **31**, 21-38, 1996

*Melbourne Graduate Fluids Conference, 2001*
*Monash University, Melbourne, Australia*

# THE EFFECT OF TURBULENCE ON THE PERFORMANCE OF A SMALL WIND TURBINE

**K. E. SWALWELL, J. SHERIDAN and W. H. MELBOURNE**

Department of Mechanical Engineering
Monash University, Clayton, Victoria, AUSTRALIA

## ABSTRACT

The BEM method is used to predict the power produced by horizontal axis wind turbines. However, turbines produce more power than expected where the BEM method predicts the blades stall. What causes this "delayed stall" effect is difficult to determine. By comparing the performance of a small turbine in a low turbulence wind tunnel environment and in the natural turbulence of a field environment the effect of turbulence was observed. Higher turbulence levels increased performance in a way consistent with "delayed stall". Further work is being undertaken to quantify the effect of turbulence on aerofoil performance.

## 1. INTRODUCTION

Electricity production is the largest single contributor to greenhouse gas emissions in Australia (Australian Greenhouse Gas Office, 2000). Wind turbines have been adopted worldwide as an alternative to burning fossil fuels, e.g. Lemming & Anderson (1999) showed wind power produced 8.6% (2779 GWh) of Danish electricity supply in 1998. Predicting the aerodynamic performance of wind turbines is important in evaluating the power production of different designs. It also determines the strength and fatigue resistance turbines require to survive their design lifetime.

This paper will only discuss horizontal axis wind turbines (HAWTs), which are far more common than vertical axis designs. The Blade Element Momentum (BEM) method is commonly used to predict the aerodynamic performance of HAWTs; it uses the results of aerofoil section test to predict the aerodynamic performance of a rotating blade element. Due to the blades rotation and the expansion of the wake behind the rotor the angle of attack varies with the wind speed. As the wind speed increases the angle of attack increases.

The BEM method predicts performance well when wind turbines are operating at angles of attack below where the aerofoil sections stall in the wind tunnel and at small yaw errors (where yaw is the angle between the rotational axis of the turbine and the wind direction). Van Grol, Snel & Schepers (1991) (as quoted in Hansen & Butterfield (1993)) found that the BEM method predicts power and annual energy yield to an accuracy of ±8% for such conditions. However the BEM method consistently underpredicts the turbines performance at wind speeds that correspond to angles of attack above stall on the aerofoil section. Even turbines that pitch the blades (change their angle) to avoid stall do not avoid the extra load, as the pitching mechanisms are too slow to avoid stall conditions during wind gusts.

The data shown in Figure 1A is from NREL's 10 m diameter turbine, as reported by Simms *et al.* (1999). Each data point was obtained by selectively averaging data during periods of steady wind and minimal yaw. The averaged data represents less than 1% of the total measurements. In Figure 1B the same data is replotted in the non-dimensional form commonly used to compare the performance of different wind turbines. The power coefficient ($C_P$) is the ratio of the power produced to the power available in the wind.

$$C_P = \frac{P}{\frac{1}{2}\rho A V^3} \tag{1}$$

where $P$ is the power output, $\rho$ is the fluid density, $A$ is the rotor area and $V$ is the freestream velocity. The tip speed ratio ($\lambda$) is the ratio of the speed of the end of the blades to the freestream velocity.

$$\lambda = \frac{\omega R}{V} \tag{2}$$

where $\omega$ is the rate of rotation and $R$ is the radius of the turbine rotor.

The large scatter at high tip speed ratios in Figure 1B is due to amplification of scatter in the low wind speed data by the unit conversion. Small errors in $V$ are increased by the power in the $C_P$ equation.

The circled areas in Figure 1A and B show where "delayed stall" occurs on a rotating turbine.

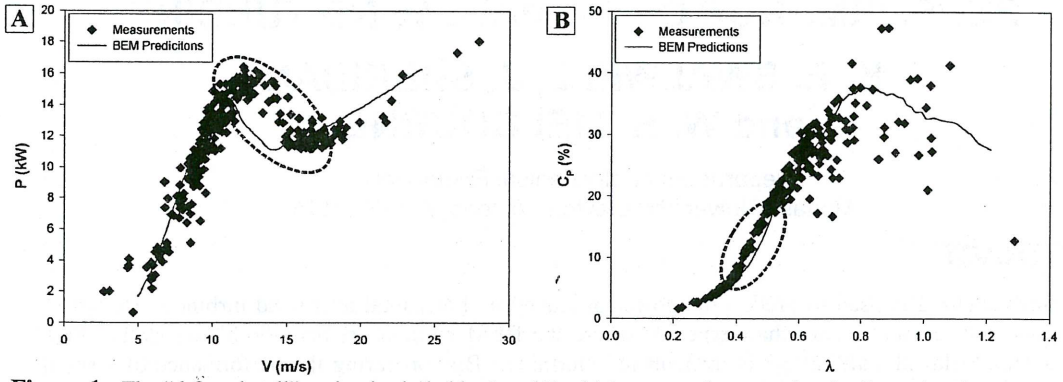


**Figure 1** : The "delayed stall" region is circled in A and B which present the same data in dimensional and non-dimensional units respectively (data from the NREL Unsteady Aerodynamics Experiment Simms *et al.*, 1999).

The uncertainty in the loads at high wind speeds due to "delayed stall" means that turbines are frequently over designed to avoid failure. This increases the weight of the turbine and therefore the material cost of the turbine and tower. A better understanding of "delayed stall" could allow designers to make more accurate predictions and therefore minimise material costs. It may even enable designs that maximise the use of the increased power available in this region.

There are numerous theories about the cause of "delayed stall". Full scale experiments in natural wind have had difficulty quantifying the different effects. Madsen & Christensen (1990) examined a 19 m diameter turbine in the field and found "delayed stall" both when the blades were rotating and when they were not, although the maximum lift in the second case was lower. Blade sections tested in wind tunnels with controlled turbulence have also found "delayed stall", as shown in Figure 2.

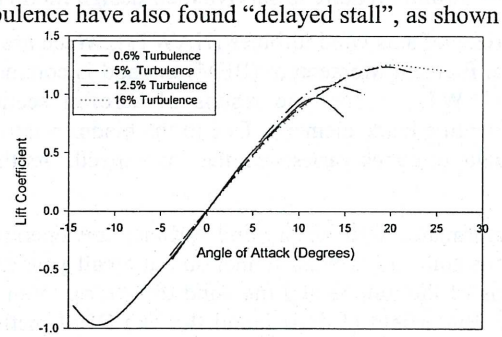


**Figure 2** : Performance of a NACA 0006 Aerofoil in Turbulence at $Re_c \sim 2x10^5$ (Jancauskas, 1983)

However, Simms *et al.*'s (1999) measurements in the low turbulence of the NREL baseline cycles and Clausen *et al.*'s (1987) wind tunnel study of a shrouded turbine also found "delayed stall". This seems to indicate that there are other important effects. Schreck *et al.*'s (2000) investigation found yaw also played an important part in the turbine response.

The current investigation compares the performance of a small turbine operating in low turbulence wind tunnel environment with the results obtained in a natural turbulence field environment to isolate the effect of turbulence on turbine performance.

## 2. EXPERIMENTAL METHOD

The data analysed in this paper was kindly supplied by Dr. Gholam Riahy Dehkordi (1999) who collected it as part of his doctoral thesis on designing a predictive controller for a wind turbine. He used a Rutland 910 wind turbine that had a variable rotational speed. The manufacturers specify this turbine produces a peak power output of 50 W at a wind speed of 10m/s. The turbine used was identical to that shown in Figure 3 except it had 12 mm wide metal struts between the blades (these were attached 107 mm from the end of the blades). Unfortunately the unusual construction of this turbine (thin blades and bracing between the blades) prevented use of the BEM method to predict performance.

The turbine was tested under different loads in the 450 kW wind tunnel at Monash University. To obtain the power curve the wind speed was held constant at 5.94 m/s and the load was varied resulting

in different rotational speeds and therefore different tip speed ratios. The tunnel and turbine were run for 15 minutes to obtain a steady temperature. Then the power output and the resistances of the generator were measured and, by correcting for generator performance, the power from the blades determined. To get measurements near stall a dynamic controller was developed by Riahy & Freere (1997) to ensure the blades remained at an appropriate tip speed ratio.

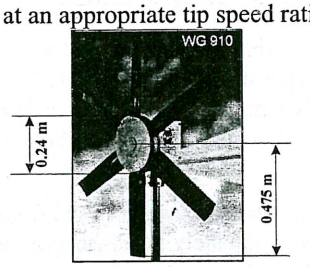


**Figure 3 :** Rutland WG 910

The field data was obtained using the same wind turbine placed on a tower on the roof. Three anemometers placed around the turbine measured the wind speed. The inertia of the blades caused changes in tip speed and power to lag the changes in wind speed during wind gusts. The field readings were averaged to minimise this effect. Most of the field measurements used were part of the testing of Gholam Dehkordi's load controller. This data was obtained from 24 hour runs with the controller alternately on (the high $C_P$ data) and off (the lower $C_P$ data). The number and size of these runs allowed a long averaging time (780 seconds). There was only a few short runs of data available at high tip speed ratios so this data was averaged over a relatively short time (200 seconds) to provide a reasonable number of data points in this region for the polynomial fit.

## 3. RESULTS AND DISCUSSION

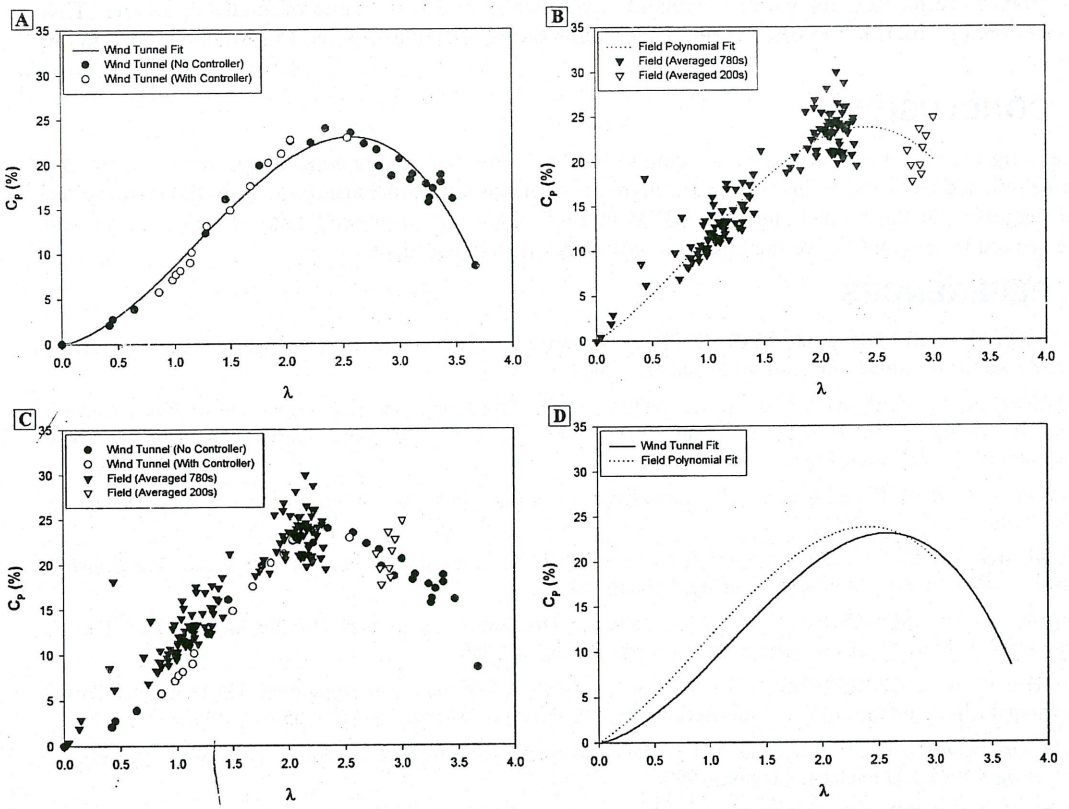


**Figure 4 :** Wind Tunnel and Field Data. (A and B show the wind tunnel and field data along with their respective fitted curves. C plots all the data points for comparison and D does the same for the fitted curves).

Figure 4A shows the measurements obtained in the wind tunnel. The data taken using the controller to maintain a constant rotational speed is indicated. A third order polynomial, constrained to pass through the origin, was fitted to the data to aid comparison (the equation is given below).

$$C_P = -2.315\lambda^3 + 8.403\lambda^2 + 2.622\lambda \qquad (3)$$

The field data, shown in Figure 4B, was averaged to minimise the effects of the inertia of the rotor on results. The polynomial fit was done in the same way as for the wind tunnel data; the fitted equation is given below.

$$C_P = -1.989\lambda^3 + 5.449\lambda^2 + 8.282\lambda \quad (4)$$

Figure 4C is a combined plot of both the wind tunnel and field data. In the "delayed stall" region the power coefficient for the field data is higher than for the low turbulence wind tunnel data. This can be seen more clearly by comparing the polynomial fits, as shown in Figure 4D. Unfortunately there was no field data at very high tip speed ratios so the effect of turbulence at tip speed ratios above three could not be evaluated.

The wind turbine investigated was an upwind turbine that used a tail vane to angle it into the wind. The placement in the field also had a predominately north-easterly wind whose direction varied little. These factors should ensure that any yaw error was minimal.

The 450 kW wind tunnel has a turbulence intensity of 0.06%, while the average turbulence intensity in the field was 18% (ranging from 9% to 36%). Figure 4 shows the performance in the stall region was altered by the turbulence levels. This change in performance with turbulence is worth further investigation.

## 4. FURTHER WORK

Turbulence is known to increase the lift and drag of aerofoils at high angles of attack. However there has been surprisingly little research done on the phenomena, presumably because it has little impact on the performance of aircraft aerofoils, whose motion effectively reduces the turbulence intensity encountered. It is planned to measure the effect of turbulence on a thick aerofoil section, similar to those used near the hub of wind turbines, the area of the blade that is predicted to stall first. Experiments are planned for various levels of turbulence over a wide range of angles of attack. This data will then be used in the BEM method and the predicted output compared to results obtained in the field.

## 5. CONCLUSION

Comparing the performance of a small wind turbine in a low turbulence wind tunnel environment and high turbulence field environment showed higher turbulence levels increased power in the stall region. This suggests that the predictions of the BEM method in the region where "delayed stall" occurs may be improved by accounting for the effects of turbulence on performance.

## 6. REFERENCES

AUSTRALIAN GREENHOUSE GAS OFFICE, "Overview: 1988 National Greenhouse Gas Inventory", Commonwealth Government of Australia, Canberra, 2000.

CLAUSEN, P. D., PIDDINGTON, D. M. & WOOD, D. H., "An Experimental Investigation of Blade Element Theory for Wind Turbines. Part 1. Mean Flow Results", *Journal of Wind Engineering and Industrial Aerodynamics*, **25**, 189-206, 1987.

HANSEN, A. C. & BUTTERFIELD, C. P., "Aerodynamics of Horizontal-Axis Wind Turbines", *Annual Review of Fluid Mechanics*, **25**, 115-149, 1993.

JANCAUSKAS, E. D., "The Cross-Wind Excitation of Bluff Structures and the Incident Turbulence Mechanism", *Mechanical Engineering*, Monash University, Clayton, 1983.

LEMMING, J. & ANDERSON, P. D., "Wind Power in Denmark - Technology Policies and Results", Danish Energy Agency, Ministry of Environment and Energy, Denmark, 1999.

MADSEN, H. A. & CHRISTENSEN, H. F., "On the Relative Importance of Rotational, Unsteady and Three-Dimensional Effects on the HAWT Rotor Aerodynamics", *Wind Engineering*, **14** (6), 405-415, 1990.

RIAHY DEHKORDI, G. H., "Dynamic and predictive dynamic wind turbine control", *Department of Electrical Engineering*, Monash University, Clayton, 1999.

RIAHY, G. & FREERE, P., "Dynamic Controller to Operate a Wind Turbine in Stall", *Solar '97*, Canberra, Australia, 1997.

SCHRECK, S. J., ROBINSON, M. C., HAND, M. M. & SIMMS, D. A., "HAWT Dynamic Stall Response Asymmetries Under Yawed Flow Conditions", NREL - National Renewable Energy Laboratory, Golden, Colorado, 2000.

SIMMS, D. A., SCHRECK, S. J., HAND, M. M., FINGERSH, L., COTRELL, J., PIERCE, K. & ROBINSON, M. C., "Plans for Testing the NREL Unsteady Aerodynamics Experiment 10-m Diameter HAWT in the NASA Ames Wind Tunnel", National Renewable Energy Laboratory (NREL), Golden, Colorado, 1999.

*Melbourne Graduate Fluids Conference*
*Monash University, Melbourne, Australia*

# Validation of a Code for Aeroelasticity Turbomachinery

**Ivan McBean, Kerry Hourigan, Mark Thompson**

Department of Mechanical Engineering
Monash University, Clayton, Victoria, AUSTRALIA

**Feng Liu**

Department of Mechanical and Aerospace Engineering
University of California, Irvine, CA 92697-3975 USA

## ABSTRACT

A multiblock method is presented for the solution of a three dimensional model of aeroelasticity in a turbomachine blade row. The method employs a fully coupled approach and the structural model involves modal reduction. This paper presents the computational model and its validation.

## 1. INTRODUCTION

As designers in the turbomachinery industry strive to design machines that are lighter, more powerful and more efficient, blade flutter has become one of the most important limiting factors on the design process. The aeroelastic response is a complex phenomenon that is not well modeled or predicted by current design techniques. Codes that implement 2-dimensional models can simulate this behaviour in a meridional plane, however the flow structures found in blade passages are generally three dimensional and such models provide a qualitative rather than quantitative analysis. Furthermore, important flow phenomena are not modeled including hub and casing vortices and tip effects.

A structured 3-dimensional Navier-Stokes code is developed to solve the unsteady governing equations. These are solved using an explicit Runge-Kutta scheme, implementing residual averaging and multigrid. The problem is then solved in a time accurate manner through a fully implicit scheme as proposed by Jameson [6]. This scheme has already been used in a 2-dimensional model of aeroelasticity in turbomachinery [15, 7]. The development of the present code is an extension of the previous 2-dimensional method to 3 dimensions. Similar algorithms have been successfully implemented in a 3-dimensional Navier-Stokes external solver that models flow over a flexible wing [16, 8].

## 2. FLUID MODEL

The present 3 dimensional multiblock and parallel code has been developed from a proven steady solver designed to model turbomachinery cascade flow [10, 9, 13, 17, 14, 11]. The governing equations for the unsteady fluid problem in a Eulerian reference frame with a moving mesh.

$$\frac{\partial}{\partial t}\iiint_{\Omega} \mathbf{w}\, d\Omega + \oint \mathbf{f}\, dS_x + \mathbf{g}\, dS_y + \mathbf{h}\, dS_z = 0 \tag{1}$$

where

$$\mathbf{w} = \begin{pmatrix} \rho \\ \rho u \\ \rho v \\ \rho w \\ \rho E \end{pmatrix} \tag{2}$$

$$\mathbf{f} = \begin{pmatrix} \rho\bar{u} \\ \rho u\bar{u} + p \\ \rho v\bar{u} \\ \rho w\bar{u} \\ \rho E\bar{u} + pu \end{pmatrix}, \quad \mathbf{g} = \begin{pmatrix} \rho\bar{v} \\ \rho u\bar{v} \\ \rho v\bar{v} + p \\ \rho w\bar{v} \\ \rho E\bar{v} + pv \end{pmatrix}, \quad \mathbf{h} = \begin{pmatrix} \rho\bar{w} \\ \rho u\bar{w} \\ \rho v\bar{w} \\ \rho w\bar{w} + p \\ \rho E\bar{w} + pw \end{pmatrix} \tag{3}$$

The time dependent and semi-discrete form of the governing equations may be written as

$$\frac{d\mathbf{w}}{dt} + R(\mathbf{w}) = 0 \tag{4}$$

A dual time stepping scheme [6] is used to calculate the unsteady flow problem. A second order accurate, fully implicit scheme is used to integrate Equation (4) to evolve the unsteady problem in a time accurate manner.

The discrete form of (4) is

$$\frac{3w^{n+1} - 4w^n + w^{n-1}}{2\Delta t} + R(w^{n+1}) = 0 \tag{5}$$

This equation may be recast into

$$\frac{d\mathbf{w}}{dt^*} + R^*(\mathbf{w}) = 0 \tag{6}$$

where

$$R^*(\mathbf{w}) = \frac{3w}{2\Delta t} + R(w) - \frac{2}{\Delta t}w^n + \frac{1}{2\Delta t}w^{n-1} \tag{7}$$

The steady state solution $w$ in equation (6) is then equivalent to the time accurate solution $w^{n+1}$ to equation (5). Any efficient algorithm may be used to obtain the steady-state solution to (6). In this paper, the above mentioned Runge-Kutta type scheme with multigrid is used. Minimum modification of the steady solver to make it time accurate in the above manner.

# 3. STRUCTURAL MODEL

Modal decomposition, otherwise known as the Rayleigh Ritz approach, reduces the structural problem to a series of uncoupled, second order differential equations. These are reduced to first order differential equations and solved by the same dual time stepping method as that for the flow equations. The problem is first solved in pseudo time using a Runge-Kutta scheme, then advanced it time through an implicit time accurate formulation [1, 2].

# 4. MULTIBLOCK & PARALLEL IMPLEMENTATION

A multiple block method involving of structured grids is used to make the best use of computational resources and to allow the generation of grids for complex geometries. While each block consists of a structured grid, the blocks can be connected to each other in an unstructured manner provided the mesh geometry is matched at the block interfaces. The Message Passing Interface (MPI) is used for interblock communication.

# 5. MODEL VALIDATION

## 5.1 Unsteady Cylinder

The low Reynolds number, unsteady cylinder is a well documented case in both experimental and numerical fields. In this case it was used to check the time accuracy of the unsteady implementation. A single block O-grid was generated with the far-field boundary approximately 50 chords from the cylinder surface. The code may only calculate for 3-dimensional mesh geometries, so 2 cells were used in the span-wise direction. The Mach number of the compressible solver was set at 0.2 as at this value, the effects of compressibility are assumed to be negligible. The Strouhal number for a grid of 196 x 96 x 3 was calculated as 0.181, which is close to the experimental value of 0.182.

## 5.2 Forced Airfoil Oscillation

To demonstrate the validity of the moving mesh, multiblock and unsteady implementation, the NACA64A010 case is presented. Computational results are compared in Figure 1 for different configurations also with experimental results. An unsteady Euler calculation is performed in the flow solver. In the first case, a single block O-grid is used in combination with TFI to deform the grid to the oscillating airfoil. The far field boundary remains rigid. The second case involves a mesh that is not deformed, but rotates rigidly with the displacement of the airfoil surface. For the third calculation, the same grid as used for the single block cases is divided into 32 equal blocks, with 4 blocks in the radial direction and 8 in the circumferential direction. In this case the block corners were located using the spring analogy. The results for inviscid flow compare similarly with results presented elsewhere [12, 1] and there is little difference between the results for the different configurations.

## 5.3 Coupled Airfoil Oscillation

The modeling of aeroelasticity requires the simulation of the interaction of elastic member with an unsteady flow. One of the simplest examples is Isogai's wing model [4, 5], a 2-dimensional NACA64A010 airfoil that has been

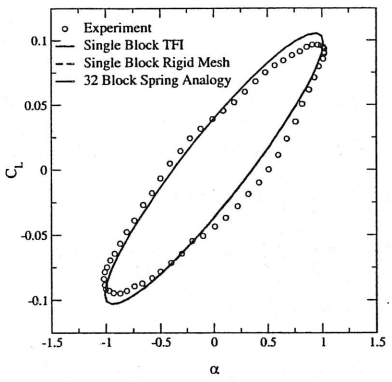


Figure 1: Comparison of unsteady NACA64A010 results with experiment.

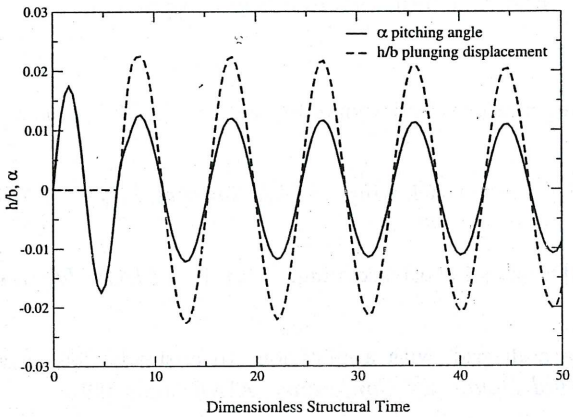


Figure 2: Stable case; $M_\infty = 0.825$, $V_f = 0.630$.

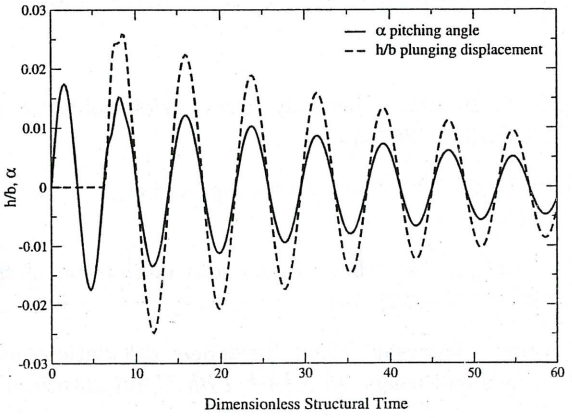


Figure 3: Damped case; $M_\infty = 0.825$, $V_f = 0.530$.

studied numerically by a number of authors [1, 8]. Experimental unsteady flow measurements are available for the airfoil for forced oscillation and these results may be used to validate the unsteady flow model.

The wing is modelled by connecting a spring to the torsion and plunging axis of the NACA64 airfoil section. The section is held by a pin at the torsion axis and force for one period of oscillation whereupon the pin is released and the amplitudes of pitching and plunging. The behaviour depends on the non-dimensional parameter of flutter velocity. An example of neutrally stable, unstable and damped configurations and results are shown in Figures 2 to 4. The a plot of the flutter boundary of the configuration is shown in Figure 5, the point at which the configuration changes from being stable to unstable.

## 6. CONCLUSION

A novel multiblock and parallel, integrated structural and fluid solver has been presented. The implementation is general and is not limited to particular geometries and thus is flexible in that it may be applied to a broad range of problems. The moving mesh and structural model allow for the coupled solution of aeroelastic problems.

A number of different cases have been presented that compare computed results with experiment or other numerical results. Navier-Stokes solution of the flow past a circular cylinder compares well with experimental data. The code is also validated for the unsteady flow around a pitching airfoil with either a rigid grid or a deforming grid generated by a multiblock TFI method. Coupled flow and structure solution for an airfoil with two-degrees of freedom demonstrate the ability of the code to simulate coupled aeroelasticity.

## References

[1] Juan Alonso and Antony Jameson. Fully-implicit time-marching aeroelastic solutions. In *AIAA 32nd Aerospace Sciences Meeting*. AIAA, January 1994. 94-0056.

[2] Juan Jose Alonso. *Parallel Computation of Unsteady and Aeroelastic Flows Using an Implicit Multigrid-Driven Algorithm*. PhD thesis, Pinceton University, June 1997.

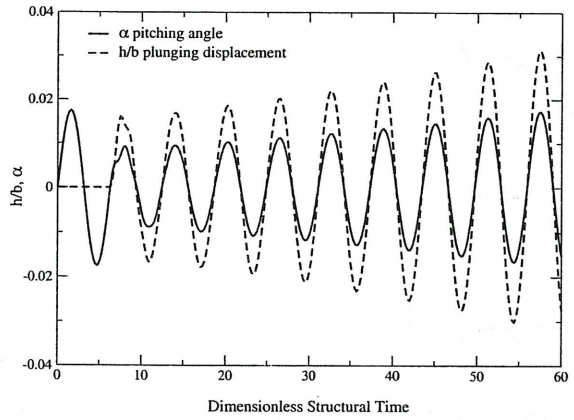


Figure 4: Diverging case; $M_\infty = 0.825$, $V_f = 0.725$.

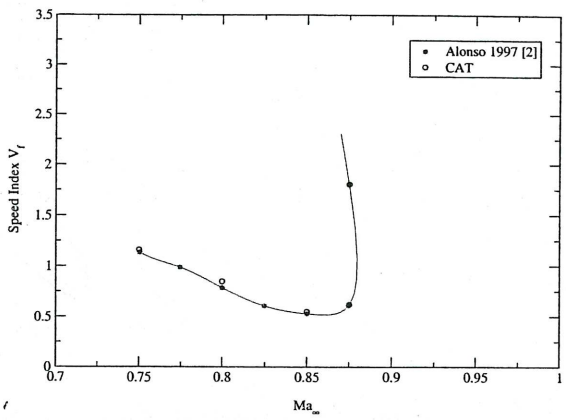


Figure 5: Flutter boundary comparison.


[3] J. T. Batina. Unsteady Euler airfoil solutions using unstructured dynamic meshes. *AIAA Journal*, 28(8):1381–1388, 1990.

[4] K. Isogai. On the transonic-dip mechanism of flutter of a sweptback wing. *AIAA Journal*, 17(7):793–795, 1979.

[5] K. Isogai. On the transonic-dip mechanism of flutter of a sweptback wing: Part ii. *AIAA Journal*, 19(7):1240–1242, 1981.

[6] Antony Jameson. Time dependent calculations using multigrid, with applications to unsteady flows past airfoils and wings. In *AIAA 10th Computational Fluid Dynamics Conference*. AIAA, June 1991.

[7] Shanhong Ji and Feng Liu. Flutter computation of turbomachinery cascades using a parallel unsteady Navier-Stokes code. *AIAA Journal*, 37(3):320–327, March 1999.

[8] F. Liu, J. Cai, Y. Zhu, and H. M. Tsai A. S. F. Wong. Calculation of wing flutter by a coupled CFD-CSD method. In *AIAA 38th Aerospace Sciences Meeting & Exhibit*. AIAA, January 2000. AIAA 2000-0907.

[9] Feng Liu and Antony Jameson. Cascade flow calculations by a multigrid Euler method. *Journal of Propulsion and Power*, 9(1):90–97, January 1993.

[10] Feng Liu and Antony Jameson. Multigrid Navier-Stokes calculations for three-dimensional cascades. *AIAA Journal*, 31(10):1785–1791, October 1993.

[11] Feng Liu, Ian K. Jennions, and Antony Jameson. Computation of turbomachinery flow by a convective-upwind-split- pressure (CUSP) scheme. In *36th Aerospace Sciences Meeting and Exhibit*. AIAA, January 1998.

[12] Feng Liu and Shanhong Ji. Unsteady flow calculations with a multigrid navier-stokes method. *AIAA Journal*, 34(10):2047–2053, October 1996.

[13] Feng Liu and Xiaoqing Zheng. Staggered finite volume scheme for solving cascade flow with a k-$\omega$ turbulence model. *AIAA Journal*, 32(8):1589–1597, August 1994.

[14] Feng Liu and Xiaoquing Zheng. A strongly coupled time-marching method for solving the Navier- Stokes and k-$\omega$ turbulence model equations with multigrid. *Journal of Computational Physics*, 128:289–300, 1996.

[15] M. Sadeghi and F. Liu. Computation of mistuning effects on cascade flutter. In *AIAA 38th Aerospace Sciences Meeting & Exhibit*. AIAA, January 2000. AIAA 2000-0230.

[16] A. S. F. Wong, H. M. Tsai, J. Cai, Y. Zhu, and F. Liu. Unsteady flow calculations with a multi-block moving mesh algorithm. In *AIAA 38th Aerospace Sciences Meeting & Exhibit*. AIAA, January 2000. To be Presented, AIAA 2000-1002.

[17] Xiaoqing Zheng and Feng Liu. Staggered finite volume scheme for solving Navier-Sokes and k-$\omega$ turbulence model equations. *AIAA Journal*, 33(6):991–998, June 1995.

*Melbourne Graduate Fluids Conference, 2001*
*Monash University, Melbourne, Australia*

# Effects of turbulence integral length scale on a Smooth Cylinder's axial correlation length at Critical and Supercritical Reynolds numbers

**M. Eaddy, W.H. Melbourne and J. Sheridan**

Department of Mechanical Engineering
Monash University, Clayton, Victoria, AUSTRALIA

## ABSTRACT

Measurements have been made of the axial correlation length on a smooth circular cylinder in low and high turbulent flow conditions. For the high turbulence flow the integral length scales were varied between 0.7D and 2D. The results for the low turbulence and high turbulence with integral scales smaller than the cylinder diameter agree well with published results. At the higher turbulence conditions with integral scales larger than the cylinder diameter it was found that the axial correlation length increased with turbulence intensity, peaking at values of approximately 3 diameters. It is postulated that this increase is caused by interaction between the transverse component of the turbulence vortices and the vortices being shed from the cylinder.

## 1. INTRODUCTION

The critical regime for a smooth circular cylinder is identified by a pronounced decrease in the mean drag coefficient from approximately 1.2 at Re~$1.5\times10^5$ to 0.25 at Re~$4\times10^5$. The Reynolds number at which the mean drag attains a minimum value is termed the critical Reynolds number and indicates the beginning of the supercritical regime (Roshko, 1961). The axial correlation length undergoes a similar decrease in value over this Reynolds number range, dropping from 3-6 diameters to ~1 diameter at the critical Reynolds number and maintaining this value in the supercritical regime (King, 1977). Zdravkovich (1997) describes the mechanism that causes this transition as a reduction in the stability of the wake region as the separation point moves rearwards and the separating shear layers become more and more aligned with the free stream, until eventually the transition to turbulence point reaches the separation point at the critical Reynolds number.

It is well known that the effect of free stream turbulence can be seen as an effective increase in Reynolds number, resulting in the critical transition and the decrease in axial correlation length to occur at lower Reynolds numbers (Cheung, 1983). Unfortunately, in order to obtain data at these Reynolds numbers the diameter of the cylinder needs to be large because of velocity limits of wind/water tunnel facilities. This causes the ratio of turbulence integral scale to cylinder diameter to reduce below unity, typically 0.5D. Experimental data obtained in these conditions have shown little effect of turbulence scale on the axial correlation length, results typically giving values of 1 diameter in the critical/supercritical regimes (Bruun and Davies, 1975; Blackburn, 1992). Due to these results it is currently understood that free stream turbulence affects the Reynolds number when transition is initiated and the magnitude of the pressure fluctuations around the cylinder. Results from experiments that have used turbulence of longitudinal integral scale ($L_x/D$) larger than the diameter of the cylinder are reported, Surry (1972) and Mulcahy (1984), but either have not investigated Reynolds numbers in the critical regime or have not measured the axial correlation length.

In this paper we present results from experiments in which the turbulence integral scale was varied from 0.7D to 2D with turbulence intensities between 2 and 12 %, for a Reynolds number range of $7 \times 10^4$ to $3.3 \times 10^5$. The results in low and high turbulence flow with an $L_x/D$ smaller than the cylinder diameter are presented to show agreement with published data. These results are then extended with new data from experiments with $L_x/D$ larger than the cylinder diameter.

## 2. EXPERIMENTAL METHOD

### 2.1 CYLINDER MODEL

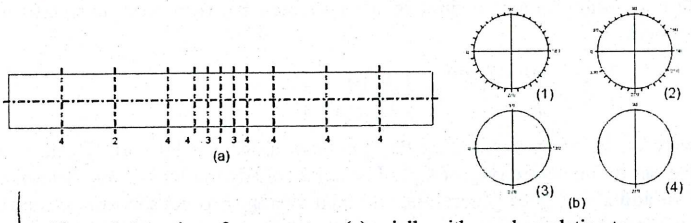


Figure 1: Location of pressure taps (a) axially with number relating to (b) circumferential position

The circular cylinder model was constructed from diameter 100mm aluminium tube. This cylinder was pressure tapped as shown in Figure 1 with a complete ring of taps at 10 degree intervals in the centre and taps along the 90 and 270 degree generators (0 degrees being the front stagnation line) at ratios of the cylinder diameter. Each tapping consisted of a 1mmID x 20mm stainless steel tube inserted in the cylinder wall with a 1500mm long P.V.C tube connecting it to a pressure transducer. The P.V.C tubing was closed with no restrictors or leaks to reduce the resonant response of the tubing. The cylinder used was classified a nominally smooth with a roughness ratio ($k/D$) of $0.02 \times 10^{-3}$. This was achieved by sanding the cylinder surface with fine emery paper to remove any major surface imperfections.

## 2.2 WIND TUNNELS

The experiments were performed in the 450kW and 1MW wind tunnels at Monash University. The use of these two tunnels allowed Reynolds numbers from 7 x $10^4$ to 3.3 x $10^5$ to be obtained with different turbulence intensities and integral scales. The cylinder was installed in the 2x1m section of the 450kW tunnel horizontally at mid height between end plates, resulting in an aspect ratio of 9.0:1 and a blockage of 5 %. The cylinder was clamped in place when aligned to the flow and can be classified as a stationary cylinder. In the 5x4m working section of the 1MW tunnel a platform was used to mount the cylinder vertically between end plates so the aspect ratio remained identical to the 450kW tunnel. Blockage in this tunnel was reduced to 2.5%. The cylinder was mounted vertically for easy connection of the pressure taps to the pressure transducers.

Alignment of the cylinder with the onset flow was achieved by rotating the cylinder until the stagnation pressure at the zero degree pressure tap was maximised and the pressure taps on either side (10 and 350 degrees) had similar mean pressures.

## 2.3 TURBULENCE GENERATION

Homogeneous free stream turbulence of different intensity and scale was generated in the 450kW tunnel using grids placed at four or five positions upstream of the cylinder. The turbulence characteristics at each position were measured using an end flow crossed hot wire anemometer connected to a TSI constant temperature anemometer bridge. The three turbulence components were obtained by rotating the cross wire 90 degrees, first measuring the $u,w$ and then the $u,v$ components.

The integral length scales were determined by fitting the Von Kärman turbulence spectra to the spectrum of turbulence measured in the wind tunnel. Tables 1 and 2 present the turbulence intensities and integral length scales for the three $(u,v,w)$ components of turbulence with '$x$' being the distance from the cylinder centreline to the centreline of the turbulence grid.

**Table 1: Grid 1 turbulence intensities and integral length scales in 450kW Wind Tunnel**

| Position | $I_u$ (%) | $I_v$ (%) | $I_w$ (%) | $L_{ux}/D$ | $L_{uy}/D$ | $L_{uz}/D$ |
|---|---|---|---|---|---|---|
| Bare Tunnel | 0.6 | 0.6 | 0.6 | | | |
| 1. x = 4.6m | 12 | 12 | 12 | 1.4 | 0.8 | 0.8 |
| 2. x = 5.6m | 10 | 10 | 10 | 1.4 | 0.9 | 0.9 |
| 3. x = 7.2m | 7 | 7 | 7 | 1.4 | 1.2 | 1.2 |
| 4. x = 9.6m | 5 | 5 | 5 | 1.4 | 1.4 | 1.4 |

**Table 2: Grid 2 turbulence intensities and integral length scales in 450kW Wind Tunnel**

| Position | $I_u$ (%) | $I_v$ (%) | $I_w$ (%) | $L_{ux}/D$ | $L_{uy}/D$ | $L_{uz}/D$ |
|---|---|---|---|---|---|---|
| 1. x = 3.55m | 7 | 7 | 7 | 0.7 | 0.7 | 0.7 |
| 2. x = 4.6m | 5.3 | 5.3 | 5.3 | 0.7 | 0.7 | 0.7 |
| 3. x = 5.6m | 4 | 4 | 4 | 0.7 | 0.7 | 0.7 |
| 4. x = 7.2m | 3 | 3 | 3 | 0.7 | 0.7 | 0.7 |
| 5. x = 9.6m | 2 | 2 | 2 | 0.7 | 0.7 | 0.7 |

The turbulence conditions in the 1MW wind tunnel with no grid was $I_u$=3.5%, $I_v$=3.5% , $I_w$=3.5%, $L_{ux}/D$=2, $L_{uy}/D$=1.2, and $L_{uz}/D$=2.

## 2.4 DATA ACQUISITION AND PROCESSING

The instantaneous pressures from the 88 pressure taps on the cylinder were sampled using an electronic Scanivalve system at a frequency of 1000hz for 35 seconds.

The initial processing of the pressure data involved correcting the data for the resonant response of the P.V.C tubing and the small time lag caused by the multiplexers in the Scanivalve. The correction of the resonant response was done using the technique presented by Irwin *et al* (1979) in the frequency domain. The resonant response and phase lag of the 1500mm P.V.C. tubing at frequencies up to 500hz had been previously measured. Convolution of inverse of this response with the Fourier transformed pressure data corrected the data for the resonant and phase lag effects. In the frequency convolving the data with an inverted phase shift and an amplitude response of one corrected for domain the time lag imposed by the multiplexer. The data was then inverse Fourier Transformed to give the corrected pressure signal for each tapping.

The axial correlation length is determined by integrating the correlation coefficients as a function of the axial separation from a reference point, as given in Equation (1). Ideally the limits of integration are zero and infinity but due to the constraints of experiments the correlation length integral is approximated between zero and point where the correlation coefficient curve first becomes negative.

$$\lambda_z = \int_0^{\rho_{xz}\left(\frac{x}{D}\right)=0} \rho_{xz}\left(\frac{x}{D}\right) d\left(\frac{x}{D}\right) \qquad (1)$$

The correlation coefficients were obtained by correlating the pressures along the 90 and 270 degree generators with the pressure at the 90 or 270 degree tap in the centre ring of taps. The axial correlation length was determined four times, to the left and right of centre on the 90 and 270 degree generators, and then averaged to get the axial correlation length quoted in this paper. This approach was taken because the vortex shedding in the critical and supercritical regimes is three dimensional along the cylinder axis. Therefore, the centre reference point may not be exactly in the centre of a vortex cell and shorter or longer correlation lengths may be measured to the left and right of the centreline.

# 3. RESULTS

The axial correlation length measured on the smooth cylinder in low turbulence flow is presented in Figure 2 with published data from three authors are included for comparison. This figure illustrates how the axial correlation length decreases dramatically when the cylinder undergoes critical transition. In the high subcritical regime (Re< 2x$10^5$) the axial correlation length is between 3.5 to 4 diameters and then suddenly drops to approximately 1 diameter in the supercritical regime. Excluding Batham's (1973) data all the other data undergoes transition at a Reynolds number, although Bruun and Davies

(1975) have only managed to capture the initial part of the transition process. Agreement between Blackburn and Melbourne (1993) and current data is good, as both experiments were performed in the same wind tunnel.

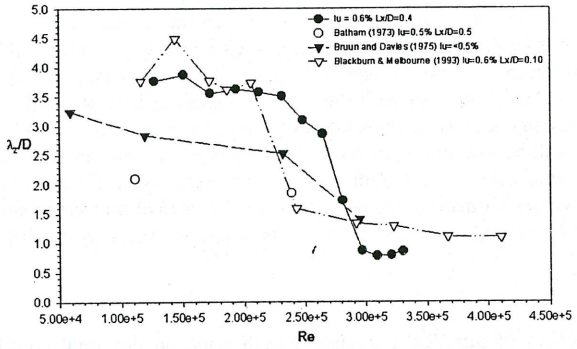


**Figure 2: Axial Correlation Length for a Smooth Cylinder in low turbulence flow as a function of Reynolds Number**

Figure 3 (a) and (b) present the axial correlation length measured for the $L_x/D$ ratios used in these experiments. Figure 3(a) is the data obtained for the flow conditions where the $L_x/D$ was less than unity. The effect of the turbulence is to promote earlier critical transition on the cylinder, as shown by a measured axial correlation length of one for almost all cases. This agrees well with the experimental data from Blackburn and Melbourne (1993) for their lower turbulence intensities. However, at their highest intensity there is a noticeable increase in the axial correlation length indicating an increase in vortex shedding organisation. Batham's (1973) indicates a considerably shorter axial correlation length in turbulent flow, approximately 0.5D. One point in the current data does stand out, the lowest Reynolds number at an intensity of 2% where an axial correlation length of three diameters was recorded. Comparison with correlation lengths in Figure 2 indicates at this turbulence intensity critical transition is occurring between the two lowest Reynolds numbers.

Figure 3(b) presents the five turbulence configurations where the $L_x/D$ ratio was greater than unity. The effect of the larger integral turbulence on the axial correlation length is significant when figures (a) and (b) are compared. The axial correlation length increases with turbulence intensity reaching values near three diameters at the highest turbulence intensity. This correlation length is similar to those measured in the high subcritical regime for the smooth cylinder in low turbulence flow (Figure 2). Unfortunately, the velocity range available in the 450kW wind tunnel with the grids installed limited the lowest Reynolds number attainable; hence we were not able to take measurements in these turbulence configurations that included the critical transition Reynolds number.

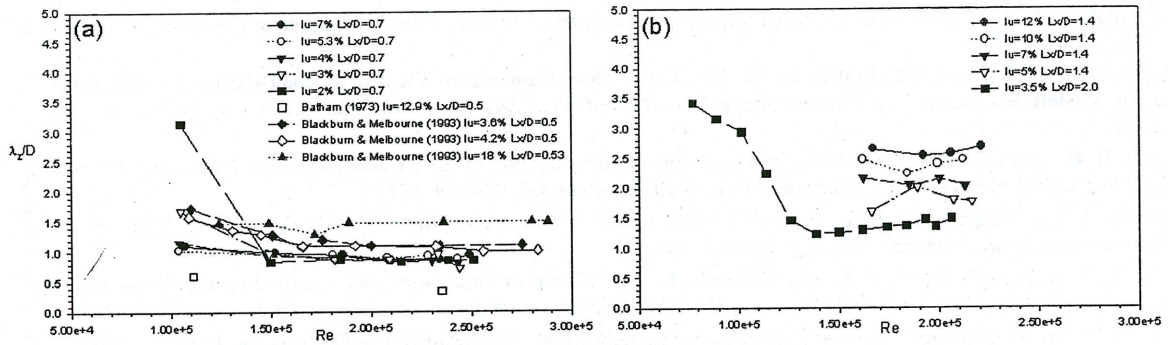


**Figure 3: Axial Correlation Length for a Smooth Cylinder in turbulent flow with (a) $L_{ux}/D < 1$, and (b) $L_{ux}/D > 1$, as a function of Reynolds number**

## 4. DISCUSSION

The axial correlation length measured on the smooth cylinder in low turbulence flow showed good agreement with previously published data. The axial correlation length decreased from 3-4 diameters to one diameter during critical transition, which is the accepted value for smooth circular cylinders in low turbulence flow in the critical regime (King, 1977).

As described by Batham (1973), Cheung (1983) and Blackburn and Melbourne (1993) the introduction of free stream turbulence results in an effective increase in the Reynolds number. This is apparent in the current set of results for turbulence with a longitudinal $L_x/D$ less than unity, with an axial correlation length of 1 diameter measured in the turbulent flow. These values are consistent with those obtained by researchers who have tested smooth circular cylinders in turbulent flow and was expected because the majority of the published axial correlation length data for a smooth cylinder in turbulent flow has been taken with turbulence with this $L_x/D$. This scale ratio is the result of the unfortunate compromise between obtaining high Reynolds numbers of the critical and supercritical regimes vs. maintaining a high integral scale to diameter ratio. The effect of small-scale turbulence was to promote earlier critical transition, which has been described by Batham (1973) as an effective increase in Reynolds number. Turbulence of this scale may be successful at promoting this transition because it can interact with the separation shear layers causing the point of turbulence transition to occur closer or at the point of separation.

The axial correlation lengths measured in the turbulent flow with a longitudinal $L_x/D$ greater than unity showed a significant increase in the vortex shedding organisation that increased with turbulence intensity, peaking at values of three diameters at the highest intensity. Blackburn and Melbourne (1993) postulated that this might occur in turbulent flows with large integral scales. Their results, which are replotted in Figure 3(a), showed that at high turbulence intensity, although the integral scale was 0.5D, the axial correlation length is increased. Further investigation is required to determine the mechanisms that cause this increased vortex shedding organisation. Current thought is the larger $L_x/D$ vortices, particularly the traverse component (perpendicular to the flow and cylinder axis), interact with the vortices shedding from the cylinder prompting them to shed over larger span of the cylinder at the same instant. Investigation of $L_x/D$ effects on a flat plate by Li and Melbourne (1999) showed that a quasi steady situation will be eventually reached where further increases in $L_x/D$ are seen as a slowly varying mean flow and have no effect on the axial correlation length. This is expected to occur for a circular cylinder and may have a relationship with the length of the vortex formation region, which in the critical and early supercritical regimes is 2.7D (Roshko, 1993). The $L_x/D$ required for this quasi-steady situation is unknown and may be difficult to generate in a wind tunnel due to facility limitations.

## 5. CONCLUSIONS

This research has investigated the effect of turbulence integral length scale on the axial correlation length on a smooth cylinder in the critical and supercritical regimes. Comparison with published axial correlation lengths for smooth cylinders in low turbulence flow has found good agreement.

Axial correlation lengths measured for the smooth cylinder in turbulence flow with the $L_x/D$ less than unity were found to agree with current expected values of one diameter. The turbulence caused an effective increase in the Reynolds number, with critical transition occurring at considerably lower Reynolds numbers than the low turbulence case. Turbulence of this integral scale is able to interact with the separating shear layers promoting the turbulent transition and reducing the axial uniformity of the vortex shedding, hence the decrease in axial correlation length.

The axial correlation length was found to increase with turbulence intensity for $L_x/D$ greater than unity. Peak values of approximately three diameters were measured on the cylinder for turbulence intensities of 12%, which are similar to those measured in the high subcritical regime. Further investigation is required to determine the mechanism that causes this increase in vortex shedding organisation. Current thought is the larger scale turbulent vortices, especially the traverse component, are able to interact with the shedding vortex and cause the vortex to shed along the axis of the cylinder at the same instant. Based on results for a flat plate, it is expected that the effect of the turbulence integral scale will eventually reach a quasi-steady situation and this may be related to the formation length of the vortices shedding from the cylinder.

## 6. REFERENCES

BATHAM, J. P., "Pressure Distributions on Circular Cylinders at Critical Reynolds numbers", *Journal of Fluid Mechanics*, **57** (2), 209-228, 1973.

BLACKBURN, H. M., "Lift on an Oscillating Cylinder in Smooth and Turbulent Flows", *Mechanical Engineering*, Monash University, Clayton, 1992.

BLACKBURN, H. M., and MELBOURNE, W. H., "Cross Flow Response of Slender Circular-Cylindrical Structures: Prediction Models and Recent Experimental Results", *Journal of Wind Engeering and Industrial Aerodynamics*, **49**, 167-176, 1993.

BRUUN, H. H., and DAVIES, P. O. A. L., "An Experimental Investigation of the Unsteady Pressure Forces on a Circular Cylinder in a Turbulent Cross Flow", *Journal of Sound and Vibration*, **40**, 535-539, 1975.

CHEUNG, C. K., "Effect of Turbulence on the Aerodynamics and Response of a Circular Structure in Wind Flow", *Mechanical Engineering*, Monash University, Clayton, 1983.

IRWIN, H. P. A. H., COOPER, K. R., and GIRARD, R., "Correction of Distortion Effects caused by tubing systems in measurements of Fluctuating Pressures", *Journal of Wind Engineering and Industrial Aerodynamics*, **5**, 93-107, 1979.

KING, R., "A Review of Vortex Shedding Research and its Application", *Journal of Ocean Engineering*, **4**, 141-172, 1977.

LI, Q. S., and MELBOURNE, W. H., "The effect of large scale turbulence on pressure fluctuations in separated and reattaching flows", *Journal of Wind Engineering and Inductrial Aerodynamics*, **83**, 159-169, 1999.

MULCAHY, T. M., "Fluid Forces on a Rigid Cylinder in Turbulent Cross Flow", *ASME Symposium on Flow Induced Vibration*, M. P. e. a. Paidoussis, ed., 1984.

ROSHKO, A., "Experiments on the flow past a circular cylinder at very high Reynolds number", *Journal of Fluid Mechanics*, **10**, 345-356, 1961.

ROSHKO, A., "Free Shear Layer, Base Pressure and Bluff Body Drag", *Symposium on Developments in Fluid Dynamics and Aerospace Engineering*, Bangalore, India, 1993.

SURRY, D., "Some Effects of intense turbulence on the aerodynamics of a circular cylinder at subcritical Reynolds number", *Journal of Fluid Mechanics*, **52** (3), 543-563, 1972.

ZDRAVKOVICH, M. M., "Flow Around Circular Cylinder" Oxford University Press, Oxford, 1997.

*Melbourne Graduate Fluids Conference, 2001*
*Monash University, Melbourne, Australia*

# A 2D NUMERICAL STUDY OF THE FLOW AROUND BLUFF RINGS

**G.J. SHEARD, M.C. THOMPSON and K. HOURIGAN**

Department of Mechanical Engineering
Monash University, Clayton, Victoria, AUSTRALIA

## ABSTRACT

A numerical study of the flow around bluff rings at low Reynolds number is presented. A Spectral Element method is used to solve the unsteady axisymmetric Navier-Stokes equations governing the fluid flow. Strouhal-Reynolds number profiles are provided for a range of ring aspect ratios, as well as critical Reynolds numbers for the onset of flow separation and periodic flow. These results show a decrease in shedding frequency and an increase in the critical Reynolds numbers for separation and unsteady flow with decreasing ring aspect ratio.

## 1. INTRODUCTION

Bluff body flows have been of practical interest to mankind for centuries. Be it the mechanics of ships or aircraft, the trajectory of an arrow or cannonball, the flow of a fluid (air, water, or another medium) around a body and the interaction that takes place, all of these are of immense interest.

Research has shown for various bluff bodies that a variety of flow states to exist over a range of Reynolds number. Very low Reynolds number flows are laminar in nature, and increasing Reynolds number leads to separation from the body and wake recirculation. The wake becomes progressively unsteady and three-dimensional with further Reynolds number increases, before becoming turbulent. Flow properties relating to drag, lift and Strouhal number vary greatly depending on the form of the wake present in the flow.

Bluff rings have been afforded little attention from researchers despite exhibiting similarities to simple geometries such as straight cylinders or spheres when the ring cross-section is extremely thin or thick respectively. Leweke & Provansal (1994) studied large aspect ratio rings due to their similarity to straight cylinders without the end effects normally encountered in experimental work. This investigation focuses on the low Reynolds number, 2D flow regime. A Galerkin Spectral-Element method is used to solve the unsteady 2D axisymmetric Navier-Stokes equations for a range of bluff ring models, with the intention of developing Strouhal profiles for the system where unsteady flow is observed, as well as determining the critical Reynolds numbers for the onset of separation of flow around the ring, and unsteadiness in the wake.

Little work has been carried out on the bluff ring geometry to date. Roshko (1953) carried out early work, noting a reduction in Strouhal number by a few percent for ring vortex shedding when compared to the straight cylinder, and pointed out some major changes experienced at low aspect ratios. Probably the most significant body of work has been contributed by Leweke & Provansal (1994). They carried out detailed experiments on bluff rings of large aspect ratio in an attempt to model cylinders without end effects. The effect of ring curvature was linearised and incorporated into an equation that provides the laminar, Strouhal-Reynolds number relationship for large-$Ar$ bluff rings as a function of $Re$, curvature $K$ and shedding angle θ:

$$St(\mathrm{Re}, K, \theta) = \{S_0(\mathrm{Re}, K = 0) - a(\mathrm{Re} - \mathrm{Re}_1)K\}\cos\theta \qquad (1)$$

$$where\ S_0(\mathrm{Re}, K = 0) = \frac{-3.810}{\mathrm{Re}} + 0.1904 + 1.220\times10^{-4}\,\mathrm{Re} \qquad (2)$$

This investigation focuses on the axisymmetric flow regime experienced at low Reynolds number. From understanding of straight cylinder and sphere flows, 3D flow appears between $178 < Re < 211$. This investigation covers the Reynolds number range up to $Re = 250$ to cover the likely 2D regime.

## 2. NUMERICAL METHOD

To model the bluff ring flow a Galerkin Spectral-Element scheme was used. This technique has been applied successfully to two- and three-dimensional bluff body flow problems such as the circular cylinder (Thompson et al, 1996). Briefly, the method uses a three-step time splitting scheme for temporal discretisation of the governing Navier-Stokes equations. Spatial discretisation is performed using a Galerkin Finite Element method with high-order Lagrangian interpolants applied within each element. A visual representation of the bluff ring geometry is given in **Figure 1**.

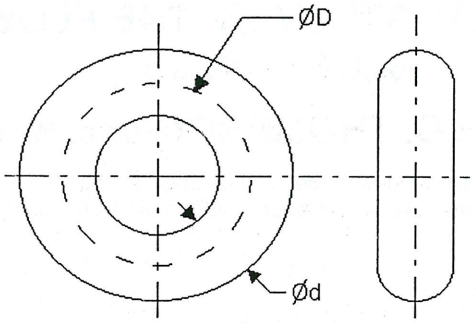


**Figure 1** : Bluff ring geometry and associated dimensions.

**Figure 1** shows that the geometry is essentially a torus, or a ring around the axis with a circular cross-section. The direction of fluid flow is in the axial direction, normal to the plane of the ring. The fluid flow interacts with the geometry by flowing around the circular ring cross-section, so a dimensionless parameter describing the fluid motion as a Reynolds number can be given based on the fluid velocity, $U$, the length scale of the ring cross-section diameter, $d$, and the fluid viscosity, $\nu$:

$$Re = \frac{Ud}{\nu} \tag{3}$$

For consistency with previous studies, the geometry is represented by an aspect ratio parameter $Ar$. This is simply a ratio of the circumference of the ring around the axis (the major axis dimension), and the ring cross-section diameter (the minor axis dimension):

$$Ar = \frac{\pi D}{d} \tag{5}$$

## 3. BLUFF RING GRID RESOLUTION STUDY

A thorough grid resolution study was conducted on a family of similar grids – small $Ar$ grids were a subset of larger $Ar$ grids. A similar grid resolution study to that performed by Barkley & Henderson (1996) was carried out. Mesh elements were concentrated around the ring cross-section, and the downstream region, where fine resolution was required. Uniform meshes with the same concentration near the cross-section of the ring resulted in far less efficient simulations, however the discrepancy between the results of the two grids was in the order of 0.1%. Thus the grids with the tetrahedral expansion were selected for the study:

Initial studies were performed on a grid of moderate domain size and a low number of nodes per element, for the $Ar = 20\pi$ case. This was chosen because vortex shedding was expected at the chosen $Re$ for simulation of 200, similar to the circular cylinder.

A suitable time step was found by running a simulation on the $Ar = 20\pi$ test grid with 25 nodes per element. Due to the nature of the spectral element model chosen, good temporal accuracy is achieved with the time step chosen close to the Courant time step. Convergent simulations were obtained with a time step of 0.005 for the range of Reynolds numbers being investigated in this study.

The number of nodes per element ($N$) chosen was found by using the $Ar = 20\pi$ grid above with the 0.005 time step, and varying the number of nodes per element. **Table 1** shows adequate performance of the $N = 49$ grid:

| Nodes per element: | Strouhal number: | Percentage difference: |
|---|---|---|
| 25 | 0.17813 | 5.8 |
| 49 | 0.17911 | 0.033 |
| 81 | 0.17917 | 0.0 |

**Table 1** : Strouhal numbers from nodes per element study.

With a suitable time step and number of nodes per element determined, an adequate domain size was found in the radial direction to limit blockage effects caused by the outer boundary.

Previous studies on the wakes of spheres (Tomboulides et al, 1993), and cylinders (Barkley & Henderson, 1996) have found using similar numerical schemes that the transverse domain must be greater than about 12 length units from the object in 2D (ie. about 360d for the Ar = 20π ring), however variations in the radial direction for an axisymmetric model were found to vary with the square of the radius, thus requiring a smaller radial domain size based on the outer diameter of the model. **Figure 2** shows the Strouhal number found for the domain sizes tested for the $Ar = 20\pi$ case. The difference between the radius = 150d and 250d cases was a mere 0.0514%:

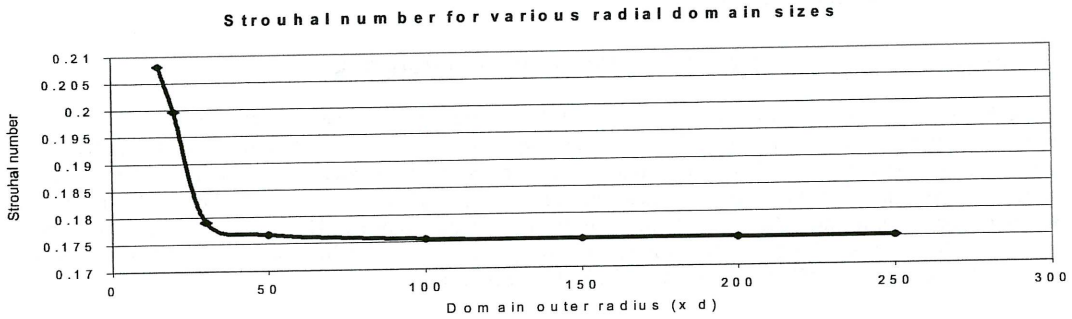


**Figure 2** : Graph of Strouhal number for various radial domain sizes.

Thus the domain size of 150d units in radius was used for all aspect ratio models, and the similar mesh created for a comparative study of the straight circular cylinder.

To avoid outlet effects interfering with the wake of the ring cross-section, a downstream domain length of 25d was used, consistent with previous numerical studies such as Barkley & Henderson (1996).

## 4. BLUFF RING LAMINAR FLOW REGIME

The Strouhal profile for each ring in the laminar flow regime is shown in **Figure 3**. Note how the smaller Aspect ratio rings shed at lower frequency and the critical Reynolds number for the onset of shedding increases:

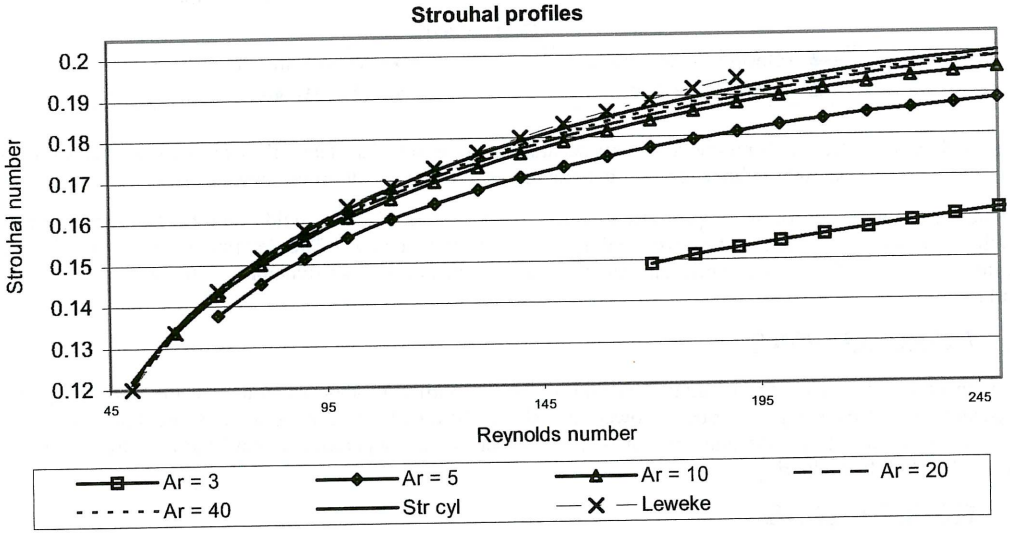


**Figure 3** : Laminar Strouhal number profiles for various Aspect ratio rings, the straight circular cylinder, and results provided in the literature.

**Figure 4** shows vorticity contours of the $Ar = 5\pi$ ring at $Re = 150$. Simulations such as this were conducted to ascertain the Strouhal-Reynolds profiles (see **Figure 3**) for the various ring sizes investigated. Note the pairing of shed vortices downstream of the ring, and the divergence of the vortices from the axis:

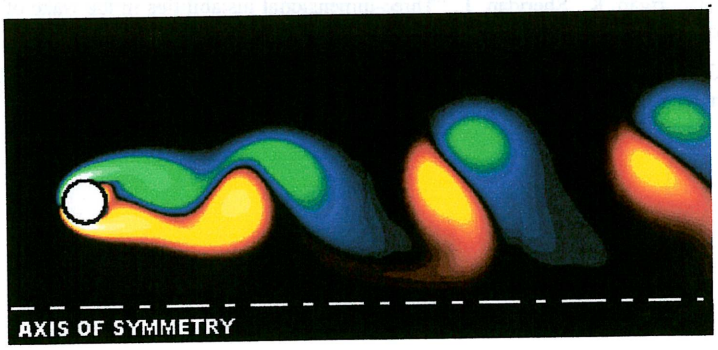


**Figure 4** : Vorticity contours for flow around a bluff ring with Ar = $5\pi$ at Re = 150.

## 5. BLUFF RING CRITICAL REYNOLDS NUMBERS

**Figure 5** illustrates a trend apparent with decreasing Aspect ratio and increasing curvature ($K$) for the critical Reynolds numbers for the separation of flow over the body and the onset of shedding to occur at a greater value. Curvature is related to Aspect ratio by the relation $K = 2\pi/Ar$. As expected, increasing Aspect ratio (decreasing $K$) represents a trend towards the limit of the geometry as a straight cylinder (left axis on chart), and the onset of shedding asymptotes towards the onset of shedding for the straight cylinder. The critical Reynolds numbers for the onset of Mode A and Mode B 3D shedding are also given for the straight cylinder case. Future work will complete the trend of such 3D instabilities over the bluff ring parameter space.

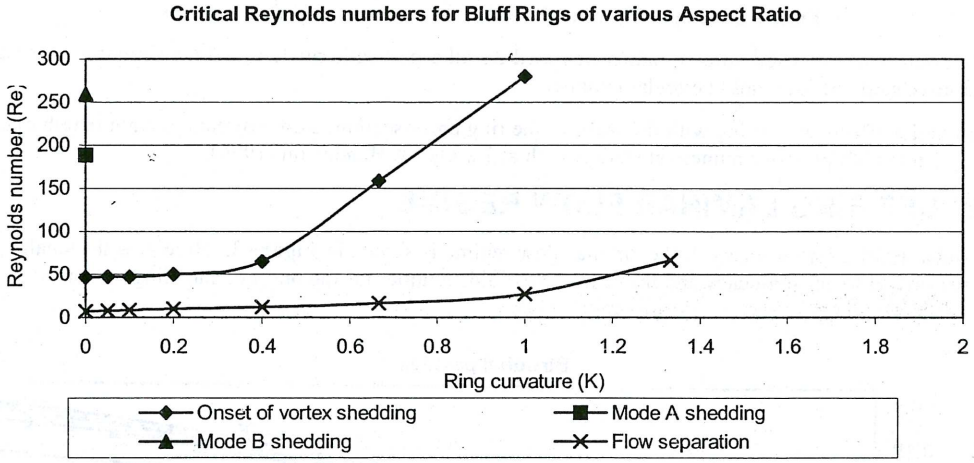


**Figure 5** : Critical Reynolds numbers for flow separation and onset of unsteady flow for increasing ring curvature (straight cylinder on left, tending towards a sphere with increasing curvature.

3D flow is expected to occur in preference to the axisymmetric 2D flow fields investigated here at Reynolds numbers of order Re = 200 and above, leading to fully turbulent flow. The determination of both the critical Reynolds numbers for such a transition, and the resulting physical wake dynamics is the topic of forthcoming work.

## 6. CONCLUSIONS

As with previous studies, the laminar flow regime for the bluff ring appears similar to the straight cylinder at sufficient $Ar$. Decreasing $Ar$ tends to lower the relative Strouhal number for a given Reynolds number, and increase the critical Reynolds numbers for both the onset of flow separation around the ring cross-section, and vortex shedding from the ring.

## 7. REFERENCES

Barkley, D., Henderson, R. D., "Three-dimensional Floquet stability analysis of the wave of a circular cylinder", *J. Fluid Mech.*, **322**, 215-241, 1996.

Leweke, T., Provansal, M., "The flow behind rings: bluff body wakes without end effects", *J. Fluid Mech.*, **288**, 265-310, 1995.

Roshko, A., "On the development of turbulent wakes from vortex streets", *NACA Tech. Note 2913*, 1953.

Thompson, M.C., Hourigan, K., Sheridan, J., "Three-dimensional instabilities in the wake of a circular cylinder", *Exp. Therm. Fluid Sci.*, **12**, 190-196, 1996.

Tomboulides, A.G., Orszag, S.A., Karniadakis, G.E., "Direct and large-eddy simulation of the flow past a sphere", *2nd ICTME*, Florence, 1993.

*Melbourne Graduate Fluids Conference, 2001*
*Monash University, Melbourne, Australia*

# VORTEX FORCES ON AN OSCILLATING CYLINDER

**J. CARBERRY and J. SHERIDAN**
Department of Mechanical Engineering
Monash University, Clayton, Victoria, AUSTRALIA

## ABSTRACT

The relationship between the vortex structures in the near wake and the forces on a moving body is investigated for a cylinder undergoing forced oscillations transverse to a free-stream. Using the formulation of Wu (1981), we calculate the vortex lift force by subtracting the inertia force from the total lift force. By considering the phase of vortex shedding and the distribution of vorticity in the near wake, we find that the vortex lift force, not the total lift force, represents the force due to the vorticity field. The phase of vortex shedding does not vary with the amplitude of oscillation, and while the phase of the total lift force varies with A/D, the phase of the vortex lift force collapses towards two constant values representing two distinctly different wake states.

## 1. INTRODUCTION

Flow past a stationary cylinder results in large scale vortex shedding at a characteristic frequency $f_o$. When the cylinder oscillates at frequencies close to $f_o$, the perturbation of the natural instability can generate significant changes in the structure of the near wake and the forces on the cylinder. The interaction between an oscillating body and the flow field, in particular the case where the cylinder is constrained to oscillate transverse to the free-stream, has been studied extensively. The cylinders motion can be mechanically driven (forced), or the result of vortex induced forces (free).

The study of a cylinder undergoing forced oscillations by Bishop & Hassan (1963), showed that as the frequency of oscillation $f_e$ increases through $f_e/f_o = 1$, there was an abrupt jump in the phase and amplitude of the lift force on the cylinder. The jump in the lift force appears to be a universal feature of this class of flows and has subsequently been observed over a wide range of oscillation amplitudes and Reynolds numbers: Mercier (1973), Staubli (1983), Gopalkrishnan (1993) and Sarpkaya (1995). Abrupt changes in the structure of the near wake and the mode of vortex shedding are also observed around $f_e/f_o = 1$, Williamson & Roshko (1988), Ongoren & Rockwell (1988) and Gu *et al* (1994). Subsequently, it was shown by Carberry *et al* (2001), that the jump in the amplitude and phase of the lift force corresponds to a change in the mode and phase of vortex shedding. The exact value of $f_e/f_o$ at which this transition occurs appears to vary with Re and turbulence levels, however the mechanisms which causes these variations are not well understood. The wake states either side of the transition are referred to as the low and high frequency states. The structure of the near wake and the lift force characteristics of the low and high frequency wake states were described in detail by Carberry *et al* (2001). The general form of these wake states is strikingly similar to those observed for a freely oscillating, elastically mounted cylinder, Govardhan & Williamson (2000).

If the relationship between the flow field and the force on a body is known, then we can identify the physical changes in the wake which correspond to changes in the force on the body. The forces on a moving body can be expressed in terms of the fluid inertia and the rate of change of the vortex moment, Wu (1981):

$$\vec{F}_{total} = -\rho \frac{d}{dt} \int_{Vc} \vec{r} \times \vec{\omega} \, dV + \rho \frac{d}{dt} \int_{Vb} \vec{u} \, dV \qquad (1)$$
$$= \vec{F}_{vortex} + \vec{F}_{fi}$$

where $V_c$ is a distant external boundary containing all the shed vorticity and $V_b$ is the volume bounding the solid body, in our case the cylinder.

The first term in equation (1) is the force due to the vorticity field, $F_{vortex}$, whilst the second term is the inertia force of the fluid displaced by the acceleration of the body. For a cylinder oscillating transverse to the free-stream, $F_{fi}$ is parallel to the lift force and the fluid inertia lift force, $F_{L\,fi}$ is equal to $F_{fi}$. While equation (1) is a useful tool for interpreting the flow field, it has proved difficult to accurately calculate the force on a body using the vortex field within a finite two-dimensional boundary which does not contain all the shed vorticity. The idea of identifying the force component due to vorticity was also examined by Lighthill (1986). Lighthill considered two force components: a) a force due to the potential flow, which varies linearly with the velocity field and includes the potential added mass force, and b) a non-linear, vortex force. However, his vortex force represents only the force on the body due to the additional vorticity: the vorticity field minus the distribution required to generate the potential flow slip boundary condition at the body. Equation (1) is derived without simplifying assumptions and we interpret $F_{fluid}$ without needing to assume potential flow. By

coincidence, for a circular cylinder $F_{fi}$ is equal to the potential flow added mass force for a fully submerged cylinder.

Despite the insights of Wu (1981) and Lighthill (1986) it is common to consider only the total lift on an oscillating body without considering the contributions of the vortex and fluid inertia components. In these cases the total lift force is simply referred to as the lift force. Govardhan & Williamson (2000) demonstrated that the changes in the total lift force may not fully represent the changes in the vorticity field. They calculated the vortex lift force by subtracting the "potential added mass force", which for a circular cylinder is equivalent to $F_{fi}$, from the total lift force. For an elastically mounted cylinder, they found that the jump in the phase of the vortex lift force did not occur at the same reduced velocity as the jump in the phase of the total lift force. The jump in the phase of the vortex lift force always corresponded to a change in the wake mode, from 2P to 2S. However, the jump in the phase of the total lift force did not necessarily correspond to a significant change in the mode of vortex shedding. In this paper we use the general equation for the vortex force (1) to describe the vortex force on an oscillating cylinder, we then relate the vortex force to the vortex structures in the near wake.

## 2. EXPERIMENTAL METHOD

The cylinder was forced to oscillate transversely to the free-stream such that its vertical motion was given by: $y(t) = A \sin(2\pi f_e t)$. Three different amplitudes of oscillation, A/D = 0.4, 0.5 & 0.6 were used, while the frequency varied from $0.74 < f_e/f_o < 1.27$. The free-stream velocity was constant at 0.090 $ms^{-1}$ and the Reynolds number, $Re = U_\infty D/\nu$, was 2300. The cylinder, 25.4 mm in diameter, with an aspect ratio of 12.5, was fitted with end plates which oscillated with the cylinder. The velocity field of the near wake of the cylinder was measured using a laser scanning version of high-image density PIV. The images were recorded on high resolution 35 mm film and digitised at 106 pix/mm. The resulting velocity fields contained approximately 3500 velocity vectors. The phase averaged vorticity fields reported here were calculated from 9 instantaneous velocity fields. The time varying lift force on the cylinder was measured by strain gauges mounted on a support sting. The body inertia force due to the oscillation of the mass of the cylinder and the support sting, was subtracted from the lift force.

## 3. RESULTS AND DISCUSSION

### 3.1 TOTAL LIFT FORCE

For the range of oscillation frequencies and amplitudes studied the wake is "locked on" to the cylinder's motion and the sinusoidal lift force has a dominant frequency of $f_e$. Thus, the time varying total lift coefficient can be approximated by a sinusoidal function:

$$C_L(t) \approx C_L \sin(2\pi f_e t + \phi_{lift}) \qquad (2)$$

where $C_L$ is the amplitude of the total lift force coefficient and $\phi_{lift}$ is the phase of the total lift with respect to the cylinders displacement y(t). To provide continuity with the nomenclature used in previous work the symbols $C_L$ and $\phi_{lift}$ are used to describe the amplitude and phase of the total lift force.

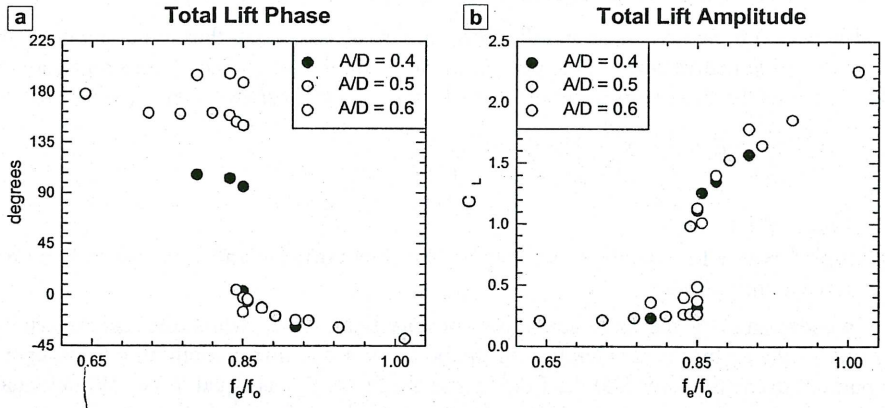


**Figure 1 Variation of $\phi_{lift}$ and $C_L$ with $f_e/f_o$, for A/D = 0.4, 0.5 and 0.6.**

The variation of $C_L$ and $\phi_{lift}$ with $f_e/f_o$, for three different amplitudes of oscillation is shown in Figure 1. For all values of A/D, at $f_e/f_o \approx 0.85$ there is an abrupt change in the amplitude and phase of the total lift coefficient, which has been shown, Carberry *et al* (2001) to correspond to a transition between two distinctly different wake states. Figure 1a shows that for the low frequency wake state ($f_e/f_o < 0.85$), there is an increase in $\phi_{lift}$ as the amplitude of oscillation increases. The change in $\phi_{lift}$ for the low frequency wake states as A/D increases from 0.4 to 0.6 is approximately 90°. However, for the high frequency wake state $\phi_{lift}$ appears to be independent of the changes in A/D. Similarly, in Figure 1b $C_L$ does not vary significantly as

A/D increases from 0.4 to 0.6. It is difficult to compare the change in $\phi_{lift}$ at transition with the change in the phase of vortex shedding, as transition also corresponds to a change in the mode of vortex shedding. However, the variation of $\phi_{lift}$ with A/D for the low frequency wake mode, allows us to compare changes in $\phi_{lift}$ with the phase of vortex shedding for a given mode of vortex shedding.

Figure 2 shows the time evolution of the low frequency wake state for A/D = 0.4 and 0.6. Despite the change in the amplitude of oscillation, the mode and timing of vortex shedding are very similar. However, it is clear that as is A/D increased from 0.4 to 0.6, the vertical movement of the wake increases, and there is a change in the distribution of vorticity in the near wake. The vorticity fields in Figure 2 correspond to the two data points at $f_e/f_o$ = 0.823 in Figure 1. Despite the similarity in the phase of vortex shedding in Figure 2, the values of $\phi_{lift}$ are very different, 103° and 196° for A/D = 0.4 and 0.6 respectively Thus, it is evident that the phase of the total lift force (total) does not represent the phase of vortex shedding.

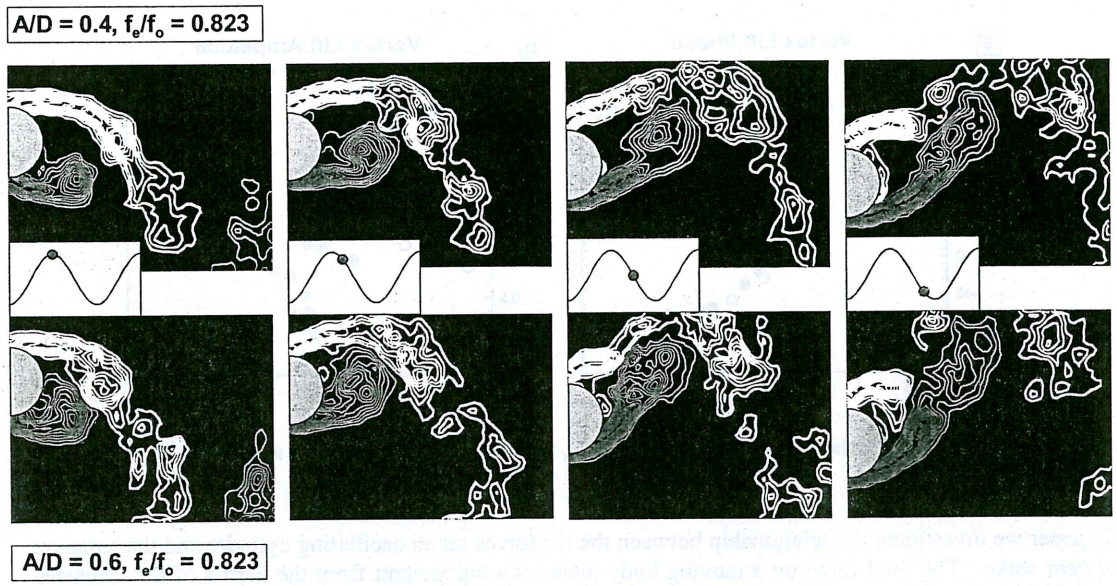


**Figure 2 Phase averaged vortex structures for the low frequency wake state as the cylinder moves through its downwards stroke. The amplitude of oscillation in the upper row is A/D = 0.4, while the lower row shows the corresponding images at A/D = 0.6. The inserts indicate the displacement of the cylinder.**

## 3.2 VORTEX LIFT FORCE

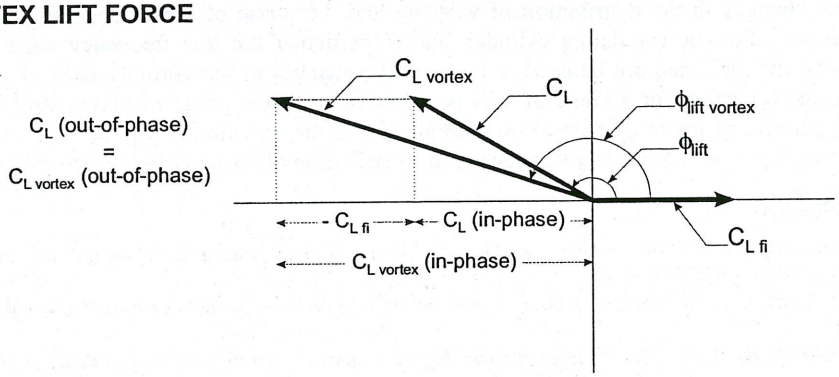


**Figure 3 Vector diagram showing the relationship between $C_L(t)$ and $C_{L\ vortex}(t)$.**

The vortex lift force is calculated using equation (1) by subtracting the fluid inertia force $F_{fi}$ from the total lift force. The fluid inertia, $F_{fi} = -\rho\ Vol\ d^2y(t)/dt^2$, is purely in-phase with y(t) and subtracting $F_{fi}$ does not alter the out-of-phase component of the lift force. The magnitude of $F_{fi}$ increases with the amplitude of oscillation, therefore as A/D increases from 0.4 to 0.6 there is a 50% increase in the magnitude of $F_{fi}$. The vector relationship between $C_L(t)$ and $C_{L\ vortex}(t)$ in Figure 3, demonstrates that the subtraction of $F_{fi}$ affects both the phase and amplitude of the lift force. The vortex lift force is now expressed in the same way as the total lift force:

$$C_{L\ vortex}(t) \approx C_{L\ vortex} \sin(2\pi f_e t + \phi_{lift\ vortex}) \qquad (3)$$

The variation of the phase and amplitude of the vortex lift force (Figure 4) is significantly different from the phase and amplitude of the total lift force (Figure 1). For both the low and high frequency wake states there is a collapse of $\phi_{lift\ vortex}$ for all values of A/D. For the low frequency wake state $\phi_{lift\ vortex}$ collapses towards

180°, while for the high frequency wake mode the vortex lift phase tends towards –90°. Unlike $C_L$, $C_{L\ vortex}$ increases with $f_e/f_o$ for both the low and high frequency wake modes and at transition $C_{L\ vortex}$ jumps downwards. For the low frequency wake state $C_{L\ vortex}$ increases with A/D, while for the high frequency wake state $C_{L\ vortex}$ does not vary significantly with A/D. Therefore, the magnitude of the jump in $C_{L\ vortex}$ at transition varies with A/D.

The collapse of $\phi_{lift\ vortex}$ indicates that for both wake states the phase of vortex shedding is approximately independent of A/D. This is consistent with the timing of the vortex shedding for the low frequency wake state in Figure 2. The vorticity fields for the high frequency wake state (not shown) also show that the phase of vortex shedding does not vary with A/D. According to equation (1) a change in the distribution of vorticity will alter the magnitude of the lift force on the cylinder. Thus the variation of $C_{L\ vortex}$ with A/D for the low frequency wake state, is consistent with the change in the distribution of vorticity observed in Figure 2.

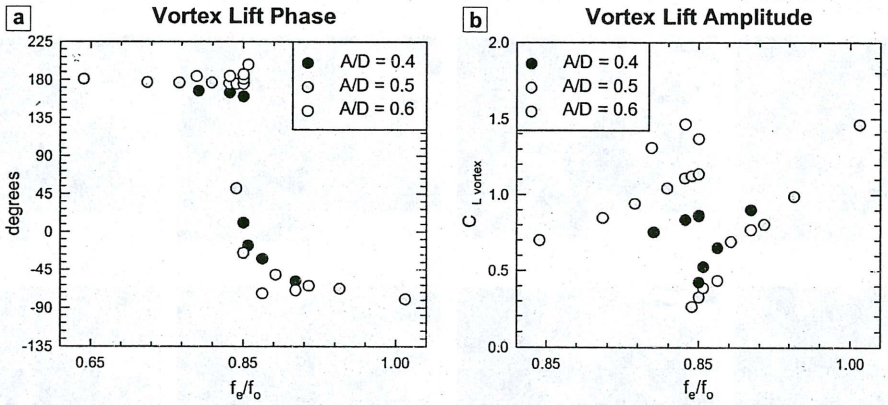


**Figure 4 Variation of $\phi_{lift\ vortex}$ and $C_{L\ vortex}$ with $f_e/f_o$, for A/D = 0.4, 0.5 and 0.6.**

## 4. CONCLUSION

In this paper we investigate the relationship between the lift forces on an oscillating cylinder and the structure of the near wake. The total force on a moving body includes a component from the inertia of the displaced fluid, $F_{fi}$ and a component due to the rate of change of the vorticity field, $F_{vortex}$. The lift forces on a cylinder oscillating transverse to the free-stream were examined for a range of oscillation amplitudes and frequencies. To determine the difference between the total force and the vortex force we compare the changes in $C_L(t)$ and $C_{L\ vortex}(t)$ with the changes in the distribution of vorticity and the phase of vortex shedding, as A/D and therefore $F_{fi}$ increases. For the oscillating cylinder, and in particular the low frequency wake state, it is evident that the total lift force can not be used to interpret the changes in the vorticity field. However, the collapse of the vortex lift phase for a range of A/D is consistent with the phase of vortex shedding, which appears to be independent of the amplitude of oscillation. While the variation of $C_{L\ vortex}$ with A/D for low frequency wake state, is consistent with the changes in the distribution of vorticity in the near wake.

## 5. REFERENCES

BISHOP, R. E. D. & HASSAN, A. Y., 1963, "The Lift and Drag Forces on a Circular Cylinder in a Flowing Fluid", *Proceedings of Royal Society, London, Series A*, vol. **277**, 32 – 50.

CARBERRY, J., SHERIDAN, J. & ROCKWELL, D. 2001, "Forces and wake modes of an oscillating cylinder", *Journal of Fluids and Structures*, **15**, 523-532

GU, W., CHYU, C. & ROCKWELL, D., 1994, "Timing of vortex formation from an oscillating cylinder", *Physics of Fluids* **6**, 3677-3682.

GOPALKRISHNAN, 1993, Vortex Induced Forces on Oscillating Bluff Cylinders, *MIT Doctoral Dissertation.*

GOVARDHAN, R & WILLIAMSON, C. H. K. 2000 Modes of vortex formation and frequency response of a freely vibrating cylinder, *J. Fluid Mech.*, **420**, 85-130.

MERCIER, J. A., 1973, "Large amplitude oscillations of a circular cylinder in a low-speed stream", *Stevens Institute of Technology, Ph.D., 1973. Engineering ,Mechanical.*

ONGOREN, A. & ROCKWELL, D., 1988, "Flow structure from an oscillating cylinder Part1. mechanisms of phase shift and recovery in the near wake", **191**, 197-223.

SARPKAYA, T., 1995,"Hydrodynamic Damping, Flow-Induced Oscillations, and Biharmonic Response", *ASME Journal of Offshore Mechanics and Artic Engineering*, Vol. **177**, 232-238.

STAUBLI, T. 1983b Untersuchung der oszillierenden Krafte am querangestromten, schwingenden Kreiszylinder. Dissertation ETH 7322.

WILLIAMSON, C. H. K. & ROSHKO, A., 1988, "Vortex Formation in the Wake of an Oscillating Cylinder", *Journal of Fluids and Structures*, **2**, 355-381.

WU, J.C., 1981, "Theory for Aerodynamic Force and Moment in Viscous Flows", *AIAA Journal*, **19 (4)**, 432-441

*Melbourne Graduate Fluids Conference, 2001*
*Monash University, Melbourne, Australia*

# INVESTIGATING THE MOTION OF TETHERED BLUFF BODIES IN STEADY FLUID FLOW

**A. R. KEENE and J. SHERIDAN**

Department of Mechanical Engineering
Monash University, Clayton, Victoria, AUSTRALIA

## ABSTRACT

The motion of tethered bluff bodies subject to steady fluid flow has been investigated experimentally using a video motion-capturing technique. Both tethered spheres and cylinders were investigated in this study; tethered spheres were investigated to verify the motion-capturing method, and tethered cylinders as part of a new area of research. Comparisons are made not only between the two types of tethered bluff bodies, but also between elastically mounted cylinders and those constrained by tethers. Additional work is being undertaken to further understand the oscillation characteristics of the tethered cylinder.

## 1. INTRODUCTION

There have been a number of studies that investigated tethered bodies subject to free surface waves, but little has been done on tethered bodies below a free surface in steady fluid flow. Govardhan & Williamson (1997) investigated the oscillation amplitude and frequency of tethered spheres at different mass ratios (the ratio of body mass to the mass of the displaced fluid), $m^* = 0.01 - 0.9$, and tether length ratios (where the tether length is nondimensionalised by body diameter), $L^* = 3 - 9$, in a water tunnel. They found that the direction of motion of largest amplitude of the tethered sphere is normal to the flow, with transverse oscillations being up to four times larger than those in the streamwise direction, so this direction was the focus of their observations. Figure 1 below shows the oscillation amplitude for two different tether lengths compared to Reynolds number, $Re$, and reduced velocity, $U^*$ (the inverse of Strohaul number, St). Figure 1(b) shows that the data for different tether length ratios actually collapse onto a single curve for the same mass ratio ($m^* = 0.76$). For the range of flow speeds investigated, it can be seen that there are two significant peaks of oscillation amplitude – a local peak at $U^* \approx 5$ (defined as mode I) and then a higher peak at $U^* \approx 10$ that continues through to the highest value of $Re$ tested in these experiments (mode II). The authors comment that as the oscillation amplitude remains constant, mode II appears to be the saturation amplitude of the system.

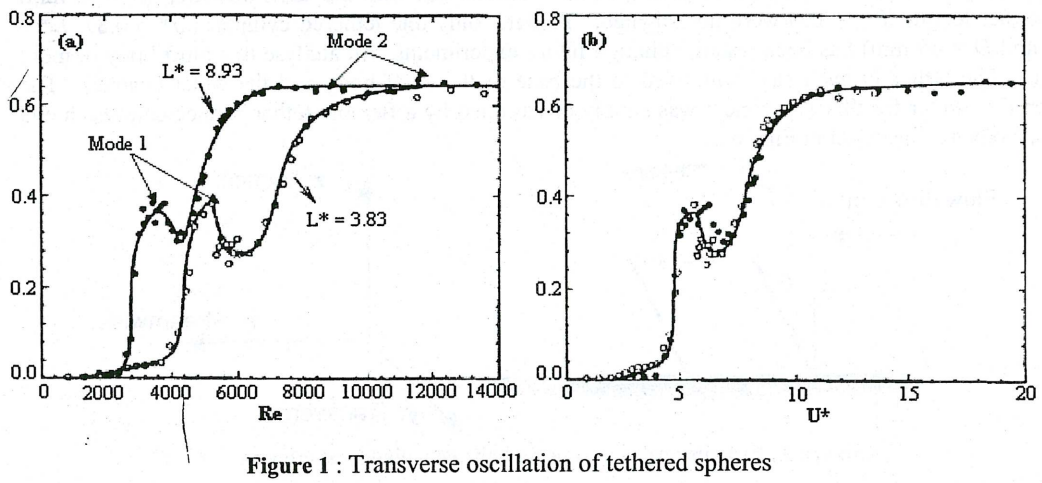


**Figure 1** : Transverse oscillation of tethered spheres

Jauvtis et al. (2000) investigated the motion of tethered spheres with higher mass ratios ($m^* = 75 - 940$) in wind tunnels, which allowed the range of $U^*$ to be increased substantially compared to the earlier studies by Govardhan & Williamson. Modes I and II were again observed for this high mass ratio case, although it was found that there is a sharp drop in oscillation response after the mode II

peak, and a third oscillation peak (mode III) is found at larger $U^*$. No explanation for this third mode has been given at this stage.

Figure 1 shows that a change in tether length does not affect the amplitudes of oscillation of the system, although it does change the Reynolds numbers at which the modes of oscillation occur. The oscillation data collapses onto the same curve when plotted against $U^*$. Figure 2 (Govardhan & Williamson, 1997) shows the transition of sphere motion for constant tether length and mass ratio ($m^* = 0.082$ and $L^* = 9.3$). The pattern of the sphere oscillations show that as the Reynolds number increases, the phase between the streamwise and transverse motions changes, and the phase plot transforms from a 'crescent' shape (a) to a 'figure-8' shape (c). In each of these cases, although the streamwise and transverse frequencies are increasing with Re, they remain at a ratio of 2:1. Williamson & Govardhan (1997) suggest that this is because streamwise oscillations become phase-locked with the transverse oscillations and vibrate at twice the frequency of the transverse.

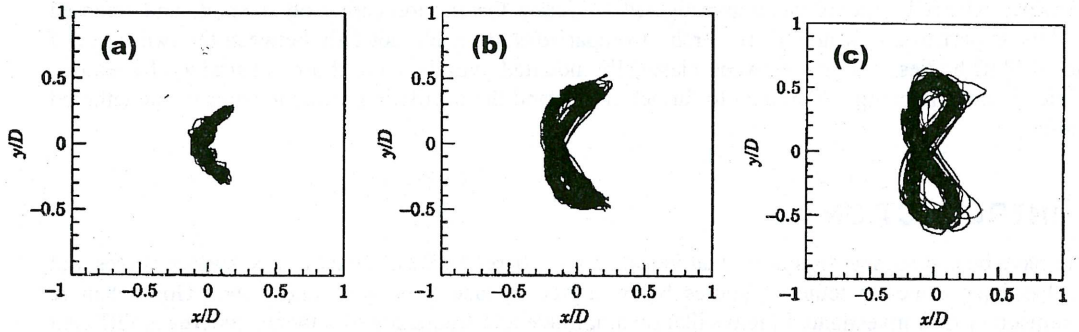


**Figure 2** : Tethered sphere oscillations for (a) $Re = 5{,}132$, (b) $Re = 9{,}176$ and (c) $Re = 11{,}310$.

The other tethered bluff body investigated in this paper, the cylinder, does not appear to have been previously investigated under these flow conditions.

## 2. EXPERIMENTAL METHOD

Experiments were performed on tethered spheres and cylinders in order to observe the dynamics of these bluff bodies when they are subjected to uniform flow conditions in a water channel of cross-section 304 mm x 310 mm.

Tethered spheres of two different mass ratios ($m^* = 0.22$, 0.82) with the same diameter ($D = 35$ mm) and tether length ($L^* = 3.5$) were investigated. To date, only one tethered cylinder ($m^* = 0.87$, $L^* = 3.5$, and $D = 40$ mm) has been tested, although future experiments will analyse this bluff body in more depth. The tether in each case was fixed to the base of the bluff body and the water channel. The tethered cylinder for this experiment was simply constrained by a flexible tether connected at each end of the body as illustrated in Figure 3.

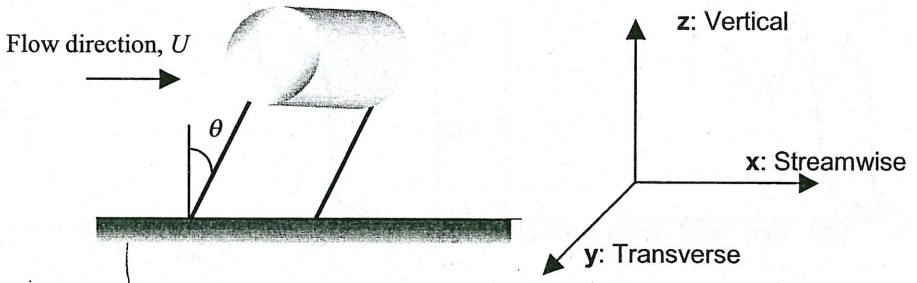


**Figure 3** : Experimental apparatus for tethered cylinder experiment.

The bluff body displacement was recorded by a digital video camera mounted next to the working section, in the significant plane of oscillation. For the case of the tethered sphere the camera was set up to record in the x-y plane (refer to axes shown in Figure 3), while the tethered cylinder was measured in the x-z plane. The motion data collected from the camera is then transferred to a computer where the frames were digitally processed. Using a computer package, each frame of information from the

video camera was analysed and the position of the body recorded. A sample set of results using this technique is shown in Figure 6 in Section 3.2 of this paper.

# 3. RESULTS AND DISCUSSION

## 3.1 TETHERED SPHERE EXPERIMENTS

For low values of $m^*$ there was found to be a strong relationship between the oscillation results of the two sets of experiments, although water tunnel restrictions prevented testing at higher $U^*$. Figure 5 shows that the experimental results follow the trend of the data presented by Govardhan & Williamson (1997), although the expected initial peak (mode I) was not noticeable when comparing $y_{RMS}$ to either $Re$ or $U^*$. Figure 5 also shows different $y_{RMS}$ values for the same values of flow speeds. This is believed to be a result of the fluctuating flow speed in the water channel used for these experiments.

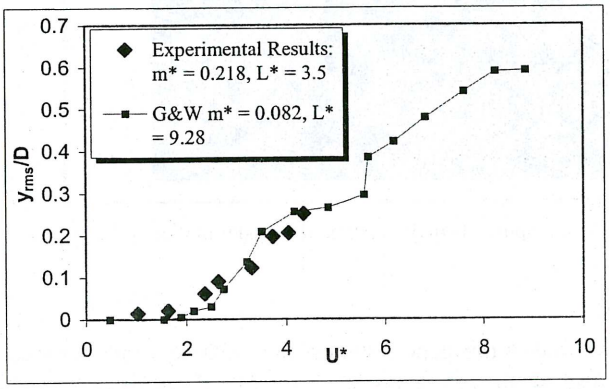


**Figure 4** : Tethered sphere oscillation values at low m*.

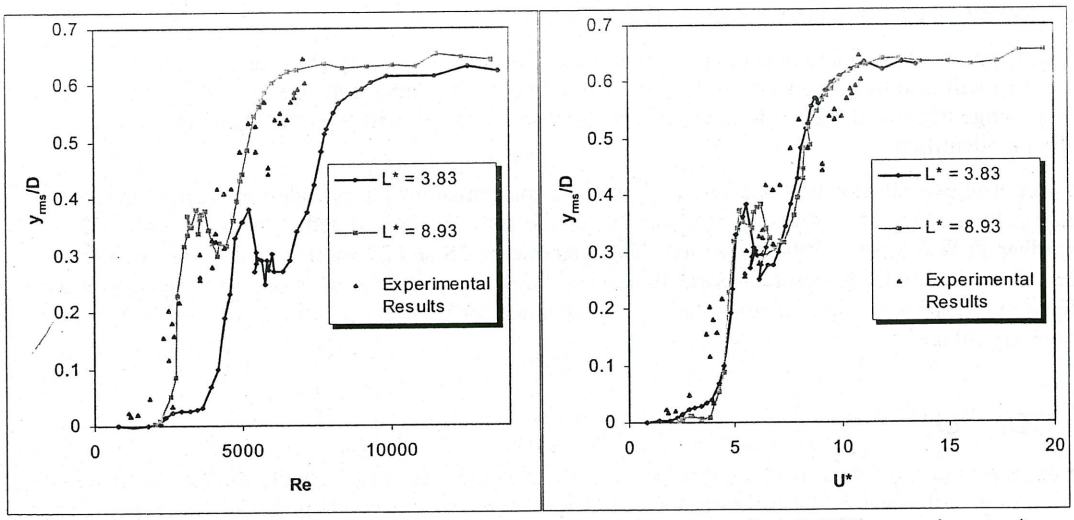


**Figure 5** : Tethered sphere oscillation values compared to $Re$ and $U^*$. Govardhan & Williamson data at $m^* = 0.76$, experimental data $m^* = 0.82$.

Although these results did not clearly show the modes of oscillation found in the results of Govardhan & Williamson, they did demonstrate that precise experimental conditions are required to get reliable results from the oscillating bluff body, which was not achievable with the water channel used for these initial experiments. Further experiments (discussed in Section 3.3) will be performed in a water channel where these variations in flow conditions will not be present.

## 3.2 TETHERED CYLINDER EXPERIMENTS

Figure 6 shows the oscillation pattern for the tethered sphere at one of the flow velocities investigated. These results show that the cylinder motion is in the shape of an arc, and that the streamwise (x)

oscillation is most significant for this bluff body, unlike the transverse oscillations of the tethered sphere. Despite the flexible tether used in these experiments, the tether remained constantly in tension (mainly due to the buoyant effects of the cylinder), and very little bending or movement of the cylinder in the transverse direction was present, despite the varying flow conditions present in the water channel.

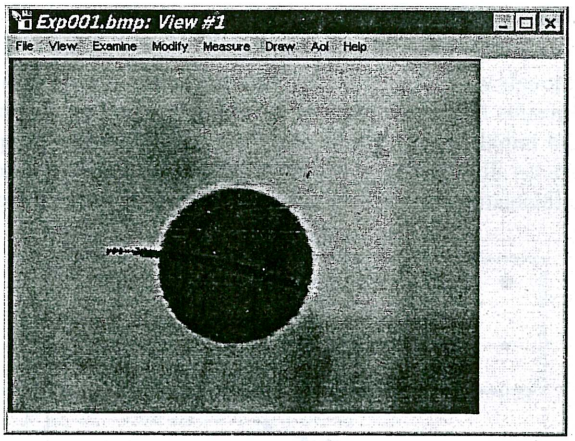


**Figure 6** : Computer display of tethered cylinder motion at $U^* = 14.2$.

### 3.3 FURTHER WORK

The initial experiments described in this paper established a reliable means for recording position data with respect to time, and also identified significant directions of oscillation for tethered spheres and cylinders. Despite the fact that the primary direction of motion is different for spheres and cylinders, future experiments will compare the motion of tethered spheres and tethered cylinders at the same mass ratios and tether lengths in the x-z plane to see if a relationship exists.

Further experiments will be conducted in a new water channel of working cross-section 600 mm x 600 mm, which will also have more controllable flow conditions. By varying $m^*$ and $L^*$ within the reduced velocity range of $U^* = 0 - 20$, it is expected that the area of interest will be covered and the branches of oscillation identified.

The proposed experiments will not only look at the displacement of the cylinder but also at the vortex shedding in the cylinder wake and the forces on the bluff body and tether with respect to time. Govardhan & Williamson (2000) observed a change between 2S and 2P wake vortex modes at different values of oscillation frequency for elastically mounted cylinders, whether a similar result occurs for the tethered cylinder case will be investigated. The apparatus for these proposed experiments is currently in the design stage.

## 4. CONCLUSION

The experiments described in this paper provide some interesting initial results for the dynamics of tethered bodies that justify further research in this area. A series of much more detailed experiments involving tethered cylinders will be performed to further this study.

## 5. REFERENCES

GOVARDHAN, R. and WILLIAMSON, C.H.K., "Vortex-induced motions of a tethered sphere", *Journal of Wind Engineering and Industrial Aerodynamics*, **69-71,** 375-385, 1997.

JAUVTIS, N., GOVARDHAN, R. and WILLIAMSON, C.H.K., "Multiple modes of Vortex-Induced Vibration of a Sphere", *Journal of Fluids and Structures*, **15**, 555-563, 2001.

WILLIAMSON, C.H.K. and GOVARDHAN, R., "Dynamics and forcing of a tethered sphere in a fluid flow", *Journal of Fluids and Structures*, **69-71,** 375-385, 1997.

GOVARDHAN, R. and WILLIAMSON, C.H.K., "Modes of vortex formation and frequency response of a freely vibrating cylinder", *Journal of Fluid Mechanics*, **420,** 85-130, 2000.

*Melbourne Graduate Fluids Conference, 2001*
*Monash University, Melbourne, Australia*

# THREE-DIMENSIONAL NUMERICAL INVESTIGATION OF FLOW PAST A ROTATING SPHERE

**C.J. Pregnalato, M.C. Thompson and K. Hourigan**

Department of Mechanical Engineering
Monash University, Clayton, Victoria, AUSTRALIA

## ABSTRACT

The flow past a rotating sphere is investigated numerically using a spectral element/spectral direct numerical simulation. The effect of sphere rotation on transition regimes is analysed for Reynolds numbers of $100 < Re < 300$, where $Re$ is the Reynolds number based on freestream velocity $U$, sphere diameter $d$ and kinematic viscosity $\nu$. The results show that the Reynolds numbers for the first transition to three-dimensionality, $Re_1$, and the second transition to time-dependence, $Re_2$, are functions of the angular velocity of the sphere $\Omega$ (normalised by the sphere radius and freestream velocity) and correspondingly occur at different $Re$ than is observed for a fixed (non-rotating) sphere.

## 1. INTRODUCTION

Previous investigations of the motion of a spinning sphere have mainly dealt with small particle Reynolds numbers, namely $Re_p$ much less than unity. However, in recent years experiments have been performed on the lift of spinning spheres at intermediate $Re$. Oesterle and Bui Dinh (1998) looked at Reynolds numbers less than 140, and proposed an empirical expression to estimate the lift coefficient within this range and for dimensionless angular velocities varying from 1 to 6. In spite of this, they could not explain the behaviour of the lift coefficient in terms of $Re$ and $\Omega$ and acknowledge that further information is required concerning the flow structure around the sphere.

Ece (1992) considered the unsteady boundary-layer flow past an impulsively started translating and spinning axisymmetric body of general shape, in which the stream function and swirl velocity were expanded in series in powers of time. They found that the rotation reduces the friction drag and increasing the spin rate causes a sooner onset of flow separation. Also, the point of separation advances upstream initially very fast and then asymptotes toward its steady-state value slowly. For any given time, the angle of separation is larger for a higher spin rate. However, these results are limited to the early stages of the boundary layer flow, and numerical integration of the boundary layer equations is necessary to extend the solutions to larger values of time.

A finite volume formulation was used by Salem and Oesterle (1998) to investigate a shear flow around a spinning sphere for $Re < 40$. Compared with uniform flow past a sphere, their results indicate that the drag is not altered by the rotation of the sphere, provided that the Reynolds number is low enough. Moreover, the lift and drag coefficients were found to be significantly sensitive to the grid parameters, so that the reported results were restricted to small $Re$.

Kurose and Komori (1999) performed three-dimensional computations of the flow around a rotating sphere in a linear shear flow. The rotation rates investigated were in the range $0 < \Omega < 0.25$, whereas the Reynolds number ranged from 1 to 500. In this study, it was found that the drag increases with increasing rotation. Also, the sign of the lift coefficient remain unchanged with increasing $Re$ in contrast to a fixed sphere in a linear shear flow, and approached a constant value for $Re > 200$ for a given rotational speed. This asymptotic value of the lift coefficient increased with increasing rotation rate, as did the Strouhal number $St$. Expressions for lift and drag were proposed for the parameter range investigated.

It is the purpose of the present paper to analyse the effect of sphere rotation on the primary transition regimes of the flow around a sphere. In particular, computations were carried out for $100 < Re < 300$ and $0 < \Omega < 0.25$. The effects of varying spinning orientations were clarified by rotating the sphere about all three primary axes. Finally, wake vortex structures are presented in the form of isosurfaces of the second largest eigenvalue of $\boldsymbol{S}^2 + \boldsymbol{R}^2$, where $\boldsymbol{S}$ and $\boldsymbol{R}$ are the symmetric and antisymmetric components of the velocity gradient tensor $\nabla \boldsymbol{u}$, as suggested by Jeong and Hussain (1995).

## 2. NUMERICAL METHOD

The velocity-pressure field was solved in primitive variable form using a hybrid spectral element/spectral method incorporated for axisymmetric problems. The procedure involves solving the time-dependent incompressible Navier-Stokes and continuity equations:

$$\frac{\partial \boldsymbol{u}}{\partial t} = -(\boldsymbol{u}\cdot\nabla\boldsymbol{u}) - \nabla p + \frac{1}{Re}\nabla^2\boldsymbol{u}$$

$$\nabla\cdot\boldsymbol{u} = 0\,.$$

In all the simulations presented, eighth order tensor product Lagrange polynomial expansions were used for all elements in the *s-r* plane, and a conventional Fourier expansion is utilised to extrapolate the two-dimensional mesh into three dimensions. A three-step time-splitting technique was used for unsteady simulations. Further details of the method may be found in Thompson *et al.* (1996).

## 3. RESULTS AND DISCUSSION

### 3.1 GRID RESOLUTION STUDY

An extensive study was performed to determine the effects of varying the grid parameters on the numerical solution. Table 1 summarises these results. A point immediately downstream of the sphere and located close to the separating shear layer was chosen, and streamwise velocity fluctuations were measured for $Re$ = 100. This location was chosen due to the high velocity gradients experienced there, and gave a good indication of the adequacy of the resolution there. Initially, a test grid (Test) was used which was then modified by increasing the number of elements in the vicinity of the sphere as well as in the downstream wake (Mesh1). Blockage effects were also examined by using a mesh whose inlet and radial dimensions were half the dimensions of the original mesh (Mesh 2 in Table 1), as well as a mesh whose dimensions were double that of the original mesh. To examine the effect of the outlet position, another mesh was constructed in which the outlet was distanced twice as far as the original mesh, whilst maintaining the same mesh concentration (and hence more elements), and it was observed that very little change in solution occurred. It is evident in Table 1 that for all meshes, increasing the order of the tensor products only increased the accuracy marginally. A difference in solution of approximately 0.3% was found between Mesh1 and Mesh2, relating the fact that blockage did not have a significant effect. However, for the purposes of flow visualisation, Mesh1 was chosen with $N$ = 8 for all simulations (Figure 2).

| N | Test | % Difference | Mesh1 | % Difference | Mesh2 | % Difference |
|---|---|---|---|---|---|---|
| 7 | 1.0030452 | 8.91664E-05 | 1.0030653 | 0.000105878 | 1.0060042 | 2.90335E-05 |
| 8 | 1.0029429 | 1.28061E-05 | 1.0029445 | 1.45021E-05 | 1.0059533 | 2.15294E-05 |
| 9 | 1.0030042 | 4.82823E-05 | 1.0030102 | 5.09642E-05 | 1.0059796 | 4.66612E-06 |
| 10 | 1.0029558 | 0 | 1.0029591 | 0 | 1.005975 | 0 |

**Table 1** Grid resolution study for an axisymmetric sphere.

| Author | Method | $St$ ($Re$ = 300) |
|---|---|---|
| Present (2000) | Spectral-Element | 0.134 |
| Johnson & Patel (1999) | Finite-Volume | 0.137 |
| Kurose & Komori (1999) | Finite-Difference | 0.128 |
| Tomboulides *et al.* (1993) | Spectral-Element | 0.136 |
| Tomboulides *et al.* (2000) | Spectral-Element | 0.136 |
| Ormieres & Provansal (1999) | Experimental | 0.123 |
| Sakamoto & Haniu (1990) | Experimental | 0.15 - 0.18 |

**Table 2** Comparisons of Strouhal number $St$ at a Reynolds number of 300.

## 3.2 FIXED SPHERE COMPUTATIONS

Initially, computations were performed for the case of a fixed sphere in order to validate the numerical procedure. The parameter of choice to monitor was the vortex shedding frequency $f$ at a Reynolds number of 300. This parameter is known to be sensitive to the grid dimensions (and in particular to blockage), and in non-dimensional form is known as the Strouhal number $St$. Table 2 summarises the Strouhal numbers obtained at $Re = 300$ from the present and previous studies. It also demonstrates that the present numerical code is well suited to the problem of bluff body vortex shedding.

## 3.3 ROTATING SPHERE COMPUTATIONS

Simulations were performed for the rotating sphere with dimensionless angular velocities varying from $0.05 < \Omega < 0.25$. Initially, the sphere was forced to rotate about the $z$-axis, and lift, drag and side-force coefficients were computed. Figure 1 presents lift and drag coefficients as a function of angular velocity for a Reynolds number of 200. For comparison, the results of Kurose and Komori (1999) are also depicted. The results show that both the lift and drag increase with an increase in sphere rotation, in accordance with previous findings (see, for example, Oesterle and Bui Dinh (1998)).

Table 3 shows the contributions of lift, drag and side forces for selected rotation rates at a Reynolds number of 200. It is evident that a streamwise rotation of the sphere results in zero lift and side force. It is also interesting to note that the drag of a streamwise-rotating sphere is less than the drag of a sphere which is rotating about the other axes. Furthermore, although not shown here, it was found that the contribution to the drag from viscous forces was of the same order as the contributions from the pressure, for $Re > 100$. In contrast, the viscous force contributions to the lift and side forces were an order of magnitude lower than the pressure contributions.

Figures 2a and 2b illustrate the vortical structure of the wake of a spinning sphere, rotating at $\Omega = 0.05$ about the $z$-axis and $y$-axis respectively at a Reynolds number of 200. Clearly visible is the double-threaded wake which is observed for a fixed sphere after $Re \approx 212$. It appears that the non-streamwise rotation of the sphere promotes conversion of azimuthal vorticity into streamwise vorticity, caused by the tilting of fluid rings as they pass close to the surface of the sphere (Thompson *et al.* (2000)). However, a rotation about the streamwise ($x$) axis forces the fluid immediately adjacent to the sphere to flow downstream parallel to the axis of symmetry. As a result, the fluid rings do not tilt as they pass close to the sphere's surface, and the double-threaded wake is not observed. Indeed, recent computations have observed that for a relatively small streamwise rotation, the wake remains axisymmetric up to a Reynolds number approaching 280 which, for a non-rotating sphere, is characterized by the presence of periodic vortex loops.

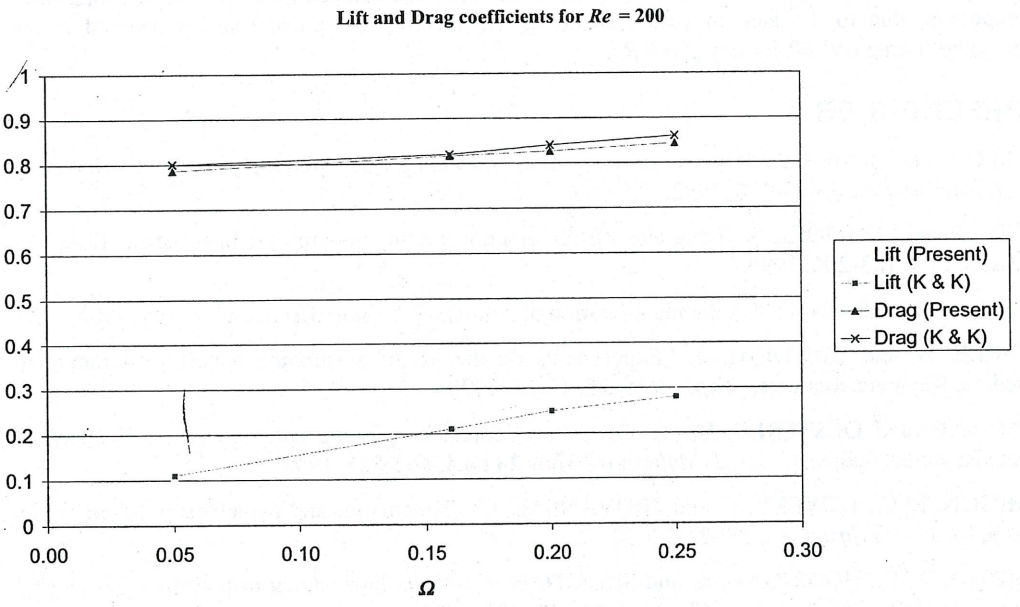


**Figure 1** Lift and drag coefficients as a function of sphere rotation.

| | $\Omega x$ | | | $\Omega y$ | | | $\Omega z$ | | |
|---|---|---|---|---|---|---|---|---|---|
| $\Omega$ | Cd | Cl | Cs | Cd | Cl | Cs | Cd | Cl | Cs |
| 0.05 | 0.7753 | 0 | 0 | 0.7862 | 0 | 0.1013 | 0.7862 | 0.1013 | 0 |
| 0.15 | 0.7762 | 0 | 0 | 0.8102 | 0 | 0.2147 | 0.8102 | 0.2147 | 0 |
| 0.16 | 0.7767 | 0 | 0 | 0.8164 | 0 | 0.2264 | 0.8133 | 0.2250 | 0 |

**Table 3** Effect of sphere rotation on forces for selected angular velocities.

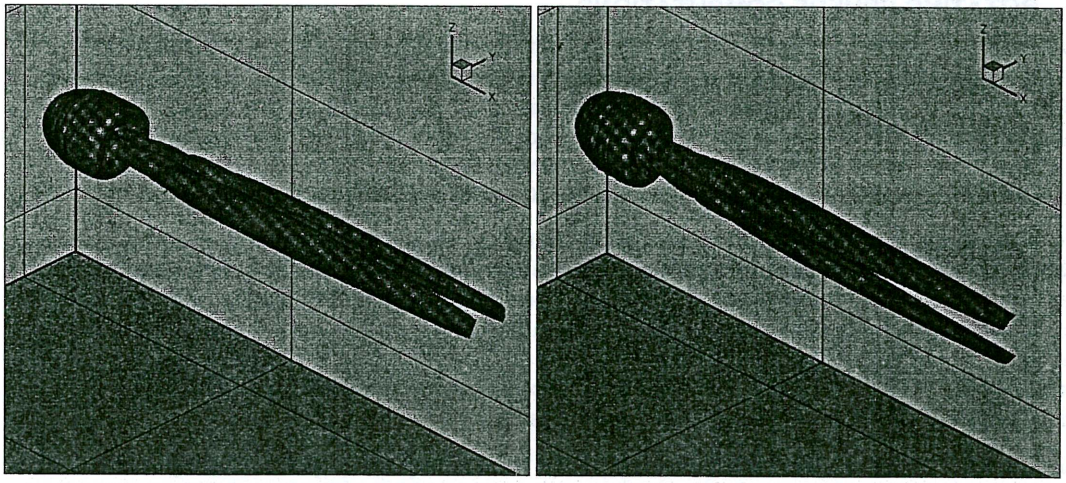

(a) (b)

**Figure 2** "Double-thread" vortex structures in the wake of a rotating sphere, with (a) $\Omega_y = 0.05$, and (b) $\Omega_z = 0.05$. Note that the surface of the sphere is obstructed from view by the $-\lambda_2$ isosurface in accordance with Jeong and Hussain (1995).

## 4. CONCLUSION

The flow about a rotating sphere was analysed numerically using a three-dimensional spectral element/spectral method for axisymmetric geometries. It was found that a non-streamwise sphere rotation caused an earlier transition to non-axisymmetry, whereas a streamwise rotation resulted in a greatly delayed transition in relation to the Reynolds number. This delayed transition resulted in a zero lift component, due to the lack of vortex shedding. An increase in sphere rotation resulted in an increase in both drag and lift for any given *Re*.

## 5. REFERENCES

ECE, M.C. "The initial boundary-layer flow past a translating and spinning rotational symmetric body," *J. Eng. Math.* **26**, 415-428, 1992.

KUROSE, R. and KOMORI, S. "Drag and lift forces on a rotating sphere in a linear shear flow," *J. Fluid Mech.* **384**, 183-206, 1999.

JEONG, J. and HUSSAIN, F. "On the identification of a vortex," *J. Fluid Mech.* **285**, 69-94, 1995.

OESTERLE, B. and BUI DINH, T. "Experiments on the lift of a spinning sphere in a range of intermediate Reynolds numbers," *Exp. Fluids* **25**, 16-22, 1998.

SALEM, M.B. and OESTERLE, B. "A shear flow around a spinning sphere: numerical study at moderate Reynolds numbers," *Int. J. Multiphase Flow* **24** no.4, 563-585, 1998.

THOMPSON, M.C., LEWEKE, T. and PROVANSAL, M. "Kinematics and dynamics of sphere wake transition," *J. Fluids Struct.* **15**, ???-???, 2000.

THOMPSON, M.C., HOURIGAN, K. and SHERIDAN, J. "Three-dimensional instabilities in the wake of a circular cylinder," *Exp. Therm. Fluid Sci.* **12**, 190-196, 1996.

*Melbourne Graduate Fluids Conference*
*Monash University, Melbourne, Australia*
*January 2001*

# Evolution of an Azimuthal Mode 4 Instability in a Circular Vortex

**Keith HIGGINS, Andrew OOI and M. S. CHONG**

Department of Mechanical and Manufacturing Engineering
The University of Melbourne, Victoria 3010, AUSTRALIA

## ABSTRACT

A numerical simulation on an infinite radial domain shows that 'square' vortices can emerge from the unstable evolution of perturbed isolated circular vortices. A second instability is observed in which the square vortex breaks into two dipoles.

## 1. INTRODUCTION

Laboratory experiments have revealed that a range of compound vortices can emerge in a two dimensional flow due to the growth of instabilities of isolated circular vortices (Carnevale & Kloosterziel 1994). These compound vortices include dipoles, tripoles, quadrupoles, and more recently, the observation of a 'square' vortex (Kloosterziel & Carnevale 1999). There have been a number of numerical studies of such phenomena, including Carton *et.al.* (1989) and Kloosterziel & Carnevale (1999).

Carton *et.al.* (1989) and Kloosterziel & Carnevale (1999) investigated the stability of circular vortices with a radial vorticity profile of the form

$$\omega_\alpha(r) = \left(1 - \frac{1}{2}\alpha r^\alpha\right) e^{-r^\alpha}, \tag{1}$$

where $\alpha$ determines the shape of the profile. For $\alpha > 0$, all these vortices have an inflection point. The corresponding azimuthal velocity profiles are given by $v_\alpha(r) = \frac{1}{2} r \exp(-r^\alpha)$. The flow is everywhere counter-clockwise. The vorticity is positive near the origin, and is surrounded by a ring of negative vorticity.

These isolated vortices have zero circulation, such that $\int_0^{2\pi}\int_0^\infty \omega(r,\theta,t) r \mathrm{d}r = 0$. As a necessary condition for instability, Rayleigh's inflection point theorem requires $\mathrm{d}\omega/\mathrm{d}r$ to change sign somewhere (Drazin & Reid 1981). For vortices with zero circulation, $\mathrm{d}\omega/\mathrm{d}r$ always changes sign somewhere if $\omega$ is continuous. The presence of an inflection point does not imply instability, it only indicates possibly unstable vortices. For small enough $\alpha$, these vortices are linearly stable. However, as $\alpha$ is increased, they first become unstable to perturbations of azimuthal wavenumber $k' = 2$, then $k' = 3, 4$.

Kloosterziel & Carnevale (1999) considered such a problem, subject to initial perturbations of the form

$$\omega'_\alpha(r) = \mu \cos(k'\theta) \exp\left[\frac{-(\alpha r^\alpha - 2)^2}{2\sigma^2}\right] \tag{2}$$

where $\mu$ and $\sigma$ are parameters used to adjust the amplitude and distribution of the disturbance. They employed a spectral method on a doubly periodic Cartesian domain with dimensions of $10 \times 10$ units. They added a dissipative term of the form $\nu_4(\nabla^2)^2\omega$ to the vorticity equation. This so-called hyperviscosity prevents build-up of small scale enstrophy. The limitations associated with the periodic cartesian domain and hyperviscosity motivated a study of instabilities using an infinite radial domain Navier-Stokes code.

We consider a numerical study of such phenomena in polar coordinates using an infinite radial domain Navier-Stokes code (Buntine & Pullin 1989). The numerical method employs Fourier expansions in the azimuthal direction and finite differences in the radial direction.

We study the behaviour of an isolated vortex subject to an azimuthal mode 4 perturbation. Without the restriction of periodic Cartesian boundary conditions, the formulation allows us to observe a dipole splitting event. Finally, we consider the time evolution of the azimuthal modes $A_k = Q_k^{1/2}$, where $Q_k$ is the enstrophy associated with wavenumber $k$.

## 2. FORMULATION AND NUMERICAL SOLUTION

The two-dimesional flow considered in this paper has uni-directional vorticity $\boldsymbol{\omega} = \omega(r,\theta)\hat{\boldsymbol{k}}$, such that $\boldsymbol{v} = \boldsymbol{v}(r,\theta)$ is the vortex induced velocity in the $(r,\theta)$ plane. The vorticity transport equation is then simplified to

$$\frac{\partial \omega}{\partial t} + \nabla \cdot (\boldsymbol{u}\omega) = \nu \nabla^2 \omega \tag{3}$$

where $\boldsymbol{\omega} = \nabla \times \boldsymbol{v}$ and $\nu$ is the kinematic viscosity. Since the fluid is incompressible, a stream function $\psi(r,\theta,t)$ can be associated with the $\boldsymbol{v}$ motion, $\nabla^2\psi = -\omega$. The velocity field is then,

$$\boldsymbol{v} = \frac{1}{r}\frac{\partial \psi}{\partial \theta}\hat{\boldsymbol{r}} - \frac{\partial \psi}{\partial r}\hat{\boldsymbol{\theta}}. \tag{4}$$

The vorticity transport equation and Poisson equation áre respectively

$$\frac{\partial \omega}{\partial t} + u_r\frac{\partial \omega}{\partial r} + \frac{u_\theta}{r}\frac{\partial \omega}{\partial \theta} = \frac{\nu}{r}\left\{\frac{\partial}{\partial r}\left(r\frac{\partial \omega}{\partial r}\right) + \frac{1}{r}\frac{\partial^2 \omega}{\partial \theta^2}\right\} \tag{5}$$

$$\frac{\partial^2 \psi}{\partial r^2} + \frac{1}{r}\frac{\partial \psi}{\partial r} + \frac{1}{r^2}\frac{\partial^2 \psi}{\partial \theta^2} = -\omega \tag{6}$$

The problem is to solve (4)-(6) numerically on an infinite radial domain, subject to the initial and boundary conditions on the vorticity field given by

$$\omega(r,\theta,t=0) \quad \text{given}, \quad \omega(r\to\infty,\theta,t)\to 0, \quad t \geq 0. \tag{7}$$

A hybrid spectral finite-difference method is employed (Buntine & Pullin 1989; Robinson & Saffman 1984). We represent $\omega$ and $\psi$ as

$$\omega(r,\theta,t) = \sum_{k=-\frac{N_\theta}{2}}^{\frac{N_\theta}{2}-1} \hat{\omega}_k(r,t)e^{ik\theta} \quad \text{and} \quad \psi(r,\theta,t) = \sum_{k=-\frac{N_\theta}{2}}^{\frac{N_\theta}{2}-1} \hat{\psi}_k(r,t)e^{ik\theta}. \tag{8}$$

where $r \in [0,\infty)$ and $\theta \in [0,2\pi)$ and $N_\theta$ is the azimuthal truncation parameter. Substitution of the truncated Fourier series (8) into Eqs. (4)-(6) gives evolution equations for the Fourier coefficients $\hat{\psi}_k$ and $\hat{\omega}_k$, $k = -\frac{1}{2}N_\theta \ldots \frac{1}{2}N_\theta + 1$.

There are two parts of the calculation: solution of the Poisson equation and time advancement. The Poisson equation (6) gives $N_\theta$ linear ODE's in $r$ for the Fourier coefficients $\hat{\psi}_k$ for given $\hat{\omega}_k$. These radial equations were solved on a finite domain obtained by a coordinate mapping

$$r = L\zeta/(1-\zeta) \tag{9}$$

which maps $r \in [0,\infty)$ onto $\zeta \in [0,1)$, where $L$ is a stretching parameter. The stretched equations were solved numerically using fourth-order finite differences at $N_r$ radial nodes. Although the velocity and vorticity fields are regular at the origin, the use of polar coordinates introduces a coordinate singularity there. The singularity is removed by expanding the streamfunction in a Taylor series about $r = 0$, ensuring that all terms are regular as $r \to 0$.

Once the $\hat{\psi}_k$ are known, the non-axisymmetric velocity field is constructed from spectral $\theta$-differentiation and fourth-order finite-differenced $\zeta$-differentiation. Then, making use of Eq. (5), $N_\theta$ ODE's in $t$ for $\hat{w}_k$ were obtained. The $\hat{w}_k$ were advanced in time using a second-order explicit predictor and a Crank-Nicolson, semi-implicit, two-point corrector scheme.

## 3. RESULTS AND DISCUSSION

Figure 1 shows the evolution of the vorticity contours for a radial vorticity distribution in which $\alpha = 7$, subject to an azimuthal wavenumber $k' = 4$ perturbation given by Eq. (2). At time $t = 0$, the vorticity contours are circular. The first instability develops at around $t = 25$. Four 'satellite' vortices have formed by $t = 75$, orbiting a core of positive vorticity which has become square in shape. A second instability develops by $t = 230$, and the satellites move towards each other and begin to merge. In subsequent frames, the positive core of vorticity is stretched until two vortex dipoles are formed. Spiral arms develop, as regions of weaker vorticity are left behind the faster rotating and stronger dipole cores. The dipoles convect away from the origin, leaving a residue of positive vorticity.

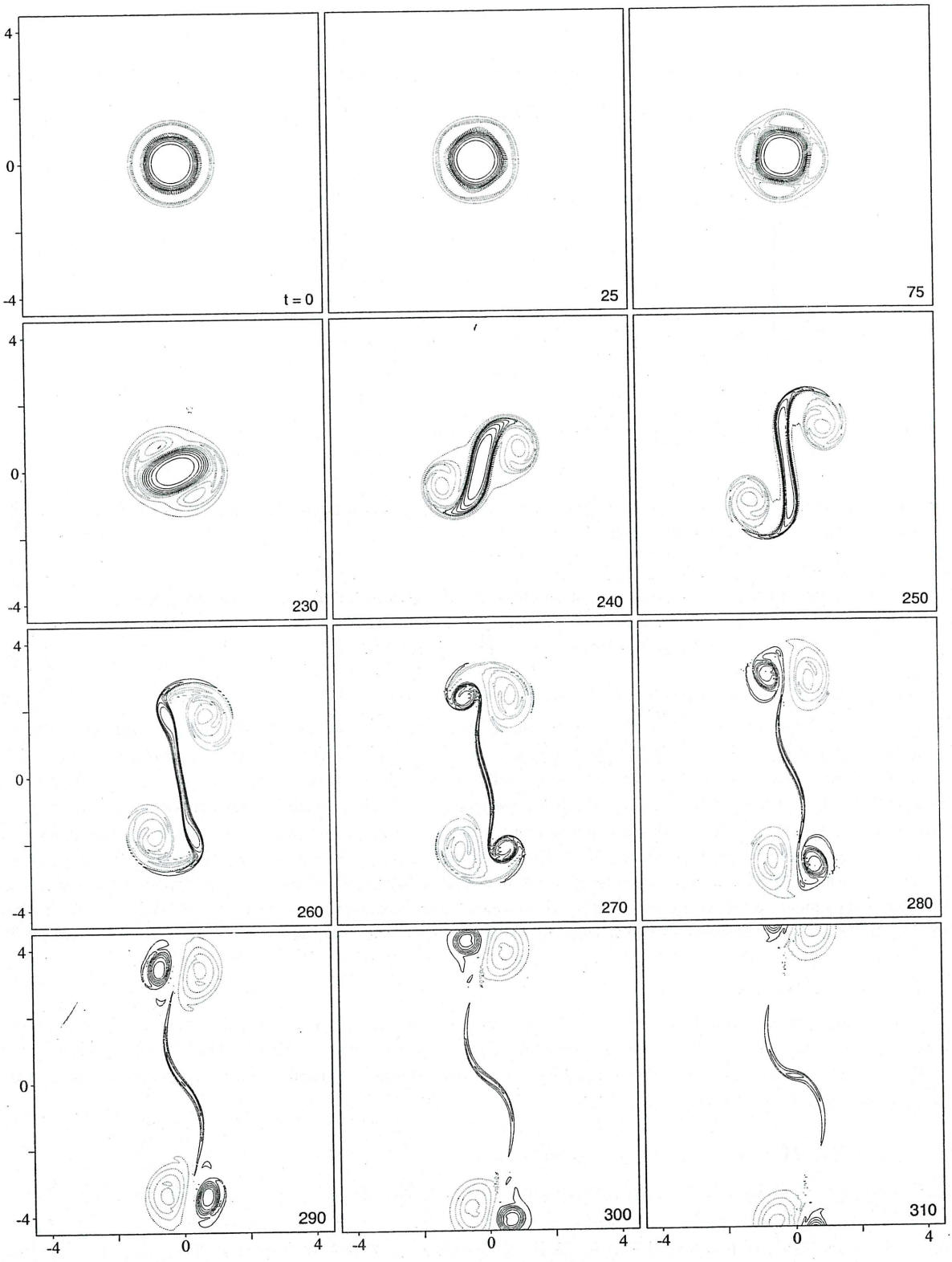


Figure 1: Vorticity contours in a numerical simulation of the evolution of $\omega_{\alpha=7}$, initially perturbed with a $w'$ given by equation 2, where $k' = 4$, $\mu = 0.05$, $\sigma = 0.5$. The minimum contour is $\omega_{min} = -0.5186$, and all contour intervals are $\Delta\omega = 0.1572$. Dashed contours indicate negative values of $\omega$. For this simulation, $N_r = 256$, $N_\theta = 512$, $L = 1.2$, $\nu = 5 \times 10^{-5}$ The timestep used is $\Delta t = 0.01$ $t < 232$, and $\Delta t = 0.005$ $t \geq 232$

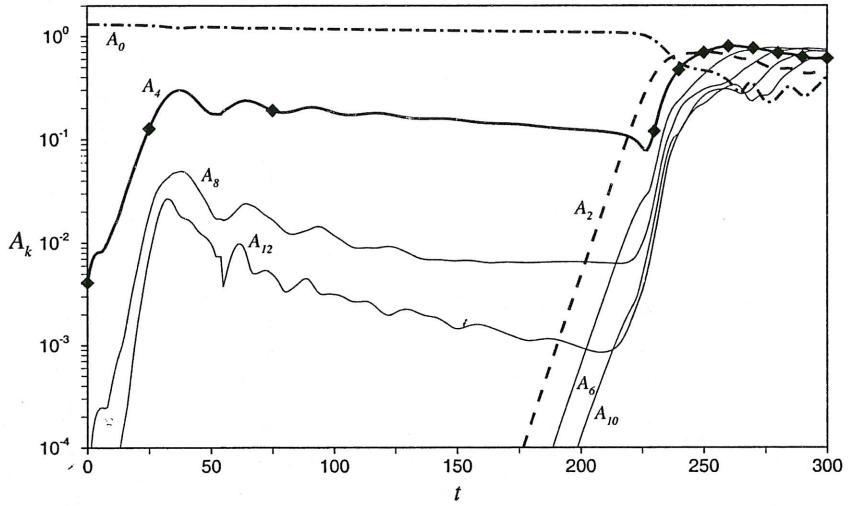


Figure 2: Evolution of the amplitudes of various azimuthal components $A_k$, given by Eq. 10. Black diamonds indicate the sucessive times at which the vorticity distributions were shown in figure 1.

A convenient measure for the amplitude of the Fourier coefficients $\hat{\omega}_k$ from Eq. (8) at any given time is

$$A_k(t) = Q_k^{1/2} = \left( \int_0^{2\pi} \int_0^{\infty} \omega_k^2(r,\theta,t) r \mathrm{d}r \mathrm{d}\theta \right)^{1/2} \tag{10}$$

where $Q_k$ is the azimuthal enstrophy associated with the wavenumber $k$.

Figure 2 shows the evolution of $A_k(t)$ in log-linear coordinates for various even azimuthal wavenumbers in the dipole formation of figure 1. A similar graph was shown by Kloosterziel & Carnevale (1999). After a brief transient (different in shape to that of Kloosterziel & Carnevale (1999)), there is a period of linear growth of the most unstable mode $k = 4$ and its harmonics, which are associated with the square vortex formation. The amplitudes of these modes peak around $t = 30$, and subsequently slowly decay. However, $A_2$ and its harmonics appear at $t = 175$, and continue to grow so that by $t = 220$, $A_2$ is equal in amplitude to $A_4$. At this time the vortex core is no longer square. The $k = 2$ mode continues to grow, and at $t = 230$, there is a rapid increase in the amplitudes of all the even modes. However, the axisymmetric mode $A_0$ decreases in amplitude. These changes in amplitude are associated with the merging of the satellites, the stretching of the core and subsequent dipole splitting.

## 4. CONCLUSION

Using an infinite radial domain Navier-Stokes code, we have performed a numerical study of the behaviour of an isolated circular vortex, subject to an azimuthal mode 4 perturbation. We find that there are two distinct instabilities, namely square vortex formation and subsequent dipole splitting. Hence the square vortex is not a stable compound vortex.

## 5. REFERENCES


BUNTINE, J.D. & PULLIN, D.I. "Merger and cancellation of strained vortices", *J. Fluid Mech.*, **205**, 263-295, 1989.

CARNEVALE, G.F. & KLOOSTERZEIL, R.C. "Emergence and Evolution of triangular vortices", *J. Fluid Mech.*, **259**, 305-331, 1994.

CARTON, X.J., FLIERL, G.R. & POLVANI, L.M. "The generation of tripoles from unstable axisymmetric isolated vortex structures", *Europhys. Lett.*, **9**, 339-344, 1989.

DRAZIN, P.G. & REID, W.H. *Hydrodynamic Stability.* Cambridge University Press 1981.

KLOOSTERZIEL, R.C. & CARNEVALE, G.F. "On the evolution and saturation of instabilities of two-dimensional isolated circular vortices", *J. Fluid Mech.*, **388**, 217-257, 1999.

ROBINSON, A.C. & SAFFMAN, P.G. "Stability and structure of stretched vortices", *Stud. Appl. Maths*, **70**, 163-181, 1984.

*Melbourne Graduate Fluids Conference, 2001*
*Monash University, Melbourne, Australia*

# CONTROL OF FLOW SEPARATION IN A WATERJET USING EXPERIMENTAL TECHNIQUES

**L. MUNUNGA**

Department of Mechanical Engineering
Monash University, Clayton, Victoria, AUSTRALIA

## ABSTRACT

*Research work undertaken by previous researchers has clearly shown that the boundary layer along the roof of a waterjet intake is likely to separate when the speed of the boat is relatively high. This paper discusses wind tunnel simulation work carried out to control flow separation in a waterjet. Investigations were carried out using vortex generators, boundary layer blowing and a splitter plate to ascertain the extent of flow improvement. Performance changes were related to impeller plane flow improvement. At high medium boat speed with an IVR of 0.55 the results of tests using vortex generators yielded the best Fractional Improvement (F.I.) of about 28%, while in the case of boundary layer blowing an F.I. of 53% was recorded under optimum blowing conditions. The splitter plate design provided a relatively good result with an F.I. of about 46% recorded at IVR of 0.55. It was further noted that in the case of vortex generators their location was very critical; the location of the splitter plate and its size were very important factors to consider for good performance. The optimisation of the blowing gap size and the blowing rate were found to be of utmost importance to achieve good results in the case of boundary layer blowing.*

## 1. INTRODUCTION

Marine vehicles have undergone various phases of technological development over the years. Around the time of the industrial revolution, sailing ships (1830) could travel at 10 knots (1 knot is about 1.85 km/h) while clipper ships (1870) could manage 16 knots (Basin and Latorre, 1997). At the moment, very large catamaran ferries can cruise at 48 knots and by using aerofoil section superstructures designers are aiming at very high-speeds, in the region of 80 knots (Walker et al., 1997). Roy (1994) and Allison (1992) give interesting overviews of the development of waterjet propulsion.

As an alternative to conventional propellers the waterjet propulsion system is currently used on many medium and high-speed craft. Mechanical simplicity, good performance, high fuel efficiency, shallow draft, good manoeuvrability, high safety, low noise and vibrations are some of its key features.

The roof of a waterjet intake (Figure 1) is curved and this curvature subjects the fluid entering the intake section initially to a favourable pressure gradient and then to an adverse pressure gradient. It is known that the boundary layer along the roof of a waterjet intake separates when the boat is running at relatively high-speed, above 35 knots. The size of the separated region grows as the speed of the boat increases. The presence of a non-uniform flow impairs the performance of the impeller, which is designed to handle uniform flow. A reduction in the non-uniformity of flow at the impeller entry plane is expected to bring additional benefits such as minimising the likelihood of cavitation damage to the impeller and reduction, or at best elimination, of vibrations due to unbalanced loading of the impeller.

Most researchers in the area of intake design have been concentrating on intake design based on changing the geometric features using CFD methods (Seil et al., 1997 and Allison, 1997) while the current research has taken a different approach. In this research attention was directed at additional design features to existing intake geometry. Many different methods can be used to control flow separation (Schlichting, 1968). The methods used in this work are: vortex generators, boundary layer blowing, splitter plate and intake screen.

## 2. APPARATUS AND METHOD

The experimental work described in this paper was carried out in the re-circulating aeronautical wind tunnel of the Department of Mechanical Engineering, Canterbury University (New Zealand). The working section of the wind tunnel is 1.2 m wide, 0.9 m high and 2.4 m long. With a typical operating speed of 25 m/s the flow may be considered incompressible. Although the Reynolds number is much smaller when using air as the working fluid, as opposed to water, previous work at the University of Canterbury, by Griffith-Jones (1994), has shown the results to be applicable to the real situation.

Figure 2 shows the schematic arrangement of the experimental apparatus in plan view. An experimental waterjet unit, with a curved duct, was placed on one wall of the working section of the wind tunnel. No impeller was used and the stator section was bored out to just leave the outer casing. A length of pipe was attached to the unit just after the nozzle in order to ensure that at a downstream measuring plane there would be fully developed pipe flow. The results obtained from a rake of pitot tubes at this measuring plane were used with knowledge of the local static pressure to determine the mass flow rate through the intake with an accuracy of better than 5%.

Performance changes were related to the Intake Velocity Ratio (IVR), which is defined as the ratio of the mean velocity at the impeller plane (Vi), and the tunnel main flow velocity ($V_b$), the equivalent of the boat velocity. It is worth noting that low boat speed corresponds to high IVR and *vice versa*. A centrifugal fan was connected to the end of the pipe to assist the flow. The variation of IVRs was achieved by changing the tunnel and fan speeds.

A second rake of pitot tubes was built and placed at the impeller plane to record the extent of flow non-uniformity at this plane. Twenty-six pressure tappings were installed at roughly uniform increments along the roof to measure the pressure variation. The pneumatic tubes from the rakes and the pressure tappings were connected to a scanivalve pressure switch and a pressure transducer. The transducer was connected to an analogue to digital card and computer system, which recorded the data.

The first design modification involved vortex generators, which were placed along the roof of the intake, at two different locations corresponding to what was termed setup 1 and setup 2 (Figure 3). The second modification made use of a boundary layer blowing system, schematically shown in Figure 2, mainly consisting of an annubar, to measure the blowing flow rate, a pressure transducer and a plenum chamber. The boundary layer blowing device made use of tangential slot blowing, in addition an adjustable flap was used to vary the blowing gap. The third design modification consisted of fitting an adjustable splitter plate mechanism (Figure 4). The splitter plate was connected to an extension bar, with provision for translational and angular motions. Experiments were carried out to determine the effect of additional design features on the intake flow distribution, especially at the impeller plane.

# 3. RESULTS AND DISCUSSION

## 3.1 VORTEX GENERATORS

Figure 5 illustrates the impeller plane distribution of the non-dimensional stagnation pressure coefficient, $c_{p0}$. At high medium boat speed with a typical IVR of 0.55, there is a significant degree of flow non-uniformity at the impeller plane, especially for the bare intake. The non-uniformity of flow is reflected by the lower values of stagnation pressure coefficient in the region between the intake roof, r = -1.00 and the centre line, r = 0.00 (horizontal axis). As the boat speed increases to match an IVR of 0.4, the region of lower $c_{p0}$ extends beyond the centre line up to about the middle of the impeller plane bottom half. It can be seen that vortex generators provide a marginal improvement in the flow distribution at the impeller plane compared to the bare intake, however it is still not near the ideal flow distribution ($c_{p0}$ = 1.00 throughout). The region of stagnation pressure deficiency is representative of the size of the separated region. At low boat speed with an IVR of 0.97 experimental results showed that the $c_{p0}$ deficient area was much smaller even for the bare intake situation. It is for this reason that flow separation from the roof is generally not a major problem at low boat speed range.

Results of Figure 5 (IVR=0.55, steup 1) represent a Fractional Improvement (F.I.)* of 27.8% and is better than the improvement recorded for setup 2. At low speed (IVR=0.97, setup 1) the F.I. was 14.5%. In the case of the high boat speed with an IVR of 0.4 vortex generators in the configuration of setup 2 provided better results with a "Fractional Improvement" of 9.5% as opposed to 6.8% for setup 1. Investigations were carried out, by trying to locate the vortex generators in different positions, and ultimately only setups 1 and 2 provided satisfactory results. These results suggest that vortex generators should be correctly positioned for them to be effective. The correct position was found to be just ahead of the separation point for the bare intake.

Figure 6 shows the distribution of the static pressure coefficient ($c_p$) along the "ramp-roof" surface of the waterjet intake. The results reveal information about the onset of separation, which is characterised by the beginning of a "plateau" region along the curve. The longer the length of the plateau the bigger the size of the separated region. Although the downstream movement of the separation point is not quite evident from Figure 6, it is possible to note the induced pressure gradient as a result of the presence of vortex generators along the roof of the waterjet intake. In addition, flow visualisation using cotton tufts revealed marginal downstream movement of the separation point.

## 3.2 BOUNDARY LAYER BLOWING

Figure 7 shows the effects of blowing high momentum fluid into the boundary layer, next to the waterjet intake "ramp-roof", on the quality of flow at the impeller plane, at IVR=0.55. The results of four different blowing rates are compared with those for the "no blowing" situation. For commercial reasons specific values relating to the blowing rate and gap opening are withheld. The general trend exhibited by experimental results was that

---

* *Fractional Improvement (F.I.) is the ratio of the actual improvement in the area weighted overall stagnation pressure coefficient to the value of the improvement that would give an overall stagnation pressure coefficient of 1.0.*

higher blowing rates generated more uniform flow at the impeller plane and also produced a smaller separated flow region. From Figure 7, the bottom curve represents the $c_{p0}$ distribution without blowing. A small amount of blowing generated an F.I. of about 20% (second curve upwards), while an increase in the blowing rate by a factor of 2.5 yielded a corresponding increase in F.I. of 83% (top curve), more than four fold. It is important to note that an increase in blowing rate does not necessarily yield a "proportional" increase in F.I..

It is vital to note that although theoretically it might be tempting to blow as much as possible in order to reduce the stagnation pressure deficiency at the impeller plane, in practice the higher the blowing rate the more the required supply pressure would be. And in real life a high externally supplied pressure would entail additional power or in the case of bleeding, some of the downstream high-pressure fluid would be used thereby reducing the propulsive thrust. With the above limitation in mind, the optimum blowing conditions (blowing rate and gap opening) produced an F.I. of about 53%.

### 3.3 SPLITTER PLATE

Figure 8 shows the stagnation pressure distribution at the impeller plane for an intake fitted with a splitter plate, with the boat operating at an IVR of 0.6. Under the above operating conditions an F.I. of 46% was recorded and a relatively good uniformity of flow at the impeller plane was noted. This performance compares fairly well, although slightly lower, with the optimum results achieved using the boundary layer blowing design. Figure 8 also shows that the stagnation pressure coefficient losses are significantly reduced resulting in the flow condition at the impeller plane to be closer to the ideal situation ($c_{p0}$ = 1.0). Several splitter plates of different sizes were tested at different positions. It was noted that both the size and position of the splitter plate influenced its performance in controlling flow separation. Smaller plates tended to perform better because they produced smaller wake regions. While the boundary layer blowing technique presented some design and manufacturing complexities using a splitter plate method was simpler and cheaper.

A design consisting of a splitter plate and an aerofoil bar screen (Figure 4) was implemented and tested. Generally, experimental results revealed that the combined design generated nearly additive effects to the waterjet intake flow at the impeller entry plane. The results have indicated that this design was practical and viable for real jet boats, especially those involved in high-speed applications.

## 4. CONCLUSION

This paper has shown that it is possible to delay the onset of separation and reduce the size of the separated region along the roof of a waterjet unit using experimental methods. The experimental techniques used in this research employed vortex generators, boundary layer blowing and a splitter plate. The improvement of flow condition at the impeller plane was expressed in terms of Fractional Improvement (F.I.) and the following significant results were noted: at an IVR of 0.55 the best F.I. was approximately 28% for vortex generators, while 53% was recorded using boundary layer blowing technique with optimum blowing conditions. The splitter plate design provided relatively good results with an optimum F.I. of about 46% recorded at an IVR of 0.55. The research revealed that the effectiveness of vortex generators was dependent on their location just before the onset of separation. It was also noted that the size and location of the splitter plate in the intake duct were very critical to its performance. Although the boundary layer blowing technique appears to be the best of the three options, its design complexity tends to limit its scope of application.

## 5. REFERENCES

ALLISON, J.L., "Maritime Waterjet Propulsion", Paper presented before the Chesapeake Section of the Society of Naval Architects and Marine Engineers, 1992.

ALLISON, J.L., "Using CFD to Design Waterjet Inlets", *Mechanical Engineering*, Vol. 119, No.5, p. 82-83, 1997.

BASIN, M.A. and LATORE, R., "Development of High Speed Craft with Aero-Hydrodynamic Support", *Proc. 4th Int. Conf. on FAST '97*, Sydney, Australia, p. 85 – 89, 1997.

CHANG, P.K., Separation of Flow, Pergamon Press, Oxford, 1970.

GRIFFITH-JONES, G.J., "Investigation of Incompressible Flow Through an Intake Duct with Applications to Waterjet Propulsion", PhD Thesis, Department of Mechanical Engineering, University of Canterbury, Christchurch, New Zealand, 1994.

ROY, S.M., "The Evolution of Modern Waterjet Marine Propulsion Unit. *International Symposium on Waterjet Propulsion, Royal Institution of Naval Architects*, 1994.

SCHLICHTING, H., "Boundary Layer Theory", 6th Ed. McGraw Hill, New York, 1968.

SEIL, G.J., FLETCHER, C.A.J. and DOCTORS, L.J., "Optimisation of Waterjet Inlets using Computational Fluid Dynamics (CFD)", *Proc. Fourth Int. Conf. on FAST '97*, Sydney, Australia, p. 59-64, 1997.

WALKER, G.J., FOUNGER, A.H.D., YOUNGES, S.P. AND ROBERTS, T.J. (1997) "Aerodynamics of High Speed Multi-Hull Craft", *Proc. Fourth Int. Conf. on FAST '97*, Sydney, Australia, p. 133 – 137, 1997.

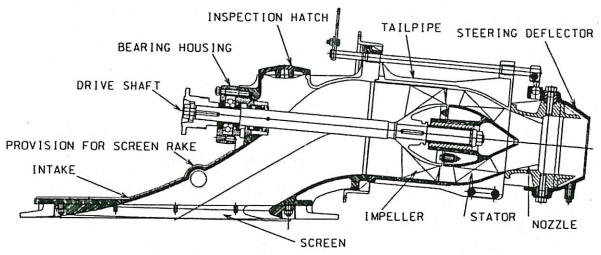


**Fig. 1**: A cross section view of a typical waterjet unit.

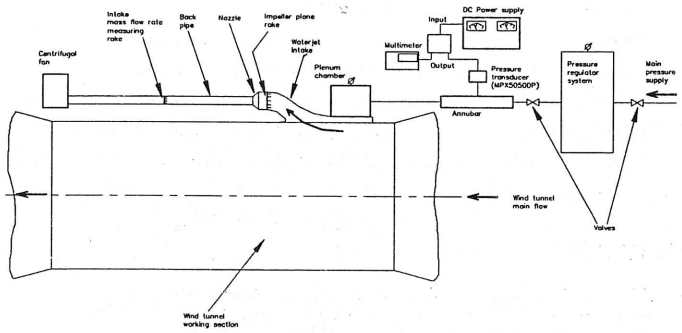


**Fig. 2**: Schematic of the experimental rig with boundary blowing setup.

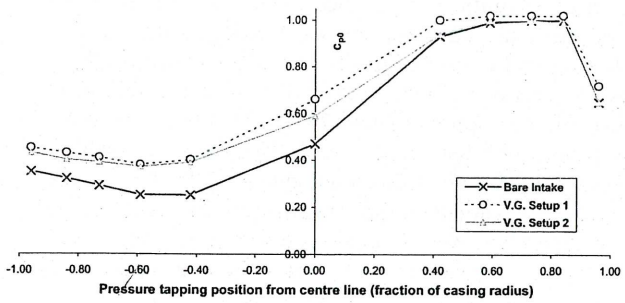


**Fig. 5**: Impeller plane stagnation pressure coefficient distribution at IVR=0.55 for an intake fitted with vortex generators.

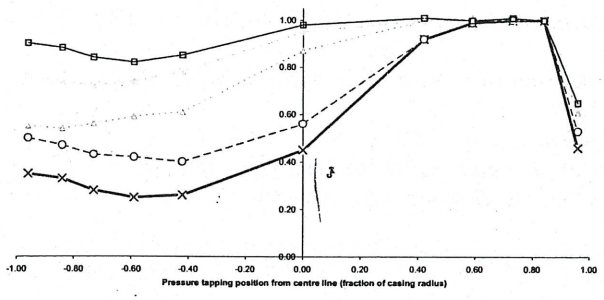


**Fig. 7**: Impeller plane stagnation pressure coefficient distribution at IVR=0.55 for a unit fitted with the boundary layer blowing setup (Bottom curve: No blowing; Top curve: High blowing).

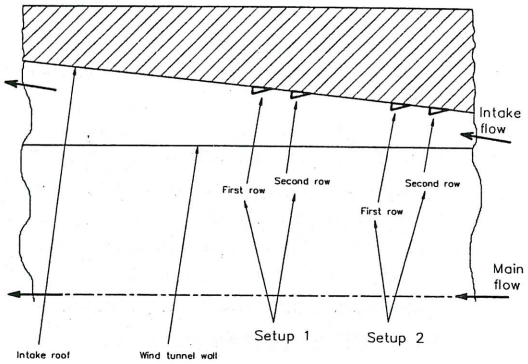


**Fig. 3**: Vortex generators on the "ramp-roof" surface of the waterjet unit.

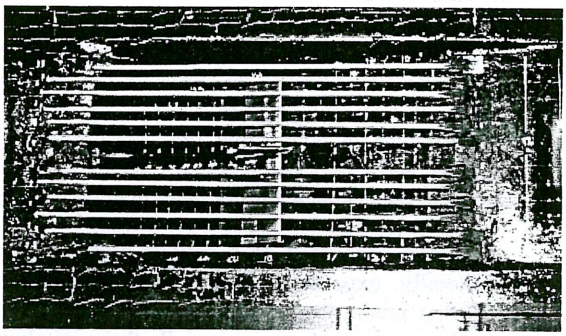

**Fig. 4**: Waterjet unit fitted with a splitter plate and a screen.

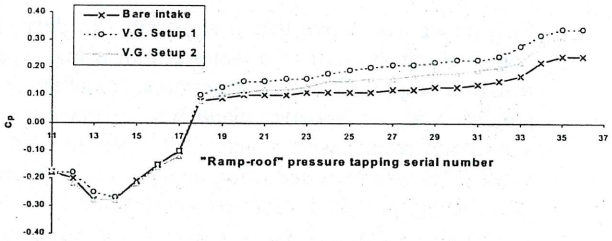


**Fig. 6**: Static pressure coefficient distribution along the "ramp-roof" at IVR=0.55 for an intake fitted with vortex generators.

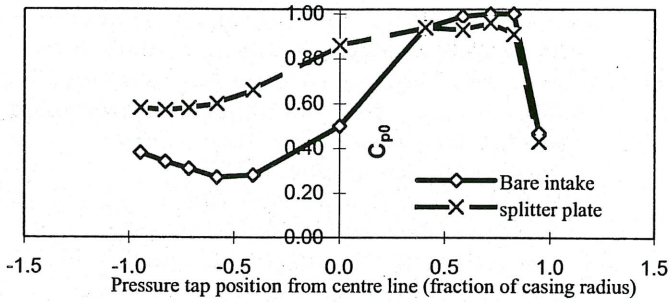


**Fig. 8**: Impeller plane stagnation pressure distribution at IVR=0.6 for an intake fitted with a splitter plate.

*Melbourne Graduate Fluids Conference*
*Monash University, Melbourne, Australia*

# Far field acoustic response of a co-rotating vortex pair

**Keith LIOW, Mark THOMPSON and Kerry HOURIGAN**

Department of Mechanical Engineering
Monash University, Clayton, Victoria, AUSTRALIA

## ABSTRACT

Powell's (1964) acoustic analogy is used to model the far field acoustic response due to the leap frogging motion of a co-rotating vortex pair. A two step approach is adopted where the time dependent incompressible flow is first modelled followed by an aeroacoustic computation of the far field acoustic fluctuations. Numerical results are compared with the analytical solutions from the method of matched asymptotic expansions and direct numerical simulation. It is found to be important to model the initial condition by a ramping function to suppress non-physical acoustic transients.

## 1. INTRODUCTION

Studies of the far field acoustic signature of a compact flow field is of vital importance in efforts to understand subsonic jet noise generation and subsequently to apply active noise control techniques. Several acoustic analogies have been developed to model acoustical fluctuations from low Mach number flows. Lighthill (1952) has proposed an acoustic model with the source derived *a priori* from the fluctuating Reynolds' stresses. Powell's (1964) acoustic model is based on a source region of non-vanishing vorticity. Theoretical investigations of acoustic analogies have often been limited to inviscid point vortices (Powell (1964), Müller and Obermeier (1967), Yates (1978)). The aim of this paper is to present the authors' development of the numerical application of Powell's acoustic model.

### 1.1 FLOW DESCRIPTION

The two vortex cores of equal circulation are initially positioned with a center to center spacing of $2R$. The vortex-induced flow rotates with a co-rotation Mach number $(\omega R)/c$. The Gaussian vorticity distribution of the vortex core is based on Mitchell's *et al.* (1995) paper. Each vortex core has zero radial velocity component. The vorticity and tangential velocity of each core are defined as follows :

$$\zeta = 3.57\frac{U_o}{R_o}\exp(-1.25(\frac{r}{R_o})^2), \tag{1}$$

$$V = (3.57U_oR_o)\frac{1-\exp(-1.25(\frac{r}{R_o})^2)}{1.25r}, \tag{2}$$

where the circulation of the flow is $\Gamma_o = 2\pi U_o R_o/0.7$ and $\omega_i$ is the angular rate of rotation based on the initial velocity field. Figure 1 depicts these distributions as a function of distance.

### 1.2 ACOUSTIC MODEL

Powell's (1964) theory of vortex sound uses the far field pressure, $p$, as the fundamental acoustic variable and defines the source from the Coriolis acceleration, $(\zeta \times \mathbf{V})$.

$$\frac{\partial^2 p}{\partial t^2} - c_o^2\nabla^2 p = \rho_o(\nabla\cdot(\zeta\times\mathbf{V})), \tag{3}$$

where $c_o, \rho_o$ represent ambient values of the acoustic medium.

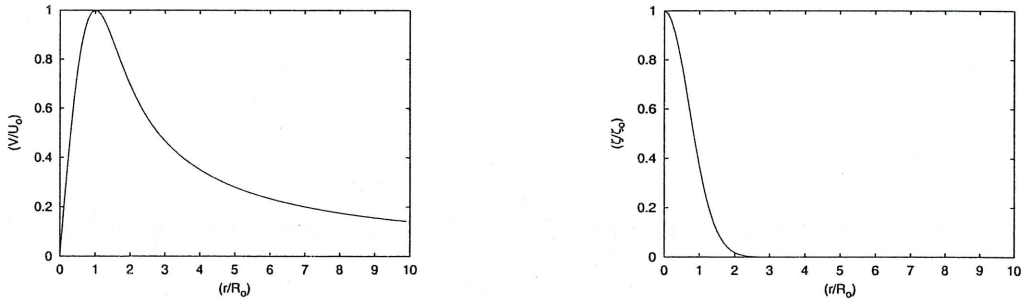


Figure 1: Vortex core tangential velocity and vorticity profile against normalised distance.

Müller and Obermeier (1967) used the method of matched asymptotic expansion (MAE) and derived the analytical far field acoustic solution from a spinning pair of inviscid point vortices. The analytical pressure contours show a double spiral behaviour described by

$$p(r,\theta,t) = -\frac{\rho_o \Gamma^4}{64\pi^3 R_o^4 c_o^2}(J_2(kr)\sin(2\theta - 2\Omega t) + Y_2(kr)\cos(2\theta - 2\Omega t)), \tag{4}$$

where $k$ is the wavenumber, $\Omega$ is the angular rate of rotation for an inviscid co rotating point vortex pair. $J_2$ and $Y_2$ are second order Bessel functions of the first and second kind respectively.

## 2. NUMERICAL METHOD

The two dimensional unsteady incompressible Navier-Stokes equations are solved numerically using a commercial finite volume CFD software package (Fluent Inc.). Spatial convective terms are discretised using QUICK interpolation scheme. The SIMPLE algorithm is used in pressure-velocity coupling. The unsteady flow field is marched in time using a second order accurate implicit time-stepping scheme. The flow is initialised with the velocity field of the co rotating vortex pair. The initial hydrodynamic pressure field is obtained by solving the Poisson equation for pressure. The computational domain, $L_{CFD}$ extends to $30R$ in the $x, y$ directions. At the boundaries, $u, v$ are based on the asymptotic far field solution of the inviscid co rotating vortex pair.

Spatial accuracy of the CFD modelling is studied by monitoring of dissipation of flow vorticity with different values of $(\Delta x_{CFD}/R_o) = 0.125, 0.1428, 0.167$. Temporal resolution studies to minimise numerical damping were also conducted with $\Delta t_{CFD} = 0.4, 0.2, 0.1, 0.05$s.

The aeroacoustic computations are performed using a seven point stencil central difference scheme which is sixth order accurate in space. At the computational aeroacoustic (CAA) boundary, there are three ghost points. On ghost nodes where an axisymmetric stencil is not possible, a non-symmetric stencil was used. Temporal marching is advanced using fourth-order Runge-Kutta scheme. An exponential stretching function was used in the computational (CAA) domain. Non reflecting radiation boundary conditions based on Bayliss and Turkel (1980) are implemented on all the CAA boundaries.

The CAA domain, $L_{CAA}$ extends to two wavelengths in the $x, y$ directions. There are 25 grid points across the vortex core. Outgoing far field acoustic waves were adequately resolved by a minimum of 20 grid points across the entire wavelength. The choice of time step was dictated by the numerical stability of the computational scheme at $(c\Delta t_{CAA}/R) = 0.009167$. Grid stretching is introduced to resolve the near field acoustic source and the far field acoustic waves. An important consideration in grid stretching is the local maximum stretching values. The stretching function adopted was an exponential one. Mitchell *et al.* (1995) has reported on non-physical reflections as the initial acoustic transient traverses through the highly stretched region. The effects of grid stretching on the propagation of acoustic transients were examined with maximum local stretching at 7.4% and 3.99% (see figure 3). Further minimisation of the reflections is performed by adding artificial dissipation ($\mu_a = 0.01$). Excessive damping might be unfavourable and this issue is currently under investigation.

Past researchers modelling acoustic fluctuations from a co rotating vortex pair have indicated the occurence of a high frequency wave component in the far field followed by the progression of the acoustic waves (Lee and Koo (1995), Mitchell *et al.* (1995)). The likely cause is the erroneous initial condition from abrupt spinning of the vortex pair. To model the initial acoustic transients, a ramping function is introduced to artificially create the vortex cores. The vortex cores are ramped from zero circulation to full strength $\Gamma_o$. To achieve asmooth exponential ramping function, the control parameter $(\Delta t_{CAA}/T_{ramp})$ was set to 0.000625.

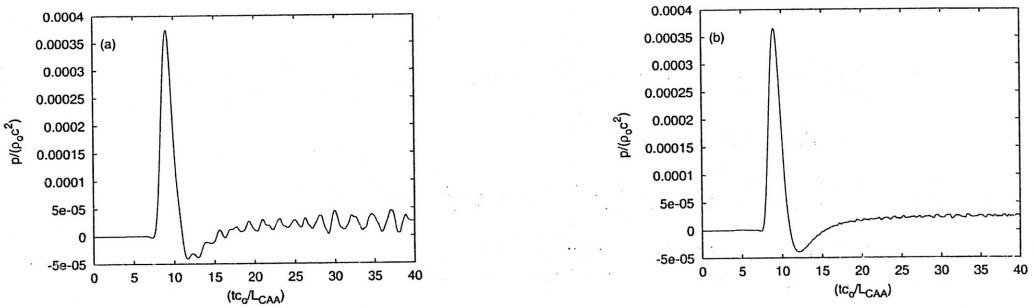


Figure 2: Trace of acoustic pressure during initial acoustic transient with maximum local stretching at 7.3% (2a), 3.9% (2b) with zero dissipation.

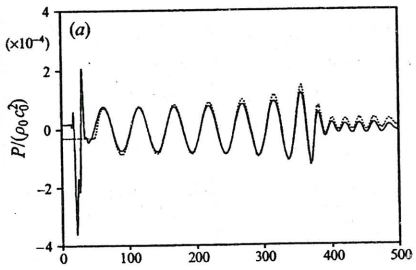


Figure 3: Far field trace of acoustic pressure at $r/\lambda = 2$ along positive x-axis of Mitchell's DNS results.

The hydrodynamic flow variables, $(u, v, \zeta)$ from the CFD domain are exported into the CAA domain using bilinear interpolation. Temporally, cubic spline interpolation was used to obtain intermediate values between the CFD time steps. A resolution study of two, four and six intervals was conducted and consequently no significant increase in accuracy was obtained beyond a six interval cubic spline interpolation.

## 3. RESULTS AND DISCUSSION

Results are presented for the modelling of the flow field and its far field acoustic effects. The Reynolds number of the flow field based on circulation of each vortex is $\mathrm{Re} = \rho_\infty \Gamma/\mu = 7500$. The initial co-rotation Mach number, $M_{cr} = 0.06$.

Four complete co-rotations were evident before eventual merging into a single circular vortex core. The angular velocity was observed to increase as the vortex cores moved closer to conserve angular momentum. The vortex cores 'loses' its initial circular profile and assumes an elliptical shape after the first co rotation. The merging process commences after approximately four half revolutions.

A comparison of two different values of grid stretching is shown in figure 2 where the vortex cores are ramped up and held stationary. The initial acoustic transient was found to generate unphysical reflections as it traverses the CAA domain. Such reflections were found to be grid-induced errors and as such, are classified as numerical noise.

Eight cycles of far field acoustic pressure data were generated from the flow field. A far field observation position is placed at $x = \lambda/2$ along the positive $x$-axis. Temporal evolution of far field acoustic pressure traces are shown in figure 4. Numerical results are compared with Mitchell's DNS results (Figure 3). The initial wave represents the propagation of the acoustic transient and were observed to be less spatially sharp than Mitchell's result. Far field acoustic waves results agree reasonably well in amplitude and oscillation frequency. The acoustic pressure cycles showed a gradual increase in amplitude and angular rate of rotation prior to merging.

The time history of the far field acoustical fluctuations at $x = \lambda/2$ is sampled. The Fourier component of the signal is obtained using a fast Fourier transform algorithm. The power spectral density in dB ($20 \log(p/p_{ref})$) is obtained by squaring both the real and imaginary components of the transform. Power spectral density obtained using the MAE reveals a singular fundamental frequency of the leading quadrupole term (figure 5). Comparison of analytical MAE results with numerical results reveal a higher frequency for the case of viscous co rotating vortex pair. However, acoustic power output agrees reasonably well.

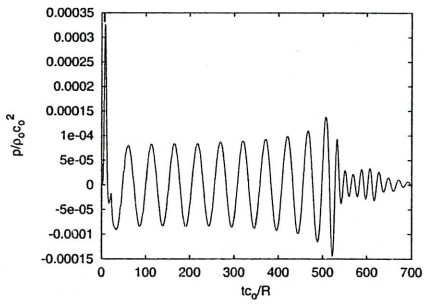


Figure 4: Far field trace of acoustic pressure at $r/\lambda = 2$ along positive x-axis.

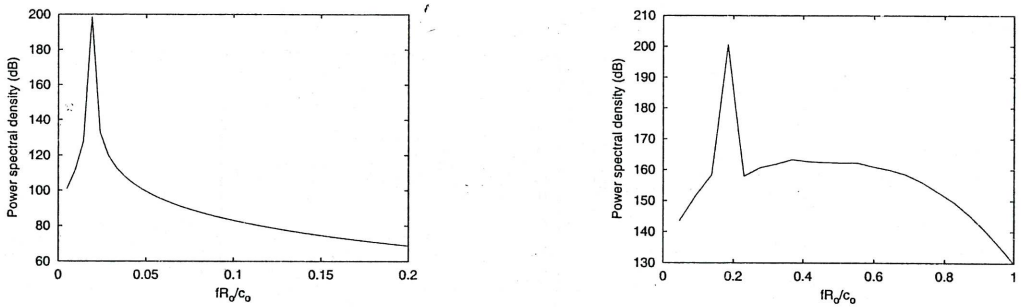


Figure 5: Power spectral density of acoustic pressure at $x = \lambda/2$ along positive $x$ axis using MAE and numerical data. Note $p_{ref} = 2.0$mPa.

## 4. CONCLUSION

The computational coupling of CFD and CAA to solve aeracoustic problems is demonstrated. Accurate modelling of the far field acoustic effects of compact low Mach number flow fields involves appropriate modelling of the initial transient. Numerical parameters such as grid stretching and dissipation or filtering schemes must be optimised in modelling the growth and propagation of acoustic transients. Ongoing studies by the authors on quantifying and controlling the levels of reflections of initial acoustic transients will be published at a later date.

## 5. REFERENCES

BAYLISS, A. and TURKEL, E., "Far field boundary conditions for compressible flows", *J. Comp. Physics,* **48,** 182-199, 1982.

LEE, D.J. and KOO, S.O., "Numerical study of sound generation due to a spinning vortex pair", *AIAA Journal,* **33,** 20-26, 1995.

LIGHTHILL, M.J., "On sound generated aerodynamically", *Proc. R. Soc. Lond.,* **A211,** 564-587, 1952.

MÜLLER, E.A. and OBERMEIER, F., "The spinning vortices as a source of sound", *AGARD,* **CP-22,** 22.1-22.8, 1967.

MITCHELL, B.E., LELE, S.K. and MOIN, P., "Direct computation of the sound from a compressible co-rotating vortex pair", *J. Fluid Mech.,* **285,** 181-202, 1995.

POWELL, A., "Theory of vortex sound", *J. Acoust. Soc. Am.,* **36,** 177-195, 1964.

YATES, J.E., "Application of the Bernoulli enthalpy concept to the study of vortex noise and jet impingement noise", *NASA Contractor Rep.,* **2987,** 1978.

*Melbourne Graduate Fluids Conference, 2001*
*Monash University, Melbourne, Australia*

# KINETIC ENERGY OF SQUARE OBJECTS FALLING UNDERWATER

**H. MARCOLLO and J. HINWOOD.**

Department of Mechanical Engineering
Monash University, Clayton, Victoria, AUSTRALIA

## ABSTRACT

The behaviour of a square object traversing uni-directionally underwater is investigated experimentally. The experiments were conducted up to a Reynolds number of 100,000. The effects of an approaching wall, or the ground, on the velocity and kinetic energy contained in the system are presented. Designers of surface cranage systems involved with lowering submersible packages can make use of the non-dimensional results for a better understanding of the energies involved.

## 1. INTRODUCTION

One of the principle concepts to become familiar with in studies of underwater forces is that of the 'added mass'. The concept attempts to visualise a bounded region of fluid that accelerates with a solid body and adds to the total mass. Strictly, the fluid particles will accelerate at varying degrees, depending on their location relative to the body and hence the added mass represents the integrated effect of these particles throughout the volume. The added mass can vary for different translation directions depending on the shape. Adding to the complexity of the concept are the dynamic effects of separation and vorticity.

Known added mass values for square type shapes in steady relative motion are given in Newman (1980), Kennard (1967) and Flagg et.al.(1971). The methods of potential flow have been used to construct tables in the aforementioned references. For many situations involving elongated bodies the three-dimensional added mass coefficients can be approximated by a strip theory synthesis using the two-dimensional coefficients of simpler forms.

Added mass is often used in stationary elastic oscillating object cases where noticeable changes in natural frequency are assigned to an additional fluid mass. However, the natural frequencies are shifted by a more complicated fluid dynamic effects, often with vortices that result in pressures in phase with the bodies' acceleration. Understanding the fundamentals of these effects with the concept of an added lumped mass proves fruitless. A more appropriate parameter is the kinetic energy, which is presented in this study.

An experimental approach has been adopted in this study in preference to an analytic or numerical method. A full Navier-Stokes computational solution for each case was deemed to require too much computer resource time, while the likelihood of the flow having a considerable amount of vorticity and unknown separation locations creates problems with potential flow solutions.

The current paper makes use of the following dimensionless terms;

$m^*$ = Mass ratio = Mass of body / mass of fluid displaced.

$V^*$ = Dimensionless velocity = Actual velocity / Terminal velocity.

$K^*$ = Dimensionless kinetic energy = Actual kinetic energy / Terminal kinetic energy.

$z^*$ = Dimensionless height from floor = Height above floor / Width of object parallel to plane of floor.

## 2. EXPERIMENTAL METHOD

### *The experimental rig*

A submersible testing rig concept was devised. This would enable faster and easier testing by adjusting the testing parameters above water and then submerging for the experimental run. The rig is shown in Figure 2.1

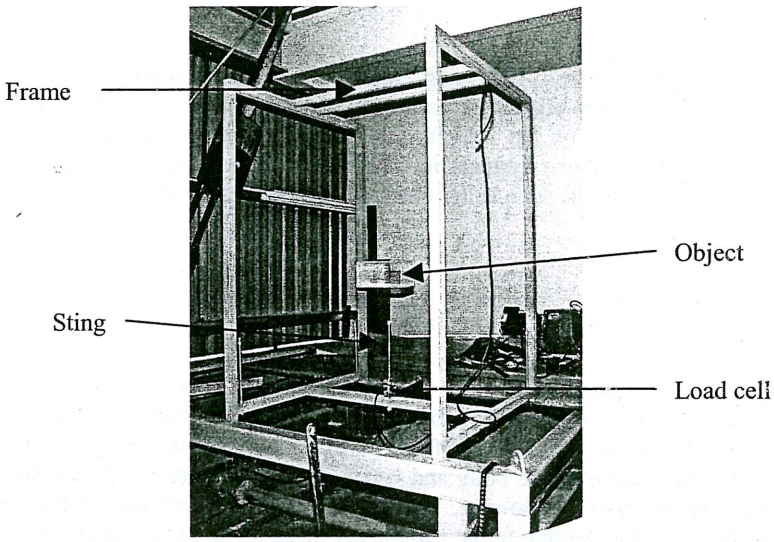


**Figure 2.1 The experimental rig set-up for the added mass tests**

The rig consists of a frame with two vertical wires to guide a falling object. A false floor is then positioned over a sting (steel rod that acts to decelerate the object) and can be set at different heights relative to the top of the sting by the use of threaded rods at each corner. At each side of the object, there is two times the width of the object in clearance to avoid frame interference effects. A rubber tip is installed on top of a sting. The tip acts to slow the object to rest over a distance of about 3mm, rather than several orders of magnitude less for a steel tip, in which case the forces through the load cell and frame would be very large.

An underwater video camera recorded images on a SVHS Video Cassette Recorder. Successive images of the dropped object were observed beside an underwater measuring stick to record terminal velocity.

A commercially available 500lb max rating load cell was waterproofed and connected to a 3V excitation strain bridge. Voltage signals were then logged onto a Pentium I computer with a Data-Translation data acquisition board. The signals were logged through GLOBAL LAB and then post processed through EXCEL.

### *Data Processing Procedure*

The force-time history recording made by the load cell doubles as a displacement-time history due to the load cell and sting acting as a linear spring. One can calculate the impulse of an object decelerated with the measured force-time history by calculating the area under the force-time curve. The maximum deflection of the load cell indicates the elastic energy stored within the load cell, sting and rubber tip on a proportionality basis. If all the elastic energy is assumed to have originally been the kinetic energy of the falling object then it is possible to calculate the total mass of the falling object.

By setting the sting at different distances from an approaching boundary, the velocity, energy, impulse and mass statistics were determined for the falling object as it approached the boundary. The velocity of the object was calculated from the impulse and kinetic energy values, while terminal velocity measurements were observed from the video.

## 3. RESULTS AND DISCUSSION

### *Falling object approaching floor*

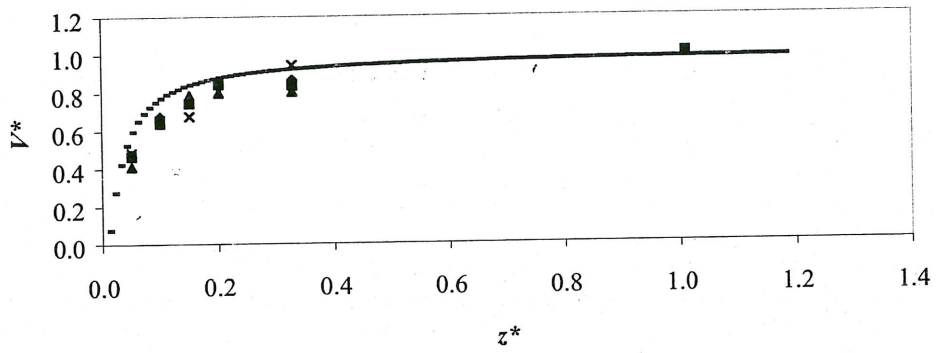


**Figure 3.2 $V^*$ as a function of $z^*$ for a falling 200 x 200 x 100mm object approaching an underwater floor (100mm dimension is normal to the floor). Object mass ratios are ♦ = 1.22, ■ = 1.30, ▲ = 1.45, × = 1.67. Theoretical line, -, is for $m^* = 1.22$.**

Figure 3.2 shows the velocity of an object as it approaches an underwater floor. For each $m^*$, results were obtained from six tests with the sting set at different heights.

A theoretical prediction of the velocity slope has also been presented in figure 3.2. (see Eqn 1).

$$\dot{z} = \dot{z}_o e^{-k/z} \qquad \text{(Eqn 1.)}$$

Where $k = \dfrac{\rho l^4}{32 m_{total}}$, $l$ is the side length of the object, $m_{total}$ is the total associated mass of the object.

The theory is based on the following hypothesis: As the object drops vertically under the influence of gravity, it causes the water in front of it to be ejected horizontally. The energy gain by the horizontally accelerated fluid is equated to the kinetic energy lost by the falling object.

The velocity seems quite well behaved globally as the data collapses reasonably well onto one line when each case is non-dimensionalised with its terminal velocity far away from the floor. The experimental results have some variations at intermediate values which may be a Reynolds number effect. The theory only takes into account the fluid dynamics of the leading edge of the object approaching the wall and not trailing edge effects. Discrepancies between the theory and the experimental results are hence ascribed to trailing edge effects and the dynamics of shedding vortices.

### *Flow visualisation*

Arrays of wool tuffs on wire were positioned vertically in the water adjacent to the path of the falling object. Another set of wool tuffs was positioned on top of the moving object on stiff wires to study the trailing edge effects. Flow patterns revealed that as the object decelerates near the floor, a narrow jet of the trailing wake shoots out from just above the trailing edge. Also observed was that still water, initially to the side of the object, is firstly accelerated away from the object as the leading edge approaches, then sucked back into the far wake after the trailing edge passes.

The trailing wake escaping as a narrow jet upon deceleration of the object is a characteristic that would be important enough to cause the theoretical prediction to differ from the experimental results.

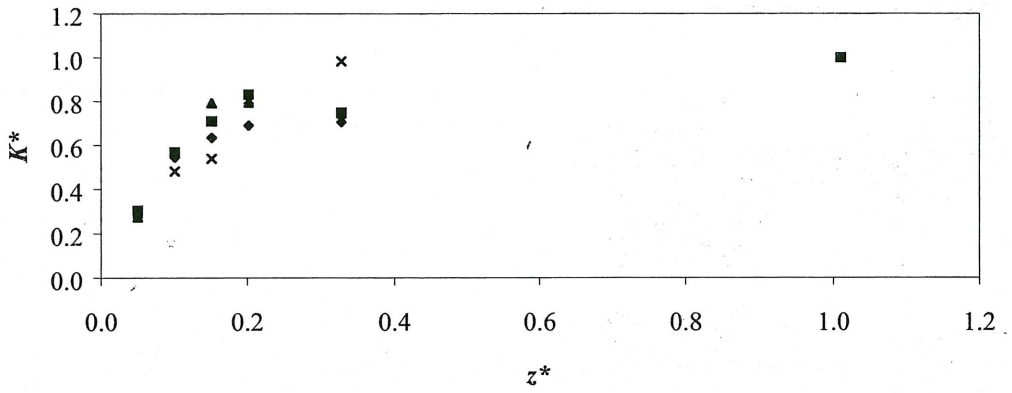


**Figure 3.3 $K^*$ as a function of $z^*$ for a falling 200 x 200 x 100mm object approaching an underwater floor (100mm dimension is normal to the floor). Object mass ratios are ♦ = 1.22, ■ = 1.30, ▲ = 1.45, × = 1.67.**

Figure 3.3 shows the behaviour of the kinetic energy of an object as it approaches an underwater floor. The dimensionless energy appears predictable for high and low values above the floor. At intermediate heights, where the floor is beginning to have a deceleration effect on the object, the behaviour appears to be more complex. As kinetic energy is proportional to velocity squared, the apparent larger variations in energy than velocity, can be attributed to the velocity squared effect.

Understanding the behaviour at intermediate ranges may not be necessary for Engineers. Designing for stresses during sub-sea mating operations or collisions should only require the close proximity data.

## CONCLUSION

We have seen that by using a sting and measuring the impulse, load cell extension and velocity of an underwater falling object, instantaneous mass and kinetic energy can be calculated.

When an object approaches an underwater floor and a deceleration effect takes place, the velocity and kinetic energy of the system is predictable in the early and late stages of deceleration ($z^* < 0.1$, $z^* > 1.0$). Simple flow visualisation was performed to discover any effects in the intermediate range of $z^*$ so as to be able to explain the difference between the theoretical prediction and the experimental results. An effect was discovered in which the trailing wake escapes in a narrow jet just above the trailing edge. Further detailed flow visualisation or computational techniques would be required to fully reveal the characteristics of the phenomenon and explain its effects on the falling object.

REFERENCES

FLAGG, C..N., NEWMAN, J.N. "Sway Added-Mass Coefficients for Rectangular Profiles in Shallow Water", *Journal of Ship Research*, p.257, December, 1971.

NEWMAN, J.N. Marine Hydrodynamics, Third Print,. The MIT Press, Cambridge, Massachusetts. 1980.

KENNARD, E.H. "Irrotational flow of frictionless fluids, mostly of invariable density." *David Taylor Model Basin Report* 2229. 1967.

*Melbourne Graduate Fluids Conference, 2001*
*Monash University, Melbourne, Australia*

# A COMPUTATIONAL APPROACH TO BICYCLE HELMET VENTILATION DESIGN

**A.J. Ellis, I.S. Wong, A.F. Bertolini and L.A. Thompson**

Department of Aerospace Engineering

RMIT University, GPO Box 2476V, Melbourne 3001, Australia

## ABSTRACT

In bicycle helmets today ventilation is seen as a key to market success of the helmet with a trend to more ventilation openings. Unfortunately these holes come at the detriment to the safety and structural integrity of the helmet. Currently some optimisation occurs in helmet ventilation design by manufacturers, however, it involves an iterative manufacturing process—making prototypes and testing them. This paper presents, to the best knowledge of the author, the first published attempt to incorporate computational fluid dynamics (CFD) into bicycle helmet ventilation modelling and prototyping where the helmet's ventilation is theoretically modelled before manufacture and experimental testing.

## 1. INTRODUCTION

Today most bicycle helmets sold are called soft-shell helmets. They consist of a plastic liner that helps spread the area of impact and hold the helmet together for repeat impacts. The expanded polystyrene (EPS) liner crushes slowly to keep the deceleration down and lengthen the impact time.

Unfortunately EPS foam is also a very effective insulator with a thermal conductivity, k of around 0.030 $Wm^{-1}K^{-1}$ (Incropera and De Witt, 1990). To try and keep the head cool in modern helmets manufacturers make holes or vents in the EPS foam liner and plastic shell. The primary mode of cooling then is by convection, or by cool air moving over the head while cycling.

Ventilation is of increasing marketing focus by helmet manufacturers yet there exists very little published scientific research on the subject. The emphasis on the number of ventilation openings in helmets is a disturbing development as ventilation holes detract from the impact protection and structural integrity of the helmet.

While there has been work performed on the ventilation and comfort of helmets, there has to date been no published attempts at optimising helmet ventilation using the CFD method. It may be advantageous to helmet manufacturers if they can incorporate CFD into the design loop to reduce prototype manufacturing and testing costs.

## 2. METHODS

In order to produce a CFD model it was first necessary to produce a three-dimensional geometry. The basic helmet geometry was taken from an existing helmet design that was chosen as a starting point for its relatively simple design. The points on the surface of the helmet were digitised using a robotic arm digitiser. The head-form points used were those of the standard head-form 'E' from the Australian Standard for pedal-cycle helmet testing AS2512.

Once the points had been entered they were made into surfaces using the module Fastsurf™ in the CAD software package CADKEY™. The surfaces were made into solids using boolean operations in CADKEY™. The solid helmet and head-form files were unioned together and converted into an ACIS file. This ACIS file was then imported into the well-known CFD software Fluent™'s geometry pre-processor GAMBIT™.

In GAMBIT™ the helmeted head-form solid was surrounded by a control volume or solution region. The dimensions of the solution region (1320mm wide by 1070 mm high by 2100 mm long) approximate that of the working section of the large subsonic wind tunnel at RMIT Aerospace Engineering in Melbourne where any experimental validation will take place.

Once the helmeted head-form and control volume were meshed the boundary conditions were inputted. Use of symmetry was made to split the control volume in half through the middle of the helmeted head-form. The entrance to the control volume was set as a velocity inlet and the exit as an outflow.

This means that only the inlet velocity vectors need to be inputted. The outflow boundary condition means that the outlet velocity conditions are calculated from the upstream conditions. From there the file was ready to import into Fluent™ for analysis. Figure 1 below shows a schematic of the model preparation procedure.

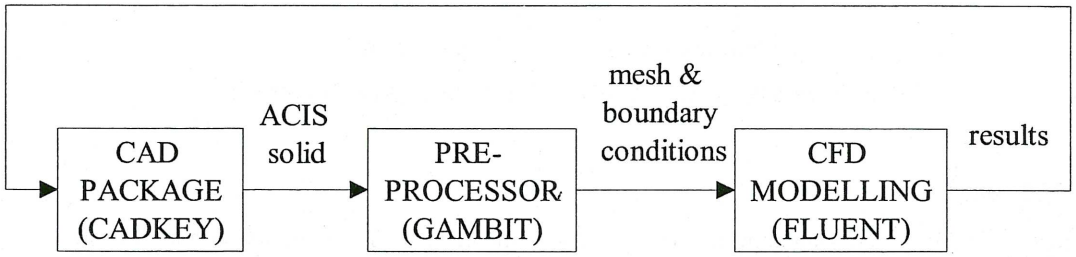


**Figure 1** : Schematic diagram showing geometry preparation procedure

## 3. PROBLEM FORMULATION

The basis of this investigation is to investigate the theory for optimal placement and design of the ventilation openings of bicycle helmets. To do this consider Bernoulli's equation for an incompressible fluid moving along a streamline:

$$p_s + \frac{1}{2}\rho_{air}V^2 + \rho_{air}gz = \text{constant} \tag{1}$$

The consequence of Bernoulli's equation is that for air to move over the head, the helmet inlet holes should be placed at a region of relative high static pressure compared to the ventilation outlet holes, which should be placed at regions of low static pressure. In effect air is accelerated over the head provided the air has freedom to move over the head and is not impeded. What this means to the helmet designer is that the interior of the helmet should have internal channels to allow the air to flow from the high-pressure region at the inlet to the low-pressure regions at the outlet. For the CFD work to be useful to helmet manufacturers, a distribution of pressures on the helmet surface need to be determined.

Since the primary mode of heat transfer from the helmeted-head will be via convection, this will be governed by equation 2 below.

$$q = \bar{h}A_s(T_s - T_\infty) \tag{2}$$

From equation 2 above it can be seen that the heat transfer will depend on the temperature difference of the ambient air flowing over the head and the surface temperature of the head. It will also depend on the product of the surface area of the head exposed to convection and the average heat transfer coefficient which depends on the flow conditions.

To model the flow conditions over the helmet in Fluent™ the 3D Reynolds-averaged Navier-Stokes equations given below in equations 3 and 4 are used.

$$\frac{\partial \rho}{\partial t} + \frac{\partial}{\partial x_i}(\rho u_i) = 0 \tag{3}$$

$$\rho\frac{Du_i}{Dt} = -\frac{\partial p}{\partial x_i} + \frac{\partial}{\partial x_j}\left[\mu\left(\frac{\partial u_i}{\partial x_j} + \frac{\partial u_j}{\partial x_i} - \frac{2}{3}\delta_{ij}\frac{\partial u_l}{\partial x_l}\right)\right] + \frac{\partial}{\partial x_j}(-\rho\overline{u_i' u_j'}) \tag{4}$$

Although in reality the flow is unsteady, in this simulation it is simplified and assumed to be steady, which negates the use of the time derivative terms in the above equations.

To model the turbulence effects in the above equations, the standard k-ε model was chosen incorporating standard wall functions.

The flow and turbulence equations are solved by finite volume methods. The solution region was meshed in this example using tetrahedral elements. By meshing the faces of the helmeted head-form with triangular elements of a closer spacing than those of the tetrahedral elements of the solution region, good mesh refinement was seen near the surface of the helmeted head-form. Overall there were 366 534 tetrahedral volume elements compromising the unstructured mesh of the solution region.

A segregated solver was used in this simulation with an implicit solution formulation technique. The eddy or turbulent viscosity is solved from equation 5 below. The model constants used have the following default values: $C_{1\varepsilon} = 1.44$, $C_{2\varepsilon} = 1.92$, $C_\mu = 0.09$, $\sigma_k = 1.0$, and $\sigma_\varepsilon = 1.3$

$$\mu_t = \rho C_\mu \frac{k^2}{\varepsilon} \tag{5}$$

Boundary conditions at the velocity inlet were specified as velocity vectors normal to the solution region inlet wall in the x-direction. This velocity (u) is substituted into equation 6 below, which gives the Reynolds number of the flow. For this simulation a value of the inlet velocity of 10 $ms^{-1}$ is used. In this equation, L is based on the diameter of a cylinder of approximately the same size as the maximum cross-sectional length of the standard head-form 'E' from the Australian Standard for pedal-cycle helmet testing AS2512. The value used here is 172 mm.

$$\mathrm{Re} = \frac{\rho u L}{\mu} \tag{6}$$

Initial conditions for k and ε were specified via turbulence intensity and length scale. The turbulence intensity is defined as the ratio of the root-mean-square of the velocity fluctuations to the mean flow velocity. Here a modest estimate of 2% is used. The turbulent length scale is a physical quantity related to the size of the large eddies that contain energy in the turbulent flow. As a guide it is recommended that this value be derived from the characteristic length of the obstruction to the flow. Since this is the head-form in this case, like in the calculation of the Reynolds Number, 172 mm is used.

Because of the non-linearity of the equations solved, Fluent™ employs under relaxation factors, which limit the changes produced in the scalar variables with each iteration. In this analysis default under-relaxation factors were used as solution controls with those for pressure = 0.3, momentum = 0.7, turbulence kinetic energy = 0.8 and turbulence dissipation rate = 0.8.

The convergence criterion used for modelling all residuals was 0.001 with approximately 160 iterations required to achieve this condition.

## 4. RESULTS

Figure 2 shows a plot of the static pressure coefficient over the helmeted head-form. As can be seen this method could be useful for helmet designers to visualize effects of design changes on the pressure distribution on the helmet.

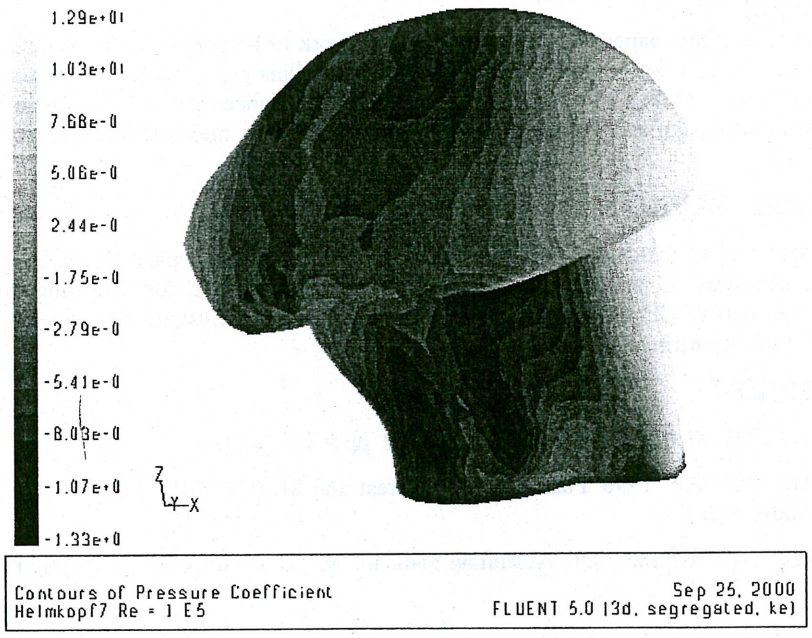


**Figure 2** : Contour plot of the static pressure coefficient

From what was described in the problem formulation section ventilation openings should be placed at areas of high pressure, while ventilation outlet holes should be placed at areas of minimum pressure. The effect of the ventilation openings on the pressure distribution of the helmeted head-form is yet to be modelled.

## 5. FURTHER WORKS

This is the first time that CFD has been used to model the pressure distribution around a helmeted-head. It is hoped that in the future this method can be developed to the point where it can be used to design and optimise the placement of ventilation openings of reasonably complex bicycle helmet designs.

The model of the head used in this simulation is a simplified one, without any of the normal facial features such as eyes, nose and ears. A model including these features could also be made although work so far performed indicates that meshing difficulties can be encountered with complex geometries and care needs to be taken. The best approach certainly seems to be to gradually build up model complexity.

The effect of different modelling conditions has not been discussed in this work. A discussion of the effect on results with refinement of mesh density and computation with different turbulence models has not been undertaken. This could be performed some time in the near future.

Before this can be achieved a C.F.D. model must be validated using simple geometry as described here. To do this it is planned that the simple helmet design modelled here in Fluent™ be produced using stereolithography techniques and placed in the wind tunnel to test. The helmet and head-form should then be pressure-tapped and the pressure coefficients derived from Fluent™ compared to those obtained in the wind tunnel.

Work presented in this paper is for external flow. However, in reality helmet ventilation involves external flow over the helmet and internal flow through the ventilation openings and over the head. An extension of this work would be to try and model this internal flow. Before meaningful results could be obtained however, accurate velocity inlet conditions would have to be ascertained by wind tunnel testing.

It is a foreseeable extension to this work that the drag coefficient is accurately obtained for aerodynamic sports helmet design. Simulations performed so far on the drag coefficient of spheres using the simulation described in this paper obtain poor results. This is likely due to the tetrahedral elements not modelling the boundary layer accurately. A boundary layer mesh could be investigated to obtain better drag coefficient results.

## 6. CONCLUSIONS

As has been discussed in this paper there is still significant work to be performed in the area of CFD modelling for bicycle helmet design and optimisation. However, this paper readily shows some of the possibilities for the future. With further work and computational advances it is not unrealistic to expect that CFD be used in the design and optimisation loop somewhere at the high end of the bicycle-helmet market.

## 7. ACKNOWLEDGMENTS

Andrew Ellis would like to thank RMIT University's Department of Aerospace Engineering for the financial support necessary to perform this research. Also to be thanked for supplying invaluable advice on various aspects of CFD modelling is Niall O'Shea from BAE Systems and Howard Connell from the Mathematics Department of RMIT University.

## 8. REFERENCES

Fluent Incorporated 1998, FLUENT 5 User's Guide, vol. 2. pp 9-1 to 9-28.

Incropera, F.P., De Witt, D.P. 1990 'Fundamentals of Heat and Mass Transfer', John Wiley & Sons, Inc., 3rd ed., appendix A10.

Standards Association of Australia 1996, Australian Standard AS2512.1 'Methods of Testing Protective Helmets', p. 14.

*Melbourne Graduate Fluids Conference, 2001*
*Monash University, Melbourne, Australia*

# Stability of Wake Flows from Elongated Bluff Bodies

**Kris Ryan, M C Thompson and K Hourigan**

Department of Mechanical Engineering
Monash University, Clayton, Victoria, AUSTRALIA

## ABSTRACT

The results from *Floquet stability analysis* of the flow around nominally two-dimensional long plates with elliptical leading edges and blunt trailing edges are presented, elucidating the early stages of wake transition to turbulent flow. Three modes of instability are found: Mode A, Mode B and Mode S. The first two of these also occur in wake transition for circular cylinders and square cross-sectioned cylinders. For sufficiently large aspect ratio, Mode S is found to be the dominant instability mode. This research indicates the generic turbulence transition scenario suggested for circular two-dimensional bodies does not apply to all two-dimensional bluff bodies.

## 1. INTRODUCTION

The generation of streamwise vortex structures in the wake of a nominally two-dimensional bluff body has been the subject of intense study and debate over the past fifty years [Roshko 1955, Gerrard 1966, Williamson 1996]. Over the last 20 years, progress in numerical and experimental technology has allowed researchers to accurately map both the parameter space governing the inception of these streamwise wake vortices and to explore the general geometry and dynamics of these streamwise wake vortices [Williamson 1996, Barkley and Henderson 1996, Henderson 1997]. It is generally accepted that the inception of streamwise vortex structures in the wake is the first step in the progression to a fully turbulent wake. Indeed, the overall wake structures observed in flow fields of relatively low Reynolds number have been shown to persist in flow fields having much higher Reynolds numbers [Williamson 1996]. Research on this topic has been inspired largely in an attempt to discover underlying features leading to fully turbulent flow and therefore to define progressively more accurate models to describe turbulent flow fields.

In an experimental study, Williamson (1996) identified 2 discontinuous alterations of the flow field in the wake of a circular cylinder as the flow changes from a two- to three-dimensional state. These changes consist of a periodic distortion of the Karman vortex-street in the cylinder spanwise direction and the generation of streamwise vortex structures in the wake of the flow field. These instabilities, referred to as Mode A and Mode B, occur successively with increasing Reynolds number and may be identified by a discontinuous jump in the Strouhal number as the Reynolds number is increased [Williamson 1988]. The Mode A instability may be identified by a spanwise periodicity of 3-4 cylinder diameters of the Karman vortex-street and the generation of streamwise vortex structures, formed between successive primary cores. Williamson (1996) observed that the Mode A instability existed within the Reynolds number range Re = 180 – 250; he found the critical Reynolds number of inception varies between 180-194 due to the hysteretic nature of the mode. In a Reynolds number range 230 to 250 Williamson observed that a new instability (Mode B) replaces Mode A as the dominant spanwise instability. The Mode B instability has a spanwise periodicity of around 1 cylinder diameter wavelength, which does not appear to vary appreciably with increasing Reynolds number. Williamson's (1988, 1996) observations have been verified numerically by a number of authors. Thompson et al. (1994, 1996) conducted (DNS) computational studies of the flow around a circular cylinder using a three-dimensional flow field. Their work verified the existence of both Mode A and Mode B. Barkley and Henderson (1996) conducted a Floquet analysis of the flow around a circular cylinder, verifying both the critical Reynolds number of inception of the spanwise wavelength of Mode A, and the spanwise wavelength of Mode B. The results have also been experimentally verified by Zhang et al. (1995).

An underlying assumption has been held that the instability modes identified in the wake of a circular cylinder would be exhibited in a bluff body of more general geometry. Little literature exists to verify this assumption. Zhang et al. (1995) experimentally discovered the existence of a "Mode C" instability in the wake of a circular cylinder when a tripwire was placed adjacent to a circular cylinder in a direction transverse to the fluid flow. The Mode C instability was found to have a spanwise wavelength of 1.8 cylinder diameters, and was found to occur when the trip wire was located within 1 diameter of the cylinder. Their results indicate that the suppression of the flow field near the boundary layer results in a Mode C instability to occur in preference to Mode A and Mode B. Numerical calculations performed by Zhang et al. (1995) verified their experimental observations. While their results were corroborated by the numerical Floquet analysis described by Noack et al. (1993 and 1994), who found the three-dimensional instability had a wavelength of 1.8 – 2 cylinder diameters, it now appears that this may have been due to insufficient numerical resolution. (As mentioned previously, the better resolved studies of Barkley and Henderson (1996) give wavelengths consistent with the experimentally measured values.)

Robichaux et al. (1999) discovered the existence of a third mode of instability in their Floquet analysis of the flow field around a square cross-section cylinder. While many physical features of this instability mode corresponded to Zhang's experimental work, Robichaux et al. referred to this instability as a "Mode S" instability in favor of a Mode C instability as their work did not require the existence of a trip wire. Indeed, their analysis found that the Mode S instability may not manifest because of the prior occurrence of the Mode A instability altering the base flow. Owing to the geometry of their model, it is possible that vortex shedding from the leading edge of the square cylinder interferes with the trailing-edge boundary layer and subsequently with the wake flow field, causing the Mode S instability to exist (but not dominate the flow field). However, their parameter space was limited to a Reynolds number range of ($150 < Re < 225$), and only for a square cross section cylinder; Mode S may become the dominant three-dimensional instability at higher Reynolds numbers. Previous research has not adequately answered whether the

results obtained from the circular cylinder describe all three-dimensional modes observed for two-dimensional bluff bodies of general geometry?

This numerical investigation aims to observe the instability modes in the wake of a blunt plate of varying aspect ratio in order to determine if Mode A and Mode B are the dominant instabilities for a variety of geometries.

## 2. NUMERICAL METHOD

The bluff body geometry under investigation consists of a flat plate of finite thickness ($H$) and finite chord ($C$). Several different plates of varying aspect ratio $AR = C/H$ have been investigated. In each investigation the plate is immersed within a uniform flow field travelling in the $x$ direction with constant velocity $U$. The fluid is considered to be a homogeneous incompressible Newtonian fluid. The leading edge has a streamlined elliptical profile. This profile prevents vortex shedding from the leading edge and thus allows the behaviour of the wake transition to be studied in isolation. Parameters describing the geometry of the leading edge are kept constant between plates. The trailing edges of the plates are blunt, thus providing a predetermined location from which trailing vortices are generated, and therefore simplifying post-processing analysis. An image of the plate geometry is given below (Figure 1):

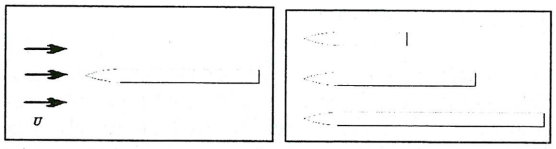


**Figure 1**: Left: Schematic diagram of experimental set-up; Right: Relative aspect ratios of plates.

A Floquet stability analysis is used to determine the most unstable spanwise instability mode(s) as a function of Reynolds number. Floquet stability analysis effectively investigates the stability of a two-dimensional periodic *base flow* to three-dimensional spanwise disturbances by determining from the linearised Navier-Stokes equations whether an assumed sinusoidal spanwise disturbance will grow from one base flow period to the next.

Owing to the requirement of a known two dimensional periodic base flow field, the modeling is performed in two stages; initially a two-dimensional Galerkin spectral-element code is used to determine a periodic base flow field solution (in the form of a Karman vortex street). In the second stage the (linearized) spectral-element method is used to determine instabilities in the third (spanwise) dimension. Details of the Galerkin spectral-element code may be found in Thompson et al. (1996). A detailed description of the Floquet analysis methodology may be found in Ioos and Joseph (1990).

For each plate, the parameter space consists of two variables. These are the Reynolds number based on the plate thickness ($Re_{Th}$), and the spanwise wavelength applicable to the stability analysis. The Floquet analysis is applied using the following approach. Starting from random perturbation fields for the perturbation velocity components and the perturbation pressure, the linearised Navier-Stokes equations are integrated forward in time. At the end of each period, the perturbation fields are normalised. Using Floquet theory it can be shown that a perturbation field can be expanded in terms of *Floquet modes*, where for any chosen spanwise wavelength, the different modes have different growth/decay rates. Thus by normalizing the perturbation fields at the end of each period, after a long time, effectively only the Floquet mode with the largest growth rate will be left. (All others grow less, or decay more, over a period than this one.) This growth rate can then be determined by calculating the amplitude of the mode at the end of a period relative to the initial amplitude. This is called the Floquet multiplier, $Fl$, and it plays an important roll in determining the stability of the two-dimensional base flow. The Floquet multiplier describes the stability of the two-dimensional flow against the selected spanwise wavelength at the given Reynolds number for the plate aspect ratio of interest. If $|\mu|$ is less than unity, the spanwise wavelength under investigation is stable at the given Reynolds number, and will not be observed experimentally. If $|\mu|$ is greater than unity, the spanwise wavelength under investigation is unstable at the given Reynolds number and should be observed experimentally (since it will grow from background noise). If $|\mu|$ is equal to unity then the Reynolds number under investigation is said to be the critical Reynolds number of inception ($Re_{Cr}$). In experiments, this is the lowest Reynolds number above which the instability will be observed.

## 3. RESULTS AND DISCUSSION

Displayed below (Figure. 2) is a diagram depicting the Floquet multiplier as a function of the Reynolds number and spanwise wavelength for a blunt flat plate with $C/H = 7.5$. Inspection of Figure 2 points to three distinct modes of instability. (The three different local maxima correspond to different instability modes.) Two of these modes correspond to Mode A and Mode B found for the flow field around a circular cylinder. However, a third mode, "Mode S" exists with a spanwise wavelength of around $\lambda = 2Th$. Similarly to the results obtained by Robichaux et al. (1999), the third mode, Mode S, does not become critically unstable. That is, the Floquet analysis predicts that Mode S should not be observed under experimental conditions. The characteristics of Mode S found in the present investigation compare favorably with those described in Robichaux et al (1999); it is therefore believed that the same instability mode occurs for both geometries.

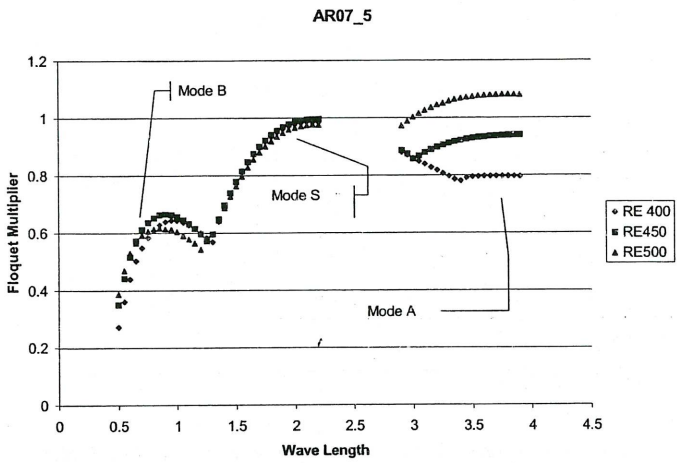


**Figure 2**: Floquet multiplier versus spanwise wavelength for plate $AR = 7.5$

Figure 3, displays the corresponding parameter space for a plate with $AR = 12.5$.

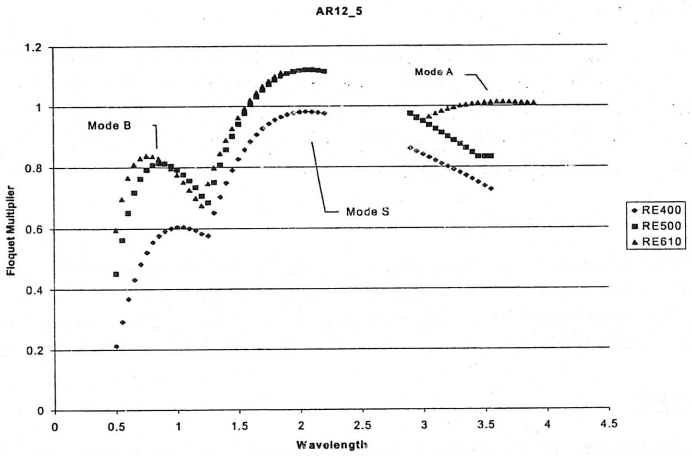


**Figure 3**: Floquet multiplier versus spanwise wavelength for plate $AR = 12.5$

In comparison with Figure 2, the most striking feature of Figure 3, is that an alteration in the aspect ratio of the plate has induced Mode S to become critically unstable (i.e., $|\mu| > 1$) for some regions within the parameter space ($Re$, $\lambda$) of interest. Furthermore, Mode S has become the most unstable wavelength. Therefore, experimentally, if the Reynolds number was increased gradually from a value below $Re_{Cr}$, the first spanwise instability to be noticed would be Mode S, not Mode A.

Finally, an increase in $AR$ from 12.5 to 17.5, produces the plot shown in Figure 4 below. Once again, Mode S is the most unstable three-dimensional instability mode found. That is, it is the first to appear as the Reynolds number is increased.

When compared to the previous plate ($AR = 12.5$), the value of $Re_{Cr}$ appears to be higher, indicating that an increased aspect ratio increases the value of $Re_{Cr}$ for the onset of a three-dimensional wake. For all

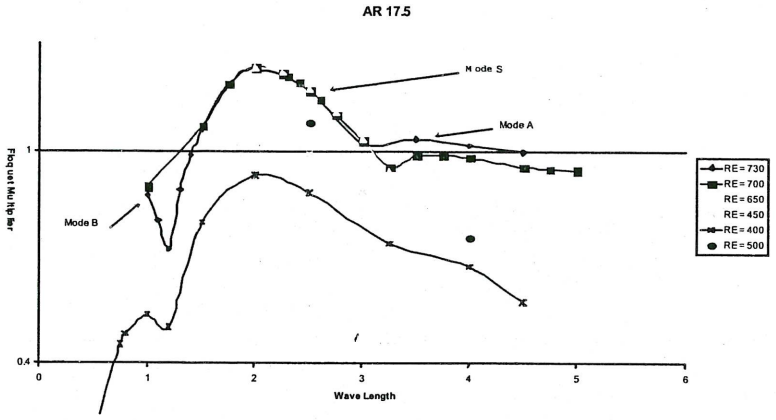


**Figure 4**: Floquet multiplier versus spanwise wavelength for plate $AR = 17.5$

aspect ratios investigated, Mode S appears to saturate towards a critical Floquet multiplier as the Reynolds number is increased. For example, for $AR$ =17.5, a set *envelope* function describes the variation of the Floquet multiplier across the wavelength band $1.5Th < \lambda < 3Th$ for $Re$ in the range [650, 730].

It is conjectured that the (closer to) equilibrium boundary layer profile obtained for longer bodies seems to favour the initial amplification of the Mode S instability over Mode A and B. The exact cause of this difference in preference, given relatively similar boundary layer profiles, is currently under investigation. It may be concluded that while the circular cylinder may be used successfully to provide a two-dimensional wake profile for a generic bluff body, it does not necessarily provide a three-dimensional transition scenario applicable to elongated bluff bodies.

## 4. CONCLUSION

The results from a Floquet analysis of the flow around a nominally two-dimensional blunt flat plate have been presented. The results indicate the presence of a third mode of three-dimensional instability, Mode S. This mode is found to have a spanwise wavelength of 1.8 – 2 plate thicknesses. For sufficiently large aspect ratio, Mode S dominates the wake flow field, becoming the principal unstable mode causing three-dimensional transition in place of Mode A, which dominates for shorter bluff bodies.

## 5. REFERENCES

NOACK, B. and ECKELMANN, H., "A global stability analysis of the steady and periodic cylinder wake", *J. Fluid Mech.*, **270**, 297-330, 1994.

GERRARD, J.H., "The three-dimensional structure of the wake of a circular cylinder", *J. Fluid Mech.*, **25**, 143-164, 1966.

HENDERSON, R.D., "Nonlinear dynamics and pattern formation in turbulent wake transition, *J. Fluid Mech.*, **352**, 65-112, 1997.

NOACK, B., KONIG, M., and ECKELMANN, H., "Three dimensional stability analysis of the periodic flow around a circular cylinder", *Phys. Fluids A.*, **5**, 1279-1281, 1993.

WILLIAMSON, C.H.K., "Vortex dynamics in the cylinder wake", *Annu. Rev. Fluid Mech* , **28**, 477-539, 1996.

ROSHKO, A., "On the wake and drag of bluff bodies", *J. Aeronaut. Sci.*, **22**, 124- , 1955.

BARKLEY, D. and HENDERSON, R.D., "Three-dimensional Floquet stability analysis of the wake of a circular cylinder", *J. Fluid Mech.*, **322**, 215-241, 1996.

WILLIAMSON, C.H.K., "The existence of two stages in the transition to three-dimensionality of a cylinder wake", *Phys. Fluids.*,**31**, 3165- , 1988.

ZHANG, H., FEY, U. and NOACK, B.R., "On the transition of the cylinder wake", *Phys. Fluids.*, **7**, 779-794, 1995.

ROBICHAUX, J., BALACHANDAR, S. and VANKA, S.P., "Three-dimensional Floquet instability of the wake of a square cylinder", *Phys. Fluids.*,**11**, 560-578, 1999.

THOMPSON, M., HOURIGAN, K. and SHERIDAN. J., "Three-dimensional instabilities in the wake of a circular cylinder", *Exp. Therm. Fluid Sci.*, **12**, 190 - , 1996.

IOOS, G. and JOSEPH, D.D., "Elementary Stability and Bifurcation Theory", 2nd Edition, *Springer Verlag, Berlin*, 1990.

*Melbourne Graduate Fluids Conference, 2001*
*Monash University, Melbourne, Australia*

# EFFECT OF FREE STREAM TURBULENCE LEVEL ON EMBEDDED THERMISTOR ANEMOMETERS

**D. M. BURTON, J. SAUNDERS & J. SHERIDAN**

Department of Mechanical Engineering
Monash University, Clayton, Victoria, AUSTRALIA

## ABSTRACT

Experiments were conducted in a wind tunnel to observe the behaviour of an embedded thermistor anemometer in turbulent flow. Symmetric grids were used to increase tunnel turbulence levels, while tunnel temperature was held constant. A hot-wire anemometer was used to determine velocity and turbulence intensity of the flow over the thermistor. Measurements showed a change in tunnel turbulence level significantly affected the output of an embedded thermistor anemometer. The results were inconclusive as to the exact effect of turbulence intensity and scale. The use of thermistor anemometers in turbulent environments should be undertaken with caution, until the effects of turbulence are further quantified.

## 1. INTRODUCTION

Thermistors are commonly used as single point thermal anemometers, behaving as slow response, robust hot-wires. The two major effects on heat transfer, and therefore output, from a thermistor are the fluid flow rate and the temperature differential between the thermistor and the fluid. It is common practice to calibrate thermistors in low turbulence wind tunnels at known velocity and temperature points. Such a calibration for one particular thermistor is shown in Figure 1, as made by the author. When a thermistor is used to find the velocity of a flow of known temperature a voltage measurement is taken, and the flow velocity determined from the calibration plot.

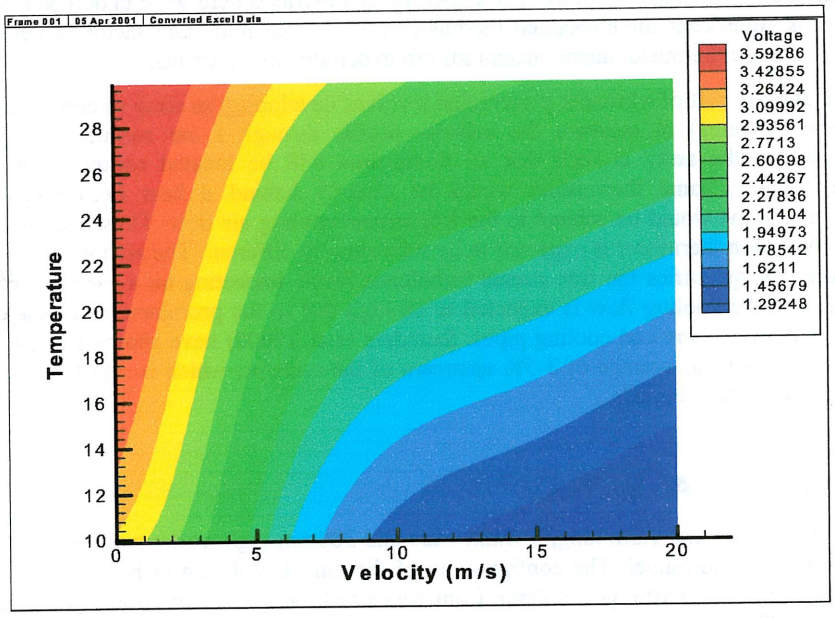


**Figure 1** : Thermistor Calibration.

Inadequate attention has been paid to the effects of free stream turbulence levels on thermistor anemometer accuracy. Unlike a hot-wire which, being extremely small with a fast response can be treated as a body in a time dependent stream, the thermistor with a high thermal mass averages readings over time. Thus, the effect of turbulence on thermistor performance must be considered.

An increase in turbulence intensity, with other flow properties held constant, will generally produce an increase in Nusselt number (Nu). For heat transfer purposes, the simplest and most representative way to model a thermistor is by a sphere in free space. Whilst the thermistor used in this experiment was not in free space, nor perfectly spherical, an evaluation of the Nusselt number of a sphere is relevant because it highlights the flow properties that may affect heat transfer. Achenbach (1978) obtained

relationships for heat transfer from a sphere in cross-flow with Prandtl number equal to 0.71, the results show the Nusselt number for a sphere to be a function of both Reynolds (Re) and Prandtl numbers. Kestin (1966) collated the results of Maizel and Sherwood (shown in Figure 2.) which indicate for a given Reynolds number the variation in Nusselt number was as much as 40 per cent over a range of turbulence intensities. Thus the Nusselt number is a function of turbulence parameters, in addition to the Reynolds and Prandtl numbers.

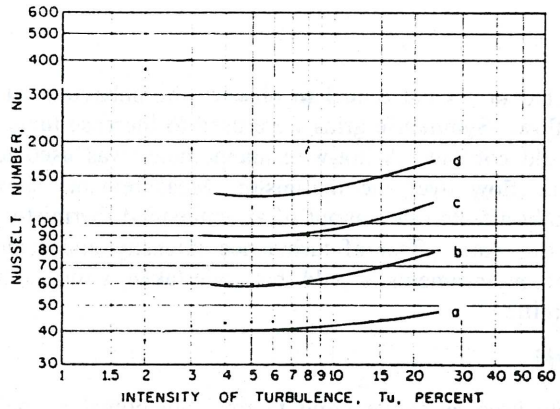


**Figure 2**: Effect of Turbulence Intensity on Nu of Spheres. (a) Re = 2440, (b) Re = 6060, (c) Re = 12450, (d) Re = 19500 (Kestin, 1966)

Given these results it is unreasonable to assume that a calibration in a low turbulence intensity wind tunnel will be applicable to measurements in a highly turbulent airflow. In such a situation it would expected that high turbulence levels would cause the output of the thermistors to indicate a higher velocity than the true average velocity. The experiments described here were undertaken to determine if this effect is significant for embedded thermistors. This is an important factor in determining the applicability of these thermistor anemometers for use in certain environments.

This investigation is part of a broader project that involves developing an array of embedded thermistor anemometers (96 units) to measure the velocity profile through a car radiator. The location of thermistors within the array is such that all thermistors will be located on the front face of the automotive radiator, some thermistors would be directly behind a heat exchanger (automotive condenser), and some would be subject to the free stream cooling air flow. Thus, the turbulence level of the flow over each thermistor is expected to be substantially different. The author has been unable to find literature that quantifies the free stream turbulence levels impacting on a car radiator. However, the turbulence in the cooling flow is expected to be high due to the prominence of flow obstructions such as structural members and cooling pipes. Saunders et al. (2000) have shown that the free stream turbulence intensity is an average of 3-5% upstream of the radiator, which is significantly larger than exists in most calibration tunnels.

## 2. EXPERIMENTAL METHOD

Tests were undertaken in a 1.2m long, 300mm wide and 300mm high working section that was placed in a closed circuit wind tunnel. The configuration of the tunnel is shown in Figure 3. The thermistor was positioned in a thin plastic grid 600mm from the exit of the working section and 600mm from the contraction exit. The thermistor anemometer consisted of two thermistors, embedded on opposite sides of the structure (see Figure 4). The front thermistor is used for speed sensing and the rear thermistor to detect any flow reversal. For the purpose of this experiment only the front thermistor was tested.

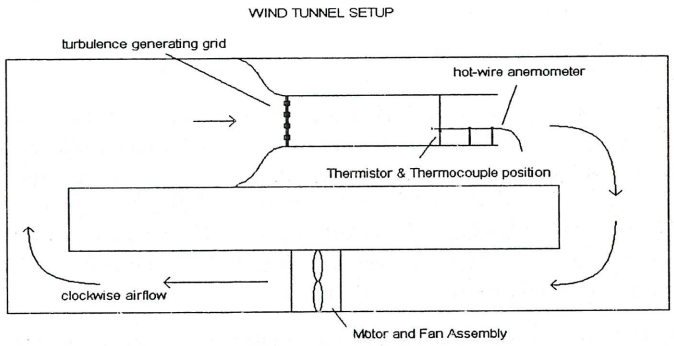


**Figure 3:** Wind tunnel set-up.

The thermistor was integrated into a Wheatstone bridge circuit that was supplied with a constant voltage. A calibrated thermocouple was located 20mm from the thermistor to measure flow temperature. Velocity and turbulence intensity was measured using a hot-wire anemometer. The hot-wire anemometer was calibrated isothermally against a pitot-static tube at 25°C. The bridge or thermistor output voltage, velocity and temperature were monitored by a data acquisition system.

The probe could not be located behind the thermistor, as it would be in the wake of the thermistor grid, and thus be subject to unrepresentative turbulence levels. Similarly, placement of the probe in front of the thermistor would cause a wake over the thermistor. To avoid this the probe was placed 10mm upstream and 20mm above the thermistor, and an assumption was made that the turbulence levels measured at this point were representative of those at the thermistor.

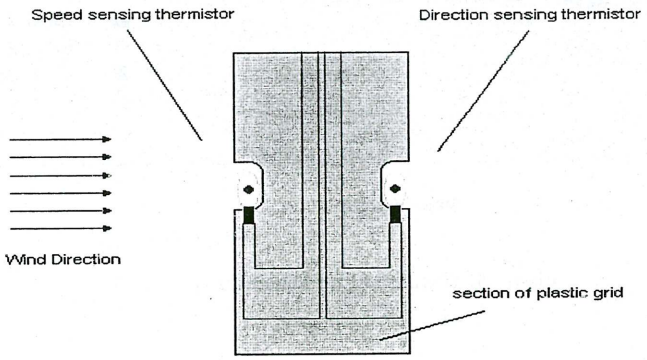


**Figure 4**: Thermistors embedded in plastic grid.

To generate varying levels of turbulence three different grids were alternately placed in the wind tunnel at the contraction exit. Table 1 shows the grid dimensions. Turbulence length scale measurements were not made, however the relative length scale is proportional to grid slat size. Thus, it is assumed that grid #1 has the greatest length scale and grid #3 the smallest. Data was obtained for each grid over a range of velocities by varying the tunnel fan speed, with all readings taken at constant temperature of 25°C.

| | Slat Width (mm) | # Slats | Blockage Percentage | Turbulence Intensity |
|---|---|---|---|---|
| **Grid 1** | **70** | **2** | **63.5%** | **29.9%** |
| **Grid 2** | **35** | **6** | **76.1%** | **28.4%** |
| **Grid 3** | **20** | **8** | **67.4%** | **21.9%** |
| **No Grid** | **-** | **-** | **-** | **1.0%** |

**Table 1. Grid Dimensions and Turbulence Intensities**

## 3. RESULTS AND DISCUSSION

It was found that the output of the thermistors drifted slightly so it was necessary to take a reading at zero velocity before and after each grid was tested. This enabled a corrected voltage to be calculated. An increase in this corrected voltage output indicates an increase in heat transfer from the thermistor. The average turbulence intensity level for each grid is shown in Table 1. A plot of voltage versus velocity is shown in Figure 5. This highlights the effects of the different flow regimes on thermistor heat transfer. It can be seen that for all grids an increase in turbulence level caused a corresponding increase in thermistor heat transfer, relative to the no grid case.

It was expected that the tests would establish an obvious relation whereby an increase in turbulence intensity could be linked to an increase in heat transfer. Similarly, a relation between turbulence length scale and thermistor heat transfer was sought. However, no relationship could be established that quantifiably linked specific changes in turbulence characteristics to increases in thermistor output. It could only be stated that the embedded thermistor anemometer, when placed in flow of a turbulent nature, exhibited significantly different and increased heat transfer rates to those displayed when in laminar flow. Further research will be undertaken to better quantify the effect of scale and intensity on thermistor heat transfer. The experiment will be repeated using lower blockage grids, and a greater distance between the turbulence generating grids and the thermistor to ensure the flow is homogeneous.

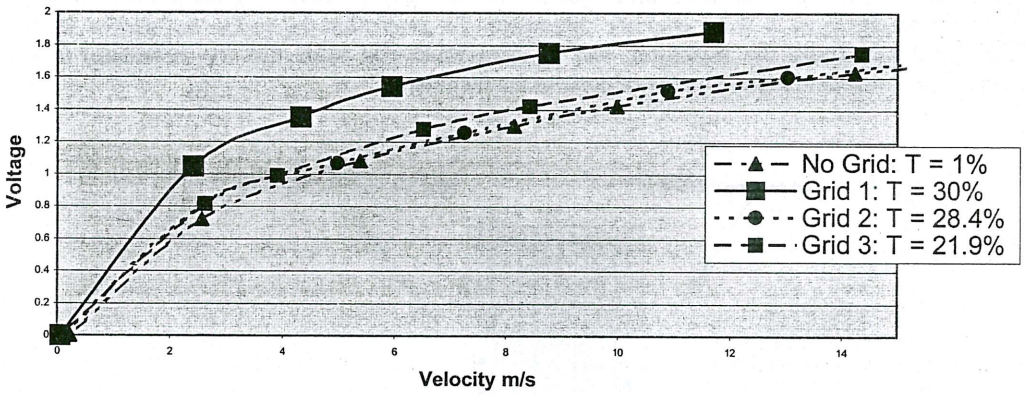


**Figure 5:** Thermistor Calibration Curve

## 4. CONCLUSION

This investigation was undertaken to determine whether the effect of turbulence on the performance of an embedded thermistor anemometer was significant. The results showed that a large increase in turbulence intensity and scale did significantly affect the thermistor heat transfer and therefore the voltage output. The relative effect of scale and intensity has not been found conclusively and warrants further investigation. Before using thermistor anemometers for velocity measurement in turbulent environments, the turbulence levels expected should be known and the effects quantified.

## 5. ACKNOWLEDGEMENTS

The authors would like to acknowledge Monash University, the Australian Government and Ford Australia for providing the support, facilities and funds needed to complete this research.

## 6. REFERENCES

ACHENBACH, E., "Heat transfer from spheres up to Re = $6\times10^6$, *Proc. Sixth Int. Heat Trans Conf.*, vol.5, Hemisphere Pub. CO., Washington D.C., pp341-346, 1978

KESTIN, J., "The Effect of Free-Stream Turbulence on Heat Transfer Rates", *Advances in Heat Transfer*, **3**, 1-32,1966

SAUNDERS, J., et al., "On-Road and Wind Tunnel Turbulence and its Measurement Using a Four-Hole Dynamic Probe ahead of several Cars", SP-1524

*Melbourne Graduate Fluids Conference, 2001*
*Monash University, Melbourne, Australia*

# COMPARISON BETWEEN EXPERIMENTAL AND NUMERICAL METHODS FOR EVALUATING CAR COOLING SYSTEM DESIGN

**K. JOHANNESSEN[1], J. SAUNDERS[1], J. SHERIDAN[1] and D. NICLASEN[2]**

[1]Department of Mechanical Engineering
Monash University, Clayton, Victoria, AUSTRALIA
[2]Holden Ltd., Port Melbourne, Victoria, AUSTRALIA

## ABSTRACT

Numerical studies of cooling airflow using computational fluid dynamics (CFD) software allow engineers to analyse designs earlier in the design cycle and at a reduced cost compared to wind tunnel experiments. However, testing is required to confirm if the CFD codes are correctly modelling the flow near the radiator.

The cooling performance of a car has been studied numerically using the Computational Fluid Dynamics (CFD) code Fluent and experimentally by measuring the Specific Dissipation of a radiator. Modifications were made to the fascia of the car and the cooling performance determined using both the numerical and experimental methods. It was found that the CFD code was accurate in predicting the trends when the fascia was changed. The seven variations tested were ranked correctly with the exception of one pair of results. Flow visualisation conducted in the wind tunnel confirmed the presence of flow structures predicted by CFD models

## 1. INTRODUCTION

Over the last thirty years there have been increasing demands on the engine cooling system of a car. This has been caused by a steady increase in engine output, combined with a reduction in the size of the cooling inlets and an increase in auxiliary components (Emmelmann and Berneburg, 1990). A water-cooling system is almost universal in new cars using a mixture of water and ethylene glycol as the coolant fluid. This fluid passes through the engine extracting heat before being pumped to a compact heat exchanger (radiator). The radiator transfers heat from the coolant fluid to passing airflow by convection. The cooling air velocity comes from either the forward motion of the car (ram air) or from an fan enclosed in a shroud (fan air) attached to the radiator. In addition, a condenser required by the air conditioning system is often located in the same airflow as the radiator (Newton et.al, 1996).

The fascia covers the front of the car and generally contains radiator air inlets, front bumper and the number plate (see Figure 1). While the fascia of a car has a significant influence on the amount of air reaching the radiator, it is crucial to the appearance of the car and is often finalised early in the design cycle with physical prototypes being expensive. However, computational surface data is usually available on and a computer model can be created at a minimal cost. But, if computer modelling of the effect of fascia changes on cooling performance is going to be of any value, testing is required to determine the accuracy of CFD results relative to current experimental test results. This is made difficult because flow under the hood is complex with regions of flow separations caused by complicated geometry.

The most thorough experimental study of CFD accuracy was conducted by Williams and Vemaganti of the Ford Motor Company (1998). They measured the airflow rate through the radiator using nine vane anemometers for twenty-three geometry configurations on the front-end of the car. The same scenarios were modelled using a Reynolds-Averaged Navier Stokes solver with a standard k-ε turbulence model. The authors found that 14/23 cases were misranked by the CFD analysis however only five were misranked by three or more places. The numerical prediction of airflow rate was an average of 1.8% below experimental values with a 90% confidence of 11.8 % on the individual measurements. The CFD output indicated regions of reverse flow that would have been quite difficult to identify in wind tunnel experiments. The anemometers used in this study were 114mm in diameter and errors could have arisen from averaging across non-uniform flow.

## 2. EXPERIMENTAL METHOD

The mass flow rate of air through the radiator is difficult to measure accurately. Vane anemometers can be used but these can experience averaging errors and the removal of the fan and shroud is often required. Hotwires are too fragile and other techniques require visual access to the flow. As a result, the cooling performance presented here was found by measuring the Specific Dissipation (SD) of the installed radiator. The Specific Dissipation is a measure of the heat rejection of a radiator and is defined as the heat transfer rate divided by the maximum temperature difference across the heat exchanger given in equation (1):

$$SD = \frac{Q}{T_{coolant,in} - T_{air,in}} = \frac{\dot{m}_{coolant} \times C_{p,coolant} \times (T_{coolant,in} - T_{coolant,out})}{T_{coolant,in} - T_{air,in}} \quad [\mathrm{W/K}] \quad (1)$$

The subscript coolant stands for the radiator coolant fluid, which is the hot fluid while the air acts as the cold fluid. This value is related to the heat exchanger effectiveness but does not require the measurement of the temperature of air exiting the radiator. This technique has been used previously on a simplified front end (Hird, Johnson & Pitt, 1986) and on complete cars (Lin et al.,1997)

Experimental measurements were conducted in the full-scale wind tunnel located at Monash University. A 30 kW heat bench supplied hot water to the radiator from outside the wind tunnel. The temperature of the coolant at the inlet and outlet were measured by T-type thermocouples, as was the ambient air temperature. The coolant flow rate is measured by a magnetic flowmeter. In this program eight fascias were tested having different sized frontal openings with the rest of the car unchanged.

## 3. NUMERICAL METHOD

The air flow around the car was modelled using the commercial CFD code Fluent (Version 5). In Fluent, a three-dimensional segregated solver was used to solve the steady Reynolds Averaged Navier-Stokes equations. The turbulence model used was a realizable k-$\varepsilon$ type with standard wall functions. The solver used a first order upwind scheme and the pressure-velocity coupling was conducted using the SIMPLE algorithm

The model grid consisted of an unstructured triangular surface mesh created on all external surfaces back to the B-pillar and larger engine bay components (Figure 1). Using the Tgrid software package a tetrahedral volume mesh was created containing ~850,000 elements. Cells were distributed unevenly with the smallest cells located in regions of the largest velocity and pressure gradients.

The boundary conditions were based on test conditions measured in the wind tunnel (Saunders and Mansour, 2000). The inlet was set to a velocity of 16.67 m/s with turbulence levels of 3 % and a length scale of 0.2 m. The outlet was a pressure outlet type with the same turbulence constraints. The sides of the domain were symmetry walls whilst the floor was a no-slip wall, like the wind tunnel floor. The radiator and condenser were modelled as a porous media with flow resistance obtained from manufacturer's performance curves. Each case was solved until the residuals converged to less than $1 \times 10^{-4}$. In addition, the mass flow rate through the radiator was monitored to ensure convergence had been achieved.

## 4. RADIATOR AIRFLOW COMPARISON

### 4.1. RESULTS

While the CFD model solution provided the air mass flow rate through the radiator in kg/s, the Specific Dissipation test gave the heat rejection in W/K. Thus, the values could not be compared directly and as a consequence the percentage change from the initial baseline case is examined. This approach is acceptable in industry as the performance of a new car is normally based on an evolution from a previous model. The results obtained with the eight fascia configurations tested are shown in Table 1 with the airflow values, relative improvements from baseline and the ranking of the cases from 1 (worst) to 8 (best).

### 4.2 DISCUSSION

The results obtained suggested that the CFD model can predict performance trends showing whether a change would make the airflow greater or less. An error in this can lead engineers to pursue inferior designs. The fascias tested were correctly ranked in order except for one pair of data where the ranking swapped. The CFD model swaps the ranking of fascias C and D with respect to the experimental

results. Further testing is required to identify the reason for this. Resolutionn down to 1% is required for commercial applications and further tests will be done to approach this range.

| Condition | Numerical Results | | | Experimental Results | | |
|---|---|---|---|---|---|---|
| | Air Mass Flow Rate kg/s | Change from Baseline and Ranking | | Specific Dissipation kW / K | Change from Baseline and Ranking | |
| Baseline Fascia (BL) | 0.67 | | | 1.57 | | |
| Fascia A | 0.51 | -23.8 % | 1 | 1.39 | -14.6 % | 1 |
| Fascia B | 0.73 | 8.4 % | 5 | 1.69 | 7.6 % | 4 |
| Fascia C | 0.72 | 7.5 % | 4 | 1.70 | 8.6 % | 5 |
| Fascia D | 0.61 | -8.7 % | 2 | 1.45 | -8.5 % | 2 |
| Fascia E | 0.76 | 13.2 % | 6 | 1.75 | 10.7% | 6 |
| Fascia F | 0.84 | 25.2 % | 7 | 1.45 | 17.4 % | 7 |
| Fascia G | 0.66 | -2.3 % | 3 | 1.85 | -8.0 % | 3 |

**Table 1** : Experimental and Numerical results

When looking at the magnitude of the change in performance from baseline the results in Table 1 show that the agreement was quite poor between the numerical and experimental results, especially for the cases with large changes in performance (eg Fascia A had reduction in performance –23.8% vs. –14.6%). This indicates that numerical methods were more sensitive than the experimental tests. It is not known which of these techniques is giving the correct results. Fascia G went against this trend with the experimental tests showing a significantly higher increase in performance. The reason for this was that this particular fascia had the grille moulded into it (unlike any others tested), which was not modelled numerically. The blockage of the real grille was significant enough to reduce the cooling performance by around 6%, which is reasonable according to previous tests. This test highlights the problem with CFD resolving small details like the grille elements.

## 5. FLOW VISUALISATION RESULTS

Yarn tuft flow visualisation was used to determine flow features between the fascia and the radiator. The features were :

- Air entering the upper nostril with some air passing over the radiator and the rest making a curtain of air about 3 cm thick seen flowing towards the top of the condenser.
- Air travelling forwards against the wind direction between the fascia and the front bumper bar.
- The effect of the air dam was to cause air to enter vertically through the bottom (breathing) opening. Air then flowed up the front face of the condenser.
- Flow circulating behind the numberplate and around the bumper bar.

All these features are present in the CFD output of velocity vectors as shown in Figure 2.

## 6. CONCLUSIONS

The Fluent CFD code has been used to model the cooling performance of a car with various fascia configurations. The results were compared with those obtained using a standard experimental test measuring the Specific Dissipation in the Monash University Full Scale Wind Tunnel. The tests showed the ability of CFD to predict performance trends and the ranking of the facias was correct for all but two configurations. The experimental and numerical techniques displayed a poor agreement on the magnitude of the change from baseline with numerical results were more sensitive than the experimental results. The CFD results showed clearly that the flow field between the fascia and the radiator is complex, separated flow. In the wind tunnel yarn tufts showed the presence of flow structures observed in the CFD output. This experiment has indicated the ability of using CFD as a valuable tool early in the design process with experimental validation completed before project sign-off.

## 7. ACKNOWLEDGEMENTS

The authors would like to acknowledge the generous support of Holden Ltd. with this program. The support of the Monash University Mechanical Engineering Department is also greatly appreciated.

## 8. REFERENCES

EMMELMANN, H.J. and BERNEBUR, H., "Aerodynamic Drag and Engine Cooling - Conflicting Goals?". *SAE Technical Paper 905128*, 1990.

LIN, C., SAUNDERS, J. W., WATKINS, S. and MOLE, L. "Increased Productivity - The Use of Specific Dissipation to Evaluate Engine Cooling". *SAE Technical Paper 970137*, 1997.

LIN, C., "Specific Dissipation as a technique for evaluating motor car radiator cooling performance", *Ph.D Thesis*, RMIT, 1999.

NEWTON, K., STEEDS, W. and GARRETT, T. K., "The Motor Vehicle", 12th Ed, Butterworth Heinemann, Oxfod, UK, 1996.

SAUNDERS, J.W. and MANSOUR, R.B., "On-road and Wind Tunnel Turbulence and its Measurement Using a Four-Hole Dynamic Probe Ahead of Several Cars", *SAE Technical Paper 2000-01-0350*, 2000.

WILLIAMS, J. VEMAGANTI, G., "CFD Quality - A Calibration Study for Front-End Cooling Airflow", *SAE Technical Paper 980039*, 1998.

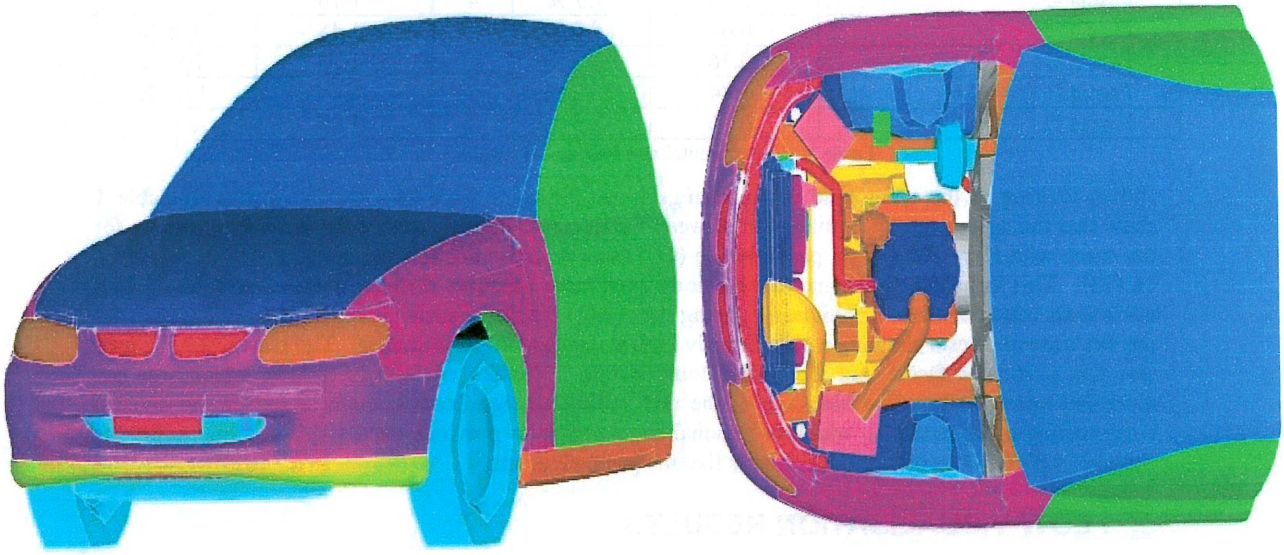

**Figure 1** : Surface model of car body with engine components exposed

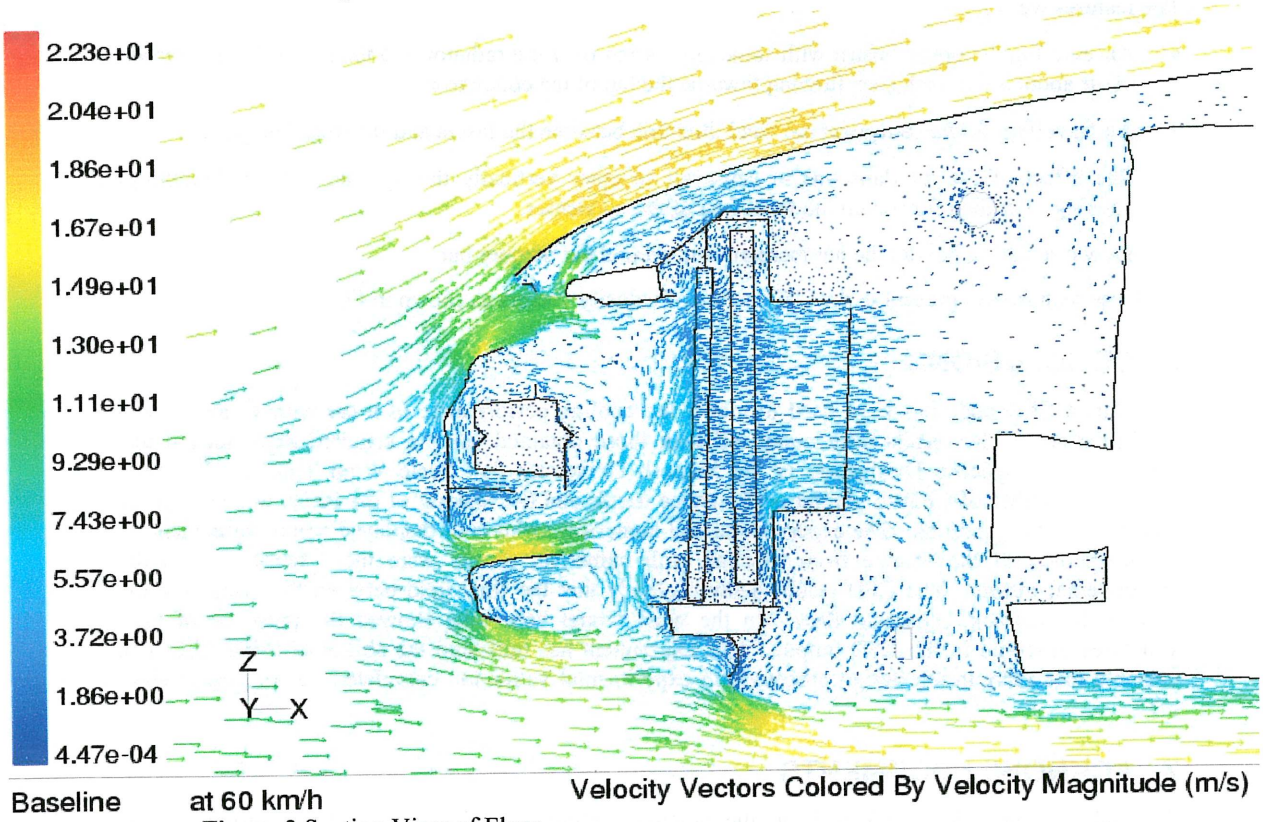


**Figure 2** Section View of Flow

*Melbourne Graduate Fluids Conference*
*Monash University, Melbourne, Australia*
*July 2001*

# STREAMWISE EVOLUTION OF TURBULENT BOUNDARY LAYERS

**Anne K. HELLSTEDT, Malcolm B. JONES and Min S. CHONG**

Department of Mechanical and Manufacturing Engineering
University of Melbourne, Victoria 3010, AUSTRALIA

## ABSTRACT

An outline of a closure scheme for computing the streamwise evolution of a turbulent boundary layer in an arbitrary pressure gradient is presented. It is applied to the specific case of sink flow.

## 1. INTRODUCTION

Utilising the Coles (1956) logarithmic law of the wall and law of the wake formulation, in conjunction with the mean continuity and mean momentum equations, Perry *et al.* (1994) derived an analytical expression of shear stress distribution to aid in the computation of the evolution of turbulent boundary layers. From the shear stress distribution, the state of a boundary layer is described by four non-dimensional parameters. The relationship between these parameters, which is assumed to be universal, is obtained experimentally. As existing data is sparse, an interpolation and extrapolation scheme is devised to compute the development of flows not already observed. The result is a pair of coupled first order ODEs which allow the streamwise evolution of the layer to be computed when the initial velocity profile and the streamwise distribution of freestream velocity are known.

## 2. EXPRESSION FOR SHEAR STRESS DISTRIBUTIONS

The mean velocity profile of a wall bounded turbulent boundary layer can be described by the Coles (1956) law of the wall, law of the wake formulation given by

$$\frac{U}{U_\tau} = \frac{1}{\kappa}\ln\left[\frac{zU_\tau}{\nu}\right] + A + \frac{\Pi}{\kappa}W_c\left[\eta,\Pi\right] \tag{1}$$

where it is generally assumed that $\kappa$ is equal to 0.41 and $A$ is equal to 5.0. $U$ is the mean streamwise velocity, $U_\tau$ is the friction velocity, $z$ is the distance normal to the wall, $\nu$ is the fluid kinematic viscosity, $\Pi$ is the Coles wake factor which generally varies with streamwise distance, $W_c$ is the Coles wake function and $\eta = z/\delta_c$, where $\delta_c$ is the boundary layer thickness.

For analytical work, the wake function is expressed in terms of a polynomial function. To ensure that the gradient $\partial U/\partial z = 0$ at $\eta = 1$, a corner function is required. Jones (1998) introduced a new corner function into the wall of the wall, law of the wake formulation, namely $-\eta^3/3\kappa$, which achieves the required peel off from the law of the wall. Therefore, the the law of the wall, law of the wake becomes

$$\frac{U}{U_\tau} = \frac{1}{\kappa}\ln\left[\frac{zU_\tau}{\nu}\right] + A - \frac{1}{3\kappa}\eta^3 + \frac{\Pi}{\kappa}2\eta^2(3-2\eta) \tag{2}$$

This formulation of Jones (1998) is utilised in the derivation of the expression for shear stress profiles, along with the continuity equation and mean momentum equations, to give

$$\frac{\tau}{\tau_0} = f_1\left[\eta,\Pi,S\right] + g_1\left[\eta,\Pi,S\right]\zeta + g_2\left[\eta,\Pi,S\right]\beta \tag{3}$$

The three functions, $f_1, g_1$ and $g_2$, are known universal analytical functions. $\zeta$ is the wake strength gradient parameter given by $\zeta = S\delta_c d\Pi/dx$ and $\beta$ is the Clauser pressure gradient parameter, $\beta = (\delta^*/\tau_0)(dp/dx)$, where $S = U_1/U_\tau$ is the skin friction parameter, $U_1$ is the freestream streamwise velocity, $x$ is the streamwise coordinate, $\delta^*$ is the displacement thickness of the boundary layer, $\tau_0$ is the wall shear stress and $p$ is the average

pressure. From equation (3) the appropriate non-dimensional parameters for calculating the streamwise evolution of the turbulent boundary layer are obtained, that is, $\Pi$, $S$, $\beta$ and $\zeta$.

# 3. CLOSURE SCHEME FOR TURBULENT BOUNDARY LAYERS

Initially Perry *et al.* (1994) considered the closure equation for approximate equilibrium flows. An approximate equilibrium flow is defined as one where $\Pi$ is invariant with $x$ (ie. $\zeta = 0$) and hence the velocity defect profiles are self-similar. For this class of flows, it is assumed the shear stress profiles are approximately self-similar and thus characterised only by $\Pi$, ie.

$$\frac{\tau}{\tau_0} = f[\eta, \Pi] \tag{4}$$

It is found that $f_1$, $g_1$ and $g_2$ become independent of $S$ for $S$ sufficiently large. Hence, taking the limiting case of $S \to \infty$ in (3) and noting $\zeta = 0$ we have

$$\frac{\tau}{\tau_0} = f_1[\eta, \Pi, \infty] + g_2[\eta, \Pi, \infty]\beta_a \tag{5}$$

where $\beta_a$ denotes the asymptotic value of $\beta$ for the restricted case of approximate equilibrium flow.

From (4) and (5) it is obvious that

$$\beta_a = \beta_a[\Pi]. \tag{6}$$

With the aid of (6), it is now possible to determine the required functional form of $\beta$ that forces approximate self-similarity of (3) when $\zeta = 0$ and (5). This results in a relationship for closure of the form

$$C[\Pi, \beta, S] = 0 \tag{7}$$

Perry *et al.* (1994) assumed (7) would also be valid when $\Pi$ varies only slowly with streamwise distance.

## 3.1 GENERAL NON-EQUILIBRIUM CASE

For the general non-equilibrium flow case in an arbitrary pressure gradient $\zeta$ must be included. Therefore, for closure, Perry *et al.* (1998) considered the relation

$$\mathcal{F}[\Pi, S, \beta, \zeta] = 0, \tag{8}$$

assuming that $\mathcal{F}$ is universal and only the four parameters are required in its formulation.

Perry *et al.* (1994) considered the shear stress to be fixed by a one-parameter family for approximate equilibrium flows, ie. (4), however, it is more correct to describe the shear stress profiles by a two-parameter family of the form

$$\frac{\tau}{\tau_0} = f[\eta, \Pi, \beta_a] \tag{9}$$

To obtain a formulation for $\mathcal{F}$ an interpolation and extrapolation scheme is developed. Begin by considering the $S - \beta$ plane for a fixed $\Pi$ which contains an experimental data point for which $S$, $\beta$, $\zeta$ and $\Pi$ are all known and from (3) $\tau/\tau_0$ versus $\eta$ is also known. By performing a curve-fit, the contour of a fixed shear stress profile shape can be traced out. As $S \to \infty$, $\beta$ and $\zeta$ approach asymptotic values $\beta_a$ and $\zeta_a$, respectively, as shown in Figure 1. The process of keeping the profile shape fixed is referred to as profile matching.

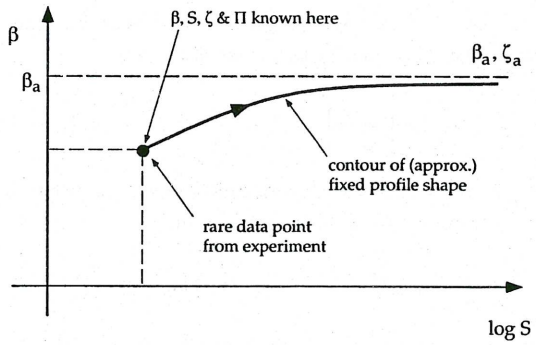


Figure 1: Fixed shear stress profile for a fixed $\Pi$.

The profile matching is achieved by using the following least squares error criterion

$$\frac{\partial}{\partial\beta_a}\left\{\int_0^1\left[\left(\frac{\tau}{\tau_0}\right)_{S\to\infty}-\left(\frac{\tau}{\tau_0}\right)\right]^2 d\eta\right\}=0,\qquad \frac{\partial}{\partial\zeta_a}\left\{\int_0^1\left[\left(\frac{\tau}{\tau_0}\right)_{S\to\infty}-\left(\frac{\tau}{\tau_0}\right)\right]^2 d\eta\right\}=0 \tag{10}$$

By repeating the profile matching procedure for different values of $\Pi$, it is then possible to map out lines of constant $\zeta_a$ in the $\Pi-\beta_a$ plane and thus obtain a known function

$$\psi[\Pi,\beta_a,\zeta_a]=0. \tag{11}$$

This shear stress profile matching procedure produces isosurfaces of $\zeta$ which can be mapped out in $\Pi-\beta-S$ space. Hence $\mathcal{F}[\Pi,S,\beta,\zeta]=0$ is known.

### 3.2 EVOLUTION EQUATIONS

Evolution equations, forming a set of first order ordinary differential equations for $S$ and $\Pi$, are obtained using the logarithmic law of the wall, law of the wake and the momentum integral equation.

The first evolution equation, derived from the law of the wall and law of the wake together with the momentum integral equation, is given by

$$\frac{dS}{dR_x}=\frac{\chi[R_x,R_L]\,R[S,\Pi,\zeta,\beta]}{SE[\Pi]\exp[\kappa S]} \tag{12}$$

where

$$R[S,\Pi,\beta,\zeta]=\frac{S+\beta(2S-C_2[\Pi]/C_1[\Pi])+\zeta(2C_1[\Pi]S-2C_2[\Pi]-S\frac{dC_1}{d\Pi}+\frac{dC_2}{d\Pi})}{\kappa C_1[\Pi]S^2-\kappa C_2[\Pi]S+C_2[\Pi]}$$

$$C_1[\Pi]=\int_0^1\frac{U_1-U}{U_\tau}d\eta,\qquad C_2[\Pi]=\int_0^1\left(\frac{U_1-U}{U_\tau}\right)^2 d\eta$$

$$E[\Pi]=\exp\left[-\kappa\left(A+\frac{2\Pi}{\kappa}-\frac{1}{3\kappa}\right)\right]$$

where $R_x=xU_0/\nu$, $U_0$ is the freestream velocity at some initial point $R_x=0$ or $x=0$, $R_L=LU_0/\nu$ is the overall Reynolds number of the apparatus and $\chi=U_1/U_0$.

An evolution equation for $\Pi$ is found from the definition of $\zeta$ in conjunction with the law of the wall and law of the wake, without reference to momentum balances, and is given by

$$\frac{d\Pi}{dR_x}=\frac{\zeta\chi[R_x,R_L]}{S^2E[\Pi]\exp[\kappa S]} \tag{13}$$

The definition of $\beta$, along with (2), leads to an auxiliary equation

$$S^2E[\Pi]\exp[\kappa S]\frac{1}{\chi^2}\frac{d\chi}{dR_x}=-\frac{\beta}{C_1[\Pi]} \tag{14}$$

Equations (12) and (13) form a set of coupled first order ODEs for $S$ and $\Pi$, and equation (14) is an auxiliary equation for $\beta$ where $\chi$ is a known given function of $R_x$ and $R_L$. Given equations (12), (13), (14) and the second auxiliary equation of $\mathcal{F}$, it is possible to compute the evolution of a boundary layer.

## 4. SINK FLOW

The study of sink flow turbulent boundary layers is of particular interest as according to Townsend (1956) and Rotta (1962) they represent the only flow case which will reach precise equilibrium on a smooth wall. The freestream velocity distribution of a sink flow turbulent boundary layer corresponds to that of a potential sink. Figure 2 shows the sink flow with a sink of strength $Q$ located at a distance $L$ from the origin, where $x=0$ and $U_1=U_0$.

For sink flow, the acceleration parameter $K=(\nu/U_1^2)(dU_1/dx)$ is a constant. When $K$ is known, the auxiliary equation for $\beta$ simplifies to an algebraic equation of the form

$$-\beta=KC_1S^2E[\Pi]\exp[\kappa S] \tag{15}$$

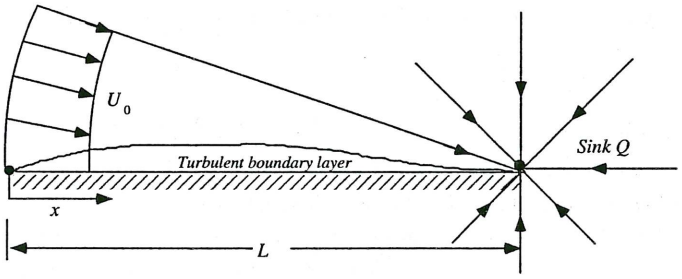


Figure 2: Sink flow.

The following functional form of $\psi[\Pi, \beta_a, \zeta_a] = 0$ has been proposed by Marusic *et al.* (1998) and Perry *et al.* (2001) based upon the experimental data of Jones (1998) for equilibrium sink flow

$$\zeta_a = (0.85 - 6.9\Pi + 8\Pi^2)\Delta\beta_a \tag{16}$$

where

$$\Delta\beta_a = \beta_a - \beta_{ae}$$

and

$$\beta_{ae} = -0.5 + 1.38\Pi + 0.13\Pi^2$$

where $\beta_{ae}$ is the value of $\beta_a$ for $\zeta_a = 0$.

It must be noted that for sink flow the evolution equations become autonomous and can therefore be displayed on a $S - \Pi$ phase plane where solution trajectories cross only at critical points. The coupled evolution equations (12) and (13) become autonomous by an appropriate change in the variable $R_x$ (ie. $T_x = -\ln(1 - R_x K)/K$), therefore $R_x$ does not appear explicitly. The autonomous evolution equations are therefore

$$\frac{dS}{dT_x} = \psi_1[\Pi, S, K], \qquad \frac{d\Pi}{dT_x} = \psi_2[\Pi, S, K] \tag{17}$$

Marusic *et al.* (1998) showed that good agreement exists between Jones' (1998) experimental results and the predicted evolution of the mean flow parameters using (16). Thus, the present closure scheme is functioning correctly and in the Jones (1998) restricted $\Pi - \zeta_a - \beta_a$ functional space equation (16) is a valid estimate. However, a more robust and generally more applicable functional form of $\zeta_a$ is needed to solve for flows with an arbitrary pressure gradient. To achieve this, more experimental data is required.

## 4. CONCLUSION

The present work describes a framework for formulating closure for a turbulent boundary layer evolving in an arbitrary pressure gradient. The mathematical machinery is working, but further experimental data is needed to further assess the viability of the scheme.

## 5. REFERENCES

COLES, D.E. (1956), The law of the wake in the turbulent boundary layer. *J. Fluid Mech.* **1**, 191-226.

JONES, M.B.(1998), Evolution and structure of sink-flow turbulent boundary layers. PhD thesis University of Melbourne, Australia.

MARUSIC, I., PERRY, A.E., JONES, M.B. & CHONG, M.S. (1998), Evolution calculations for turbulent boundary layers approaching equilibrium sink flow. In *Proc. 13th Australasian Fluid Mech. Conf.* Melbourne, Australia.

PERRY, A.E., MARUSIC, I. & JONES, M.B. (1998), New evolution equations for turbulent boundary layers in arbitrary pressure gradients. *Sadhana, Indian Academy of Sci.* **23**, 443-457.

PERRY, A.E., MARUSIC, I. & JONES, M.B. (2001), On the streamwise evolution of turbulent boundary layers in arbitrary pressure gradients. *J. Fluid Mech.*. Under review.

PERRY, A.E., MARUSIC, I. & LI, J.D. (1994), Wall turbulence closure based on classical similarity laws and the attached eddy hypothesis. *Phys. Fluids* **6 (2)**, 1024-1035.

ROTTA, J.C. (1962), Turbulent boundary layers in incompressible flow. *Prog. Aero. Sci.* **2**, 1-219.

TOWNSEND, A.A. (1956), The properties of equilibrium boundary layers. *J. Fluid Mech.* **1**, 561-573.

# NOTES

# NOTES

# NOTES

# NOTES